Contact and Non-Contact Measurement of Electronic Transport in Individual 2D SnS Colloidal Semiconductor Nanocrystals

Adam J. Biacchi[*,‡], Son T. Le[‡], Brian G. Alberding[§], Joseph A. Hagmann[‡], Sujitra J. Pookpanratana[‡], Edwin J. Heilweil[‡], Curt A. Richter[‡], and Angela R. Hight Walker[*,‡]

‡ Nanoelectronics Group, Engineering Physics Division, National Institute of Standards and Technology (NIST), Gaithersburg, Maryland 20899, United States.

§ Remote Sensing Group, Sensor Science Division, National Institute of Standards and Technology (NIST), Gaithersburg, Maryland, 20899, United States.

*E-mail: adam.biacchi@nist.gov, angela.hightwalker@nist.gov

ABSTRACT Colloidal-based solution syntheses offer a scalable and cost-efficient means of producing 2D nanomaterials in high yield. While much progress has been made towards the controlled and tailorable synthesis of semiconductor nanocrystals in solution, it remains a substantial challenge to fully characterize the products' inherent electronic transport properties. This is often due to their irregular morphology or small dimensions, which demand the formation of colloidal assemblies or films as a prerequisite to performing electrical measurements. Here, we report the synthesis of nearly monodisperse 2D colloidal nanocrystals of semiconductor SnS and a thorough investigation of the intrinsic electronic transport properties of single crystals. We

utilize a combination of multi-point contact probe measurements and ultrafast terahertz spectroscopy to determine the carrier concentration, carrier mobility, conductivity/resistivity, and majority carrier type of individual colloidal semiconductor nanocrystals. Employing this metrological approach, we compare the electronic properties extracted for distinct morphologies of 2D SnS and relate them to literature values. Our results indicate that the electronic transport of colloidal semiconductors may be tuned through prudent selection of the synthetic conditions. We find that these properties compare favorably to SnS grown using vapor deposition techniques, illustrating that colloidal solution synthesis is a promising route to scalable production of nanoscale 2D materials.

KEYWORDS: colloidal nanocrystals, 2D materials, solution synthesis, electronic properties, electrical measurements, time-resolved terahertz spectroscopy, tin sulfide

Two-dimensional nanomaterials have garnered immense research interest in the last decade due to their potential as building blocks for the next generation of optoelectronics. Unlike graphene, many metal chalcogenides have a band gap which, as a semiconductor, allows them to serve as the principle constituent of solid-state devices.[1] Metal chalcogenides with a layered crystal structure tend to naturally form 2D crystals, a consequence of stronger in-plane atomic bonding relative to their weaker out-of-plane van der Waals interactions between layers. When nanoscale-thin, this 2D morphology lends itself well for their incorporation into optoelectronics, both due to their ability to stack efficiently with other device components and their substantial mechanical elasticity, which engenders the fabrication of flexible or wearable electronics.[2,3] Additionally, 2D semiconductor nanocrystals display attractive electrical properties, such as higher intrinsic

mobilities than are found in organic electronics or assemblies of 0D nanoparticles, as well as a multitude of emerging, novel physics.[4,5] Two-dimensional materials initially were prepared using micromechanical exfoliation;[6] however, more recently substantial progress has been made in developing *in vacuo* techniques such as chemical vapor deposition (CVD) and molecular beam epitaxy (MBE) that utilize gas-phase reactants.[7] Although large, high-quality single crystals are accessible, scalability and reproducibility remain ongoing issues for these techniques, which currently limit their efficacy for commercial applications.[8,9]

A promising alternative to gas-phase deposition of 2D materials is solution-based synthetic strategies. These low-temperature methods yield liquid "inks" of dispersed freestanding 2D semiconductors that allow for the straightforward fabrication of flexible devices, assemblies, and thin films through means such as inkjet printing, spray coating, or roll-to-roll processing. Employing these fabrication techniques has allowed for solution-processed 2D semiconductors to be effectively incorporated into field-effect transistors, photodetectors, solar cells, light-emitting diodes (LEDs), photocatalysts, memory devices, and more.[10-12] Most of the dispersed 2Ds used in devices have been produced by top-down liquid processing techniques, which involve the exfoliation of layered materials in solution followed by extensive post-processing centrifugal separation.[13,14] However, the scale-up of these methods is hampered by poor yields, low throughput, and difficulty in achieving morphological uniformity. Conversely, bottom-up solution-phase syntheses of 2D materials lend themselves better to commercialization, as they utilize the pre-existing chemical manufacturing infrastructure and paradigms.[15] Colloidal chemistry has proven effective in the mass production of 0D semiconductor nanomaterials with fine control of nanocrystal size and morphology. Consequently, the past two decades has seen colloidal semiconductors successfully complete the evolution from small-scale curiosities to

consumer products. Wet chemical methods have successfully accessed a variety of 2D semiconductor nanocrystals,[16] including Sn(S,Se),[17,18] PbS,[19] Ge(S,Se,Te), [20-22] GaSe,[23] InSe,[24] Cd(S,Se,Te),[25] Mo(S,Se,Te)$_2$,[26-28] and various lead halide perovskites.[29] However, achieving high yields of morphologically uniform, individual, unagglomerated crystals *via* solution routes requires extensive reaction and processing optimization. Relative to bottom-up gas-phase deposition techniques, to date it remains a significant challenge to produce monodisperse 2D materials when employing colloidal chemistries.

Among the more intriguing emerging 2D materials is tin(II) sulfide (SnS). The tin sulfides are a family of earth-abundant semiconductors being actively investigated for use in a variety of technological application spaces. Although several stable and metastable phases of 1:1 tin sulfide are accessible, the most thermodynamically favored is the GeS-type orthorhombic α-phase,[30] found naturally as the mineral herzenbergite, and which we will generally refer to hereafter in this report simply as "SnS". The structure of SnS is a compound analogue of black phosphorus, with two-atom-thick layers of Sn and S orthogonal to the [100] direction. Atoms are bonded strongly to three nearest neighbors within the layer, forming a zigzag arrangement in the *b*-direction and an arm chair arrangement in the *c*-direction (see Figure S1).[31] The overall atomic geometry of the crystal can be thought of as a distorted rock salt structure, where the $5s^2$ lone pair electrons of Sn^{2+} lead to the formation of gaps between the two-atom-thick planes due to electrostatic repulsion. Weaker van der Waals interactions between atoms across the gap result in the formation of a pseudo-octahedral coordination environment.[32] The layered atomic structure resulting from these bonding arrangements affords the driving force for SnS to crystallize primarily in 2D morphologies, and imparts electrical anisotropy within the {100} facets of individual 2D crystals. SnS is intrinsically p-type due to the presence of Sn vacancies, which act as shallow acceptors,[33]

resulting in relatively high conductivities ranging from 10^{-4} to 0.1 S / cm.[34] Undoped carrier concentrations of holes are reported to be on the order of 10^{15} cm^{-3} to 10^{17} cm^{-3} with Hall mobilities of up to 90 cm^2 / V·s in single crystals.[35,36] SnS also displays excellent optical properties, including an indirect band gap of 1.07 eV and absorption coefficient values > 10^4 cm^{-1} across the visible and near-infrared spectrum,[37] which is higher than Si and most other absorber materials. Finally, unlike many other semiconductors, SnS is a non-toxic, low-cost compound, making it a promising candidate for widespread commercial application.

Nanocrystals of SnS have been reported using solution-based syntheses in a variety of sizes and morphologies, although there are limited examples of nearly uniform products. Zero-dimensional nanoparticles have been accessed with a high degree of monodispersity as spheres,[17,38-41] cubes,[17,40,42] and tetrahedra.[39,40] Owing to SnS having an exciton Bohr radius of ≈ 7 nm,[43] many of these 0D nanocrystals exhibit an increased band gap due to quantum confinement, a phenomenon which also occurs for thin 2D SnS.[44] Several colloidal methods to prepare 2D nanocrystals of SnS have been developed;[17,38,45,46] however, to date, high-yield syntheses of 2D SnS have been limited to small or intermediate-sized crystals with dimensions of ~ 250 nm or less. The synthesis of larger (>1 μm), high-quality, single-crystalline 2D materials is of nanoelectronic and optoelectronic interest due to the potential for larger mobilities, fewer interface recombination sites in assemblies, and the ability to lithographically fabricate devices using individual crystals. Although colloidal synthesis routes to larger 2D SnS nanosheets[41,42,47,48] and nanoribbons[49-52] have been reported previously, their morphological and dimensional uniformity is limited. To our knowledge, there has been no report of a high-yield solution-based route to μm-scale, monodisperse, single-crystalline 2D SnS nanocrystals.

A pressing technological obstacle for the application of colloidally produced materials in optoelectronics is the lack of a straightforward means to measure the inherent electronic transport properties of the individual synthesized crystals. While structural and optical characterization of semiconductor nanocrystals has become routine, electronic features are substantially more challenging to interrogate. Contact probe and spectroscopic measurements typically are performed on films or superlattices of assembled colloidal nanocrystals;[12,53,54] however, such a strategy does not allow for the disentanglement of the innate carrier transport within individual crystals from that resulting due to charge transfer between separate colloidal domains. Carrier transport is strongly influenced by capping agents,[55] inter-crystalline charge transfer ligands,[56] and packing order.[57] As such, the properties of assemblies are not representative of the individual nanocrystals contained therein, and the full dissemination of inherent electronic behavior for discrete colloidal semiconductors has proven exceptionally challenging. Further, relative to single-crystalline 2D nanomaterials, assemblies of 0D nanocrystals have often been plagued by poor mobility and conductivity resulting from imperfect assembly and the prevalence of surface recombination sites. Although it is desirable to produce devices using individual, high-quality, 2D single crystals of colloidal materials, electrical characterization is rare and generally limited to two-contact measurements,[21,23,52,58-61] while the four-point probe method, which measures the intrinsic conductivity of a material, is rarely achieved. In light of the tremendous interest towards employing colloidal nanocrystals as components of optoelectronic devices, the development of techniques that determine the inherent electronic transport properties of solution-synthesized semiconductors, such as time-resolved terahertz spectroscopy (TRTS),[10,41,62-64] is desperately needed.

Here, we report a comprehensive analysis of the electronic transport properties in individual colloidal semiconductor nanocrystals. First, we present the development of a solution chemistry-based synthetic approach to produce nearly monodisperse μm-scale 2D tin(II) sulfide nanoribbons and square nanosheets using a one-pot, one-step, easily scalable synthetic route. These syntheses represent a rare example in this size regime of essentially uniform, single-crystalline, 2D nanocrystals produced using colloidal chemistry. Next, we detail the structural characterization of these SnS materials, and describe how they are processed from solution to fabricate back-gated, top-contact solid-state devices from individual colloidal crystals. Finally, we interrogate their electronic transport properties using a combination of multi-point contact probe electrical conductivity measurements and time-resolved terahertz spectroscopy. These combined studies allow for the direct determination of carrier concentration, carrier mobility, conductivity, and the majority carrier type within an individual 2D nanocrystal. We report findings illustrating that careful manipulation of solution chemistries can selectively afford products with substantively disparate charge carrier behavior. These measurands are challenging to extract using common experimental practices, and underpins that this metrological strategy represents a significant and valuable advancement in the characterization of colloidally synthesized semiconductors.

RESULTS AND DISCUSSION

Solution Synthesis and Structural Characterization of μm-scale Colloidal 2D SnS. We developed high-yield, solution-based routes to μm-scale 2D crystals of colloidal SnS in two distinct morphologies. Their 2D structure and relatively large in-plane size were essential for the subsequent fabrication of solid-state devices using individual colloidal nanocrystals as the semiconductor component. Concurrently, a high degree of shape and size monodispersity was

desired as, in addition to being an atom-efficient and cost-effective synthetic process, a substantial degree of crystalline homogeneity allowed for bulk structural characterization of the product. To these ends, we pursued a heat-up strategy of nanocrystal synthesis in solution (see materials and methods section for details), as such approaches have proven consistently effective at producing large quantities of monodisperse shape-controlled nanocrystals.[65,66]

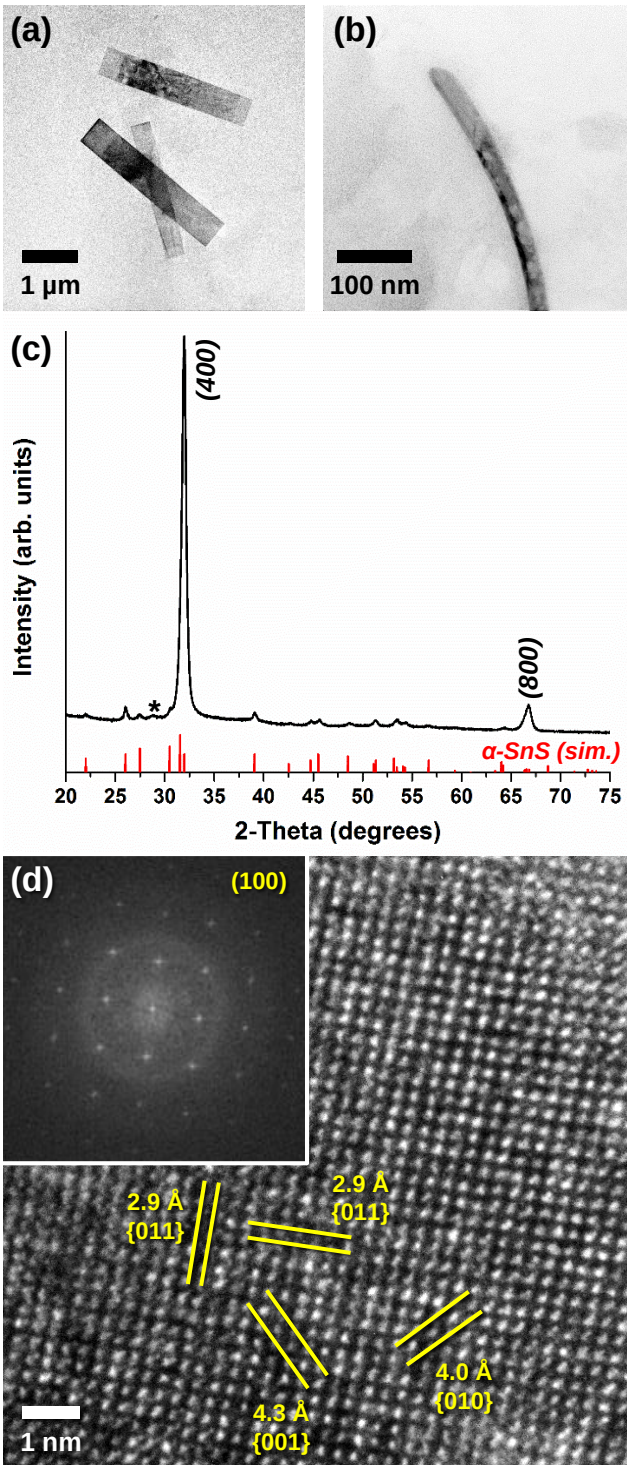

Figure 1. TEM images of μm-scale colloidal SnS nanoribbons, viewed from the (a) top and (b) side, displaying their 2D morphology. (c) Powder XRD pattern of the nanoribbons, which can be indexed to phase-pure orthorhombic α-SnS (* = surface oxide present in air) and displays strong preferred orientation in the [100] direction. (d) HRTEM image of a single SnS nanoribbon and

(inset) the resulting FFT, both of which reveal that they are single-crystalline with a surface that can be indexed to α-SnS(100).

SnS 2D Nanoribbons

One of our devised syntheses produced a high yield of nearly morphologically-uniform, high aspect ratio, 2D SnS colloidal crystals that hereafter we refer to as nanoribbons. Briefly, $SnCl_2$ and elemental sulfur were dissolved in oleylamine (OLAM) solvent and heated to 180 °C (453 K) under an inert atmosphere. The product was collected, separated from solution by centrifugation, and redispersed in toluene. Figure 1a shows a representative transmission electron microscope (TEM) image of the resulting 2D nanoribbons lying flat, and additional images can be found in Figure S2. Statistical analysis of the crystals revealed that our product had a morphological yield of 95 % nanoribbons, with an average length of 2.81 μm ± 0.28 μm (C.V. = 10 %) and width of 0.48 μm ± 0.19 μm among the nanoribbons. Notably, such high yield and monodispersity is rarely reported for bottom-up synthesized colloidal semiconductors in the >1 μm size regime. We found that variations in regent concentration, Sn:S precursor ratio, and temperature all adversely affect the homogeneity of our nanocrystals; however, the reaction is robust enough to tolerate small perturbations to the synthetic conditions. Additionally, the selection of $SnCl_2$ was essential to produce monodisperse nanoribbons as both $SnBr_2$ and Sn acetate yielded mixtures of nanoribbons, likely due to differences in thermal decomposition kinetics afforded by the anion (Figure S3). Figure 1b displays the view of an individual nanoribbon from the side, indicating that the μm-scale crystals possess smooth top and bottom facets with a thickness of approximately 17 nm to 20 nm. Their morphological smoothness was also observed using high-angle annular dark-field scanning TEM (HAADF-STEM), and the few-layer thickness of the nanoribbons was confirmed by atomic force microscopy (AFM) (Figures S4, S5).

The structural composition of the 2D nanoribbons was investigated using powder X-ray diffraction (XRD). The resulting pattern (Figure 1c) was indexed to phase-pure orthorhombic α-SnS (JCPDS No. 73-1859, space group *Pnma*, lattice constants a = 1.118 nm, b = 0.398 nm, c = 0.433 nm). The strong relative intensity of the (400) and (800) reflections indicated substantial preferred orientation towards [100], which is expected as the layered planes of covalently-bound Sn-S extend in the *b* and *c* crystallographic directions (Figure S1). Aside from the reduced relative sharpness of the reflections, due to smaller crystalline domain sizes, the XRD pattern matches well with that collected from commercially-purchased bulk herzenbergite SnS, including a small amount of native surface oxide detectable at approximately 29 °2θ (Figure S6). High-resolution TEM (HRTEM) analysis of the μm-scale nanoribbon surface revealed that they were single-crystalline, free of linear and planar defects such as dislocations and twinning (Figure 1d). Lattice fringes with spacings of 2.9 Å (0.29 nm) were visible between a given atom and its four nearest neighbors, which agrees well with the expected interatomic distance for planes of the form {011}. The (010) and (001) planes were also visible, with interatomic lattice fringe distances of 4.0 Å (0.40 nm) and 4.3 Å (0.43 nm), respectively. A fast Fourier transform (FFT) of the collected HRTEM image (inset) matched well with the [100] zone axis of SnS, in good agreement with our powder XRD results. Selected area electron diffraction (SAED) of an individual nanoribbon produced a pattern which confirmed its single-crystalline nature and can be indexed to α-SnS(100) (Figure S7). Additionally, when compared to the orientation of the nanoribbon being characterized, reciprocal space distances between diffraction spots along the length of the crystal correspond to the SnS<010> directions, while the diffraction spots along the width match that of SnS<001>. This indicates that the nanocrystals grow more favorably along the zigzag *b*-axis relative to the armchair *c*-axis, the latter of which is identified as the lateral direction of the ribbons.

We verified these results by performing HRTEM analysis on the corner of a nanoribbon (Figure S8), and found that the atomic fringes along the length of the crystal matched well to the lattice spacings of SnS(010), and those of the width to SnS(001). These crystalline orientations concur with those previously observed in the case of belt-like SnS nanowires that similarly grew primarily in the <010> directions, which was ascribed to the higher surface energy of the SnS{010} facets relative to those of {100} or {001}.[67]

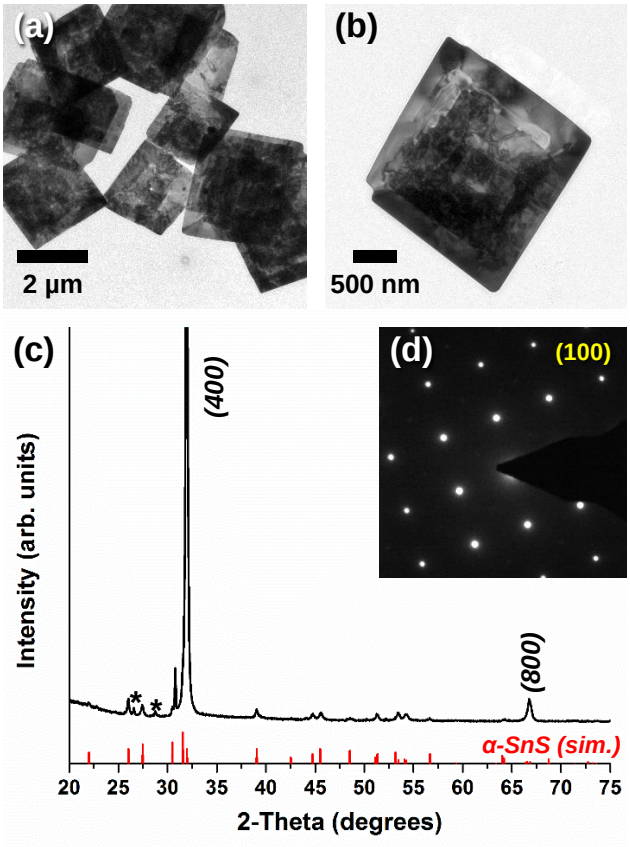

Figure 2. (a and b) TEM images of µm-scale 2D colloidal SnS square nanosheets. (c) Powder XRD pattern of the square nanosheets, which can be indexed to phase-pure orthorhombic α-SnS (* = surface oxide present in air) and displays strong preferred orientation in the [100] direction. (d) SAED pattern collected from an individual square nanosheet, confirming that it is single-crystalline SnS oriented towards the [100] zone axis.

SnS 2D Square Nanosheets

A second synthetic procedure we developed yields SnS square nanosheets with high morphological uniformity. Briefly, an excess of Sn(IV) chloride was heated in OLAM under an inert atmosphere while in the presence of hexamethyldisilazane (HMDS) and elemental sulfur to form μm-scale colloidal 2D SnS nanocrystals. The silvery-dark product was collected, purified by centrifugation, and redispersed in toluene. Figures 2a,b show demonstrative TEM characterization of the resulting square nanosheets (Figure S9 for additional images). Particle counting confirmed that the nanosheets had nearly uniform lateral dimensions of 2.58 ± 0.37 μm per side (C.V. = 14 %), and our synthesis produced a yield of 89 % square nanosheets. Unlike the μm-scale nanoribbons, the SnS nanosheets have an irregular, uneven surface. HAADF-STEM imaging shows the broad face of the nanosheets resemble a series of cliffs and plateaus (Figure S10). The coarse morphology of the nanosheets was further confirmed by AFM, showing a series of steps that rise from the edges of the nanostructure (Figure S11). The nanosheets are also revealed to be substantially thicker than the nanoribbons, with vertical dimensions ranging from 75 nm around the periphery of the nanostructure to 150 nm along the thickest interior regions. The impetus for this unusual morphology is uncertain; although it resembles the terraced morphology that can result from screw dislocation-driven growth, it lacks the distinctive spiral pattern that results from such a mechanism. More likely, it is the result of a nonclassical, kinetic-driven crystallization mechanism such as oriented attachment[68] or the "wedding cake" growth model, which consists of successive adatom-driven nucleation events.[69] The reaction kinetics may be a result of the presence of HMDS during synthesis, which is known to increase the reactivity of Sn complexes it coordinates to and often influences product crystallinity when employed in solution-based syntheses.[45,52] Our use of Sn^{4+}, instead of the Sn^{2+} utilized for nanoribbons, also requires an

additional reduction process to take place during the formation of SnS that could alter nucleation and growth kinetics. We also found that the reaction temperature and an excess of Sn are important synthetic parameters in this synthesis (Figure S12).

Figure 2c shows the powder X-ray diffraction pattern of a drop-cast ensemble of square nanosheets, confirming that they too could be indexed to phase-pure GeS-structural type α-SnS with a small amount of native surface oxide. As with the nanoribbons, the as-prepared nanocrystals were oriented preferably along [100], which is consistent with their layered, anisotropic, 2D structure. The increased sharpness of the reflections, relative to that of the nanoribbons, indicated a larger single-crystalline domain size, which we attribute to both the greater thickness and higher cross-sectional area of the nanosheets. Importantly, the sharpness of the reflections in the XRD pattern suggests that, despite their coarse morphology, these nanocrystals are not polycrystalline. This observation was confirmed by electron diffraction (Figure 2d). The spot pattern produced from SAED revealed that the square nanosheets, or at least very large domain therein, were single-crystalline and that, like the nanoribbons, the surface normal of the nanosheets corresponded to the [100] zone axis. The in-plane orientation of the electron diffraction pattern indicated that the four edges of the nanosheets extended in the zigzag (<010>) and armchair (<001>) directions, while <011> aligned with the corners of the square (Figure S13).

The 2D morphology and large-scale monodispersity of centrifugally washed, drop-cast SnS nanocrystals was verified by scanning electron microscopy (SEM) analysis (Figures 3, S14, S15). The high morphological uniformity of our two products was evident through examination of large-area films of deposited SnS, which show 100 or more nearly identical nanocrystals at a time. The nanoscale thinness of the μm-scale 2D materials (≈ 17 nm – 20 nm for the nanoribbons, ≈ 75 nm

– 150 nm for the nanosheets) is also observable by side view inspection of individual crystals. The difference in flexibility between the morphologies, likely as a function of their thickness, is apparent. Whereas the nanoribbons curve and bend with ease, the square nanosheets stack in a rigid, inelastic manner. The elasticity of drop-cast nanoribbons makes them potentially of interest for flexible devices and straintronics (Figure S16). The distinct tiered structure of the nanosheets was also easily observable; however, each individual crystal appeared to have a distinct pattern of steps and plateaus, despite approximately uniform lateral dimensions. Additionally, we generated elemental maps of SnS nanoribbons and square nanosheets using energy-dispersive X-ray spectroscopy coupled with SEM (SEM-EDX), which confirmed a homogeneous distribution of Sn and S throughout the nanostructures (Figures S17, S18). Notably, SEM-EDX also detected carbon and nitrogen on the 2D nanocrystals, suggesting that molecular surfactants are still adsorbed to the surface of the nanocrystals even after washing.

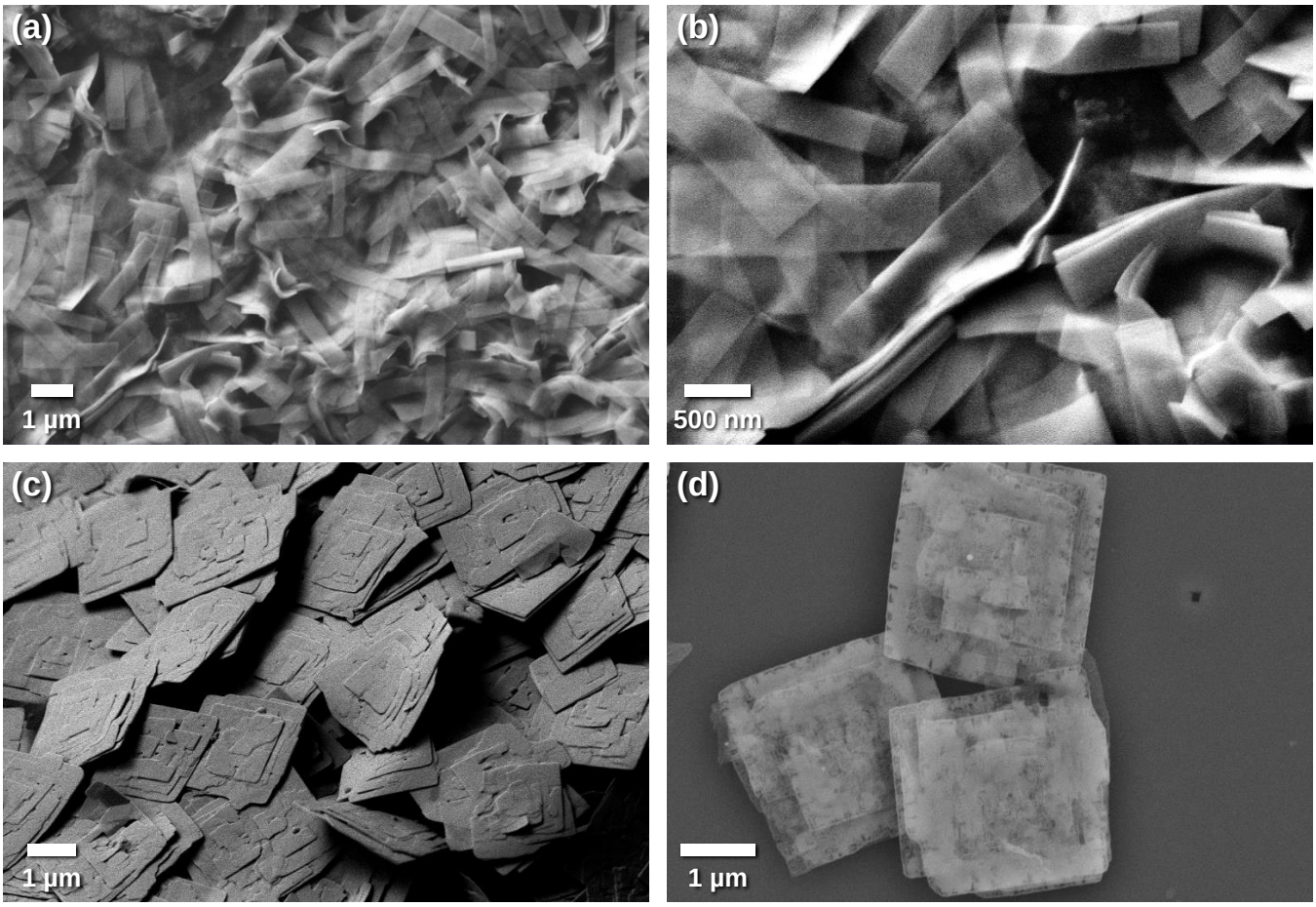

Figure 3. SEM images of (a,b) SnS nanoribbons and (c,d) SnS square nanosheets dropcast on a substrate, indicating the high morphological uniformity of individual crystals within the colloidal solution. The greater rigidity and coarseness of the square nanosheets, relative to the nanoribbons, can also be clearly seen.

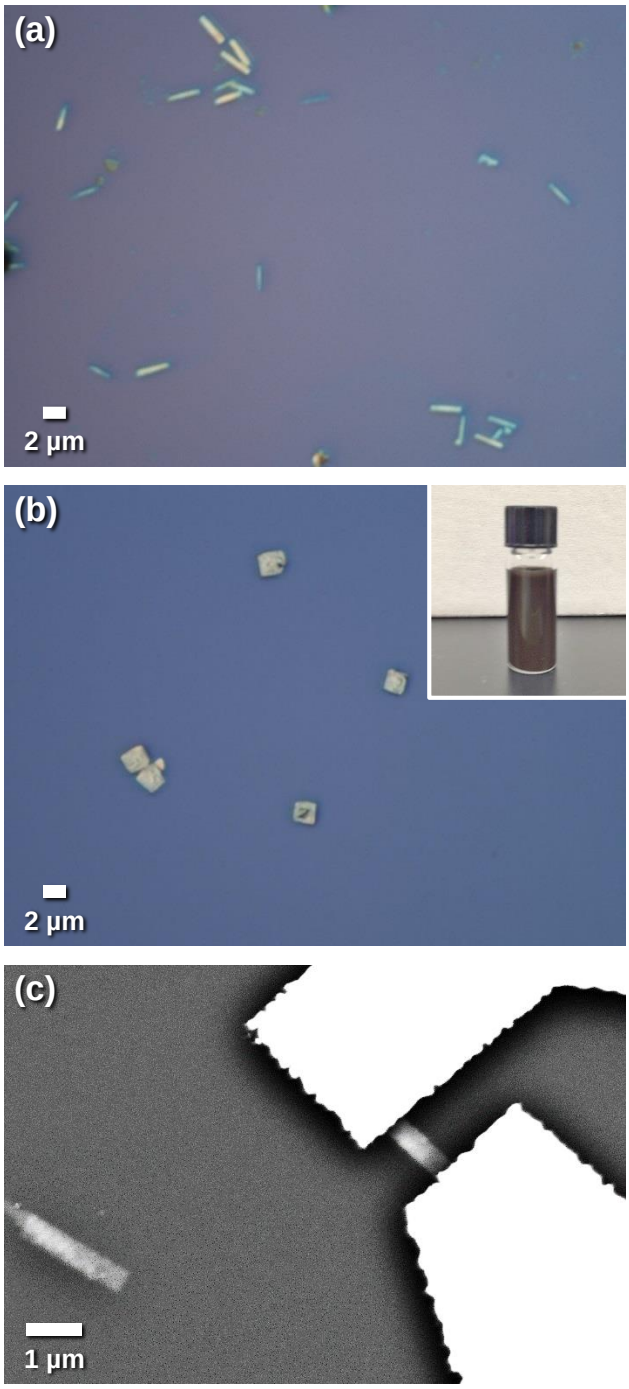

Figure 4. Optical microscopy images of (a) SnS nanoribbons and (b) SnS square nanosheets dropcast from (inset) colloidal solution on p+Si/SiO_2 substrates prior to device fabrication. (c) SEM image of a back-gated, 2-contact device fabricated from an individual SnS nanoribbon that was cast onto the substrate.

Fabrication of Back-Gated Devices from Individual Crystals of Colloidal 2D SnS.

To explore the electronic transport properties of our synthesized 2D SnS nanocrystals, we fabricated back-gated field-effect transistor (FET) devices from individual SnS nanoribbons and square nanosheets taken from solution using standard lithographic techniques. Although long-chain surfactants adsorbed to the surface of the 2D SnS afford colloidal stability and prevent agglomeration of nanocrystals, these organic species are highly insulating and must be removed prior to SEM analysis or device fabrication. Accordingly, first we diluted and centrifugally washed solutions of our samples, which consists of separating the precipitate from the supernatant and then redispersing the former in neat toluene. The effect of this washing step is manifest when the SEM images in Figure 3 are compared to those of unwashed 2D nanocrystals, Figure S19. Without washing, an amorphous matrix of dried organic residue can be seen encapsulating the crystals, preventing both effective charge transfer between domains and the isolation of individual 2D SnS semiconductors for subsequent device fabrication. Drop-casting dilute solutions afforded deposited 2D SnS with a free proximity of 10 μm or more surrounding them, making these regions suitable for the deposition of metal contacts to a series of individual semiconductor nanocrystals (Figure 4). Unlike most exfoliation-based 2D material techniques, using solution-synthesized nanocrystals allowed us to fabricate on the order of 6 – 10 separate devices in each lithographic write, and fabricating up to hundreds at a time is achievable due to the preponderance of nearly uniform 2D materials available on each substrate (supporting information and Figures S20-S23 for more details).

Our initial electronic device measurements revealed that our device did not display ohmic behavior (Figure S24). The nonlinearity of the initial I_{DS}-V_{DS} curves was attributed to a Schottky barrier arising from poor contact between the deposited Cr/Au and the SnS channel. To resolve

this problem, a second annealing step was necessary, this time with the entire device array being treated at 350 °C (623 K) in 5 % forming gas. The subsequent linearity of the I_{DS}-V_{DS} curve is indicative of an ohmic-like interface between the semiconductor and the contact. Previous studies have also shown a marked decrease in contact resistance between SnS and metal contacts following annealing, and this improvement is usually attributed to a solid-state reaction at the interface which results in the formation of a CrS_x or other metal-sulfide compound.[70,71] To ensure that the fidelity of the SnS crystal had been preserved during this reaction and throughout the fabrication process, we performed Raman spectroscopy as a means of structural analysis. As shown in Figure S25, the Raman spectra of 2D SnS as-synthesized, following centrifugal washing, and after the device fabrication process changed minimally, indicating the SnS structure remained intact. A slight hardening of most phonon modes can be attributed to the removal of surface ligands by washing and, especially, by thermal annealing. The peaks matched well with the previously-reported Raman spectra of α-SnS,[37,72] and all are induced from first-order scattering from optical phonons.[30] Further confirmation was provided by powder XRD (Figure S26). Although alloys may have formed at the device interface, SEM-EDX elemental mapping of the devices confirmed that there was no detectable metal diffusion from the contacts into the semiconductor channel during fabrication (Figure S27).[73]

Electrical Characterization of Individual Solution-Synthesized 2D Crystals of SnS.

We explored the electrical properties of solution-synthesized, μm-scale 2D SnS nanocrystals using the test structures fabricated from single nanoribbons and square nanosheets. A schematic of the completed top-contact, back-gated FET devices is displayed in Figure S28. First, output characteristics of individual 2D SnS nanocrystals were collected using a two-terminal configuration at room temperature in the dark. Evaluation of the devices was performed without

ambient light to avoid the generation of photocurrent, as the high absorptivity of SnS in the visible spectrum, which lends itself towards application in photodetectors and photovoltaics, is well-documented.[37,74] Figure 5 shows typical I_{DS}-V_{DS} curves generated from output measurements of individual solution-synthesized SnS nanoribbons while varying the back gate bias, V_{GS}, between – 40 V and 40 V. The linearity of the output curves indicated that the interface between the contacts and the semiconductor was ohmic-like. Additionally, gate action was observed in that the drain-source current showed a consistent response to applied V_{GS}; as the back gate bias became more negative, the output current increased. This is indicative of an injection of holes, and implies that the Fermi level within the band gap lies towards to the top of the valence band of SnS.

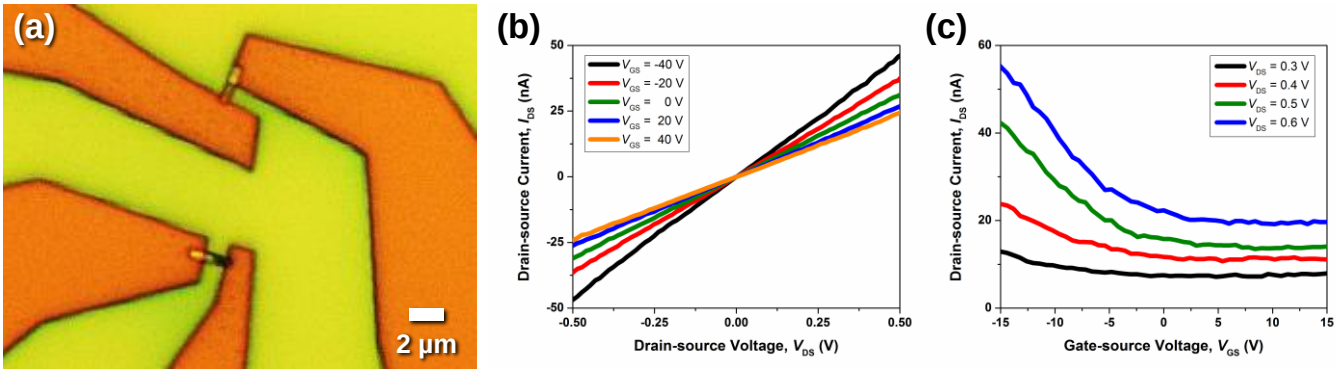

Figure 5. Back-gated two-contact devices fabricated from individual colloidal SnS nanoribbons. (a) Representative optical microscopy image and the resulting room temperature (b) output (I_{DS}-V_{DS}) and (c) transfer (I_{DS}-V_{GS}) characteristics. The output characteristics confirm ohmic contact between the metal and semiconductor. The p-type behavior observed in the transfer characteristics confirm that holes are the majority carrier in the SnS nanoribbons.

Transfer characteristics of a nanoribbon device, generated by sweeping the back gate voltage V_{GS} with an applied bias V_{DS} ranging from 0.3 V to 0.6 V, are displayed in Figure 5c. The measured drain-source current decreased with a more positive V_{GS}, reinforcing their p-type semiconductor character. This hole-dominated carrier transport is expected, as the relatively low formation

energy of Sn vacancies generally results in an excess of holes for bulk, thin film, and nanoscale SnS,[33,75] thereby resulting in intrinsic p-type conductivity.[34,35] The consistent influence of V_{GS} on I_{DS} indicates that these devices function as FETs; however, the relatively low subthreshold slope and the inability to fully turn the devices off limit their effectiveness in this application. Notably, the room temperature FET performance of these colloidally synthesized single-crystalline SnS devices, while modest, is comparable to those using exfoliated and vapor-deposited 2D SnS.[52,76-78] Previous reports of single-crystalline 2D SnS (and SnSe) FETs displayed poor on/off ratio, no higher than 10 and as low as 1.5, with a fully "off" current in the tens of nA. This appreciable "off" current has been attributed to strong carrier screening that prevents the induction of effective switching behavior by the field effect of the gate. SnS inherently has a relatively short Debye screening length,[77] which results in a depletion of carriers towards the bottom of the channel but a shunting effect as carriers continue to pass beyond screening length near the top surface. The poor gate tuning behavior of SnS FETs was somewhat ameliorated by thinning the channel down to several 10s of nm.[77] Although this could explain a low gate response in our thicker 2D square nanosheets, the SnS nanoribbons are only 20 nm or less in height. We therefore ascribe the inability to turn our nanoribbon devices off to the relatively thick (300 nm) SiO_2 dielectric layer, and posit that improved device performance could be achieved by employing either a dielectric layer on the order of 30 nm or a top-gated configuration.

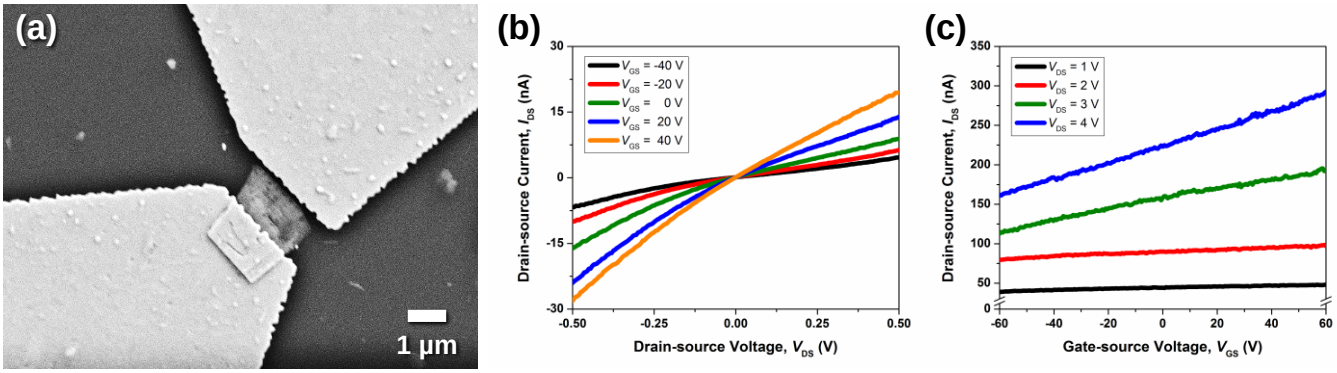

Figure 6. Back-gated, two-contact devices fabricated from individual colloidal SnS square nanosheets. (a) Representative SEM image and the resulting room temperature (b) output (I_{DS}-V_{DS}) and (c) transfer (I_{DS}-V_{GS}) characteristics. Although limited current and gate action is observed, n-type ohmic behavior is displayed indicating, unlike nanoribbons, electrons are the majority carrier.

The output current of the SnS square nanosheet devices displays an ohmic response that is consistently lower than that of nanoribbons with similar channel dimensions. As seen by the two-contact I_{DS}-V_{DS} behavior illustrated in Figure 6, I_{DS} is consistently half or less than that of the nanoribbons for a given applied bias and back gate voltage. These devices display a consistent response to applied V_{GS}; but surprisingly, the current increased with higher applied back gate potential, suggesting that electrons, not holes, were the majority carrier in these solution-synthesized 2D materials. This was corroborated by the collected transfer curves of the devices (Figure 6c), which confirm the n-type character of the square nanosheets. The field effect-induced gate action is even lower than that of the nanoribbons, with a nearly linear subthreshold slope, which was not unexpected considering their larger channel height. As mentioned above, SnS generally exhibits p-type transport behavior due to the thermodynamic favorability of forming Sn^{2+} vacancies, and these defects' ability to act as shallow acceptors.[75] The n-type conductivity measured in our SnS square nanosheets represents one of the few reported cases of electrons acting as the majority carrier. Previously, this has been achieved in SnS through external doping using elements such as Pb or Cl,[79] and, notably, isoelectronic black phosphorus was recently n-doped by surface deposition of silicon nitride.[80] Although we did not deliberately dope our square nanosheets, we hypothesize that HMDS or $SnCl_4$, neither of which were present during the synthesis of the nanoribbons, may have acted as a source of extrinsic Cl, Si, or N dopants. To test

this theory, we performed detailed X-ray photoelectron spectroscopy (XPS) analysis on the square nanosheets. As seen in Figure S29, Cl 2p and Si 2p photoelectrons were not detected at the surface of the nanocrystals. Nitrogen is observed in the centrifugally washed samples; however, this is due to OLAM surfactant adsorbed to the nanosheet surface. Following removal of the ligands by annealing the signal due to the N 1s photoelectrons is no longer present, in agreement with FTIR data (Figure S21), indicating that there does not appear to be extrinsic doping.

An alternative explanation of the n-type behavior exhibited by the square nanosheets is intrinsic doping, specifically a disproportionally Sn-rich stoichiometry. Quantitative EDX elemental analysis of a wide-area, large ensemble of nanocrystals found that the μm-scale SnS nanoribbons had a slight excess of sulfur (Figure S30), in conjunction with most previous reports of nanoscale and bulk SnS.[38] Conversely, the elemental stoichiometry of the SnS square nanosheets, determined by ensemble EDX measurements (Figure S31), indicated a ≈ 7.5 % majority of tin, which is a significant margin of difference even when accounting for the limitations of quantitative EDX. Non-stoichiometry is known to be an effective means of switching the majority carrier from holes to electrons in metal chalcogenides, both through the formation of anion vacancies[81] and the presence of excess cations.[82] Indeed, an excess of Sn or deficiency of S has previously resulted in n-type SnS.[76,83,84] The Sn-heavy elemental composition of the square nanosheets, and its resulting influence on carrier transport and band structure, can result from either a deviation in stoichiometry within the crystal lattice, including the formation of S vacancies, or from cationic Sn Lewis acid complexes adsorbed to the surface.[56,85] We believe this is a reasonable explanation for the n-type behavior of these nanocrystals, especially in light of the excess Sn^{4+} present during their synthesis, which was not the case for our 2D nanoribbons. However, we note that extrinsic doping at

concentrations below the limits of XPS detection cannot be discounted as a possible source of this unexpected charge transport.

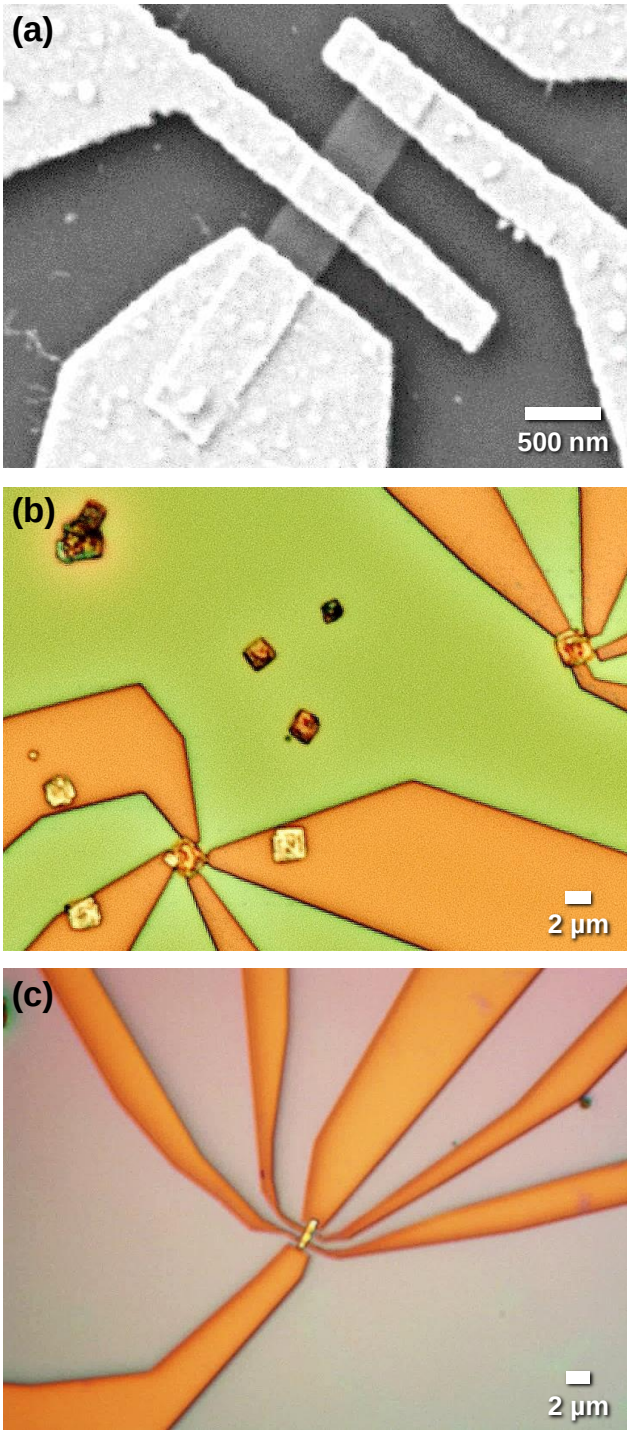

Figure 7. (a) SEM and (b and c) optical microscopy images of more complex back-gated device architectures fabricated from individual colloidal SnS nanoribbons and square nanosheets with 3 or more separate metal contacts.

We hypothesized that the relatively low currents displayed by our nanosheets may be due to oxide formation. XPS analysis confirmed the presence of a thin native surface oxide, but of insufficient thickness to strongly affect device performance (Figure S32). A more likely impetus to the modest currents measured in our two-terminal SnS devices are oxides resulting from our choice of contact metal. Although Cr is commonly used as a semiconductor-contact adhesion layer due to its low work function, which is especially important for facilitating charge transfer to n-type semiconductors, it has been reported to form insulating oxides (CrO_x) at the interface during deposition, even under high vacuum conditions.[71] These oxides, which also can form with other common low work function contact metals such as Ti, will act as a Schottky barrier to the channel, assuming no Fermi level pinning. Indeed, we recently have found that higher work function metals significantly improve the performance of our two-terminal SnS devices.[86] This uncertainty about the band alignment of our contacts underpins the importance of performing four-point measurements, instead of two-point measurements, when extracting the fundamental electronic properties of our materials.

To determine the inherent conductivity of the individual solution-synthesized SnS nanocrystals, devices with additional contacts were patterned (Figure 7). These are among the smallest many-terminal devices ever fabricated from individual 2D semiconductor crystals, and approach the scaling limit for our lithographic process. Using four-point probe techniques, with a linear arrangement of terminals along the length of the nanoribbons (Figure S33) and a van der Pauw arrangement on the square nanosheets (Figure S34), allowed for deconvolution of contact

resistance from the inherent resistance of the material. Our SnS nanoribbons had an average room temperature resistivity of 10.3 Ω·cm, which corresponds to a conductivity (σ) of 0.097 S / cm and compares favorably to the conductivity of single-crystalline SnS reported elsewhere.[33] As determined using SAED and HRTEM, the length of the ribbon corresponds to the *b*-axis zigzag structural orientation of the anisotropic SnS crystal. Previous reports[74,76,78] confirmed that the conductivity is higher in this direction, relative to that of the armchair direction, and so, although the ribbon width is too narrow for direct four-probe measurement, we can reasonably postulate that the conductivity along this direction would be lower. By comparing the device resistance obtained from two-point measurements with the channel resistance extracted from four-point results on the same nanoribbon, the magnitude of contact resistance may be quantified by

$$R_{\mathrm{contact}_{2,3}} = \frac{1}{2}\left(R_{\mathrm{device}_{2-3}} - R_{\mathrm{channel}_{2-3}}\right) = \frac{1}{2}\left(\frac{dV_{\mathrm{DS},2-3}}{dI_{\mathrm{DS},2-3}} - \frac{dV_{2-3}}{dI_{\mathrm{DS},1-4}}\right) \qquad (1)$$

for a linear arrangement of 4 contacts, and assuming contacts 2 and 3 have an equal resistance, R_{contact}. Our average measured two-point resistance between contacts 2 and 3 was 5.21 x 10^6 Ω, which indicates that the contact resistance of these devices was in the range of 8.5 x 10^4 Ω. This indicates that, although our contacts function reasonably well, further engineering of the semiconductor-metal band alignment could improve device performance.

Four-point probe analysis of the square nanosheets utilized a van der Pauw configuration, which affords measurements along two directions set off 90° from each other, in this case corresponding to the edges of the square nanocrystals. We found the measured resistances to be highly anisotropic, with an average value of 5.35 x 10^5 Ω in one direction and 8.55 x 10^5 Ω for the orthogonal in-plane direction, yielding an overall room temperature value of ρ = 23.1 Ω·cm. This corresponds to a conductivity of 0.043 S / cm and confirms that the solution-synthesized SnS square nanosheets are less conductive than the SnS nanoribbons. However, it is important to note

that the resistivity value determined for the square nanosheets assumes isotropic in-plane carrier transport, which is not the case for 2D nanocrystals of SnS. Indeed, our measured resistance along one edge of the square nanosheet was 1.6 times higher than along the other. Although we cannot verify it structurally, considering previous experimental and computational transport studies of SnS single crystals[74-76,87] we can reasonably assume that the direction of lower resistance corresponds to the zigzag *b*-axis, and the higher resistance is along the orthogonal armchair *c*-axis. These measurements confirm the impact of structural orientation on device performance and underpin the importance of probing electronic transport anisotropy in solution-synthesized colloidal nanocrystals.

Extracting the Electronic Transport Properties through a Combination of Four-Point Probe and Time-Resolved Terahertz Spectroscopy.

Accurate measurement of the intrinsic charge carrier mobility, and subsequently the carrier concentration, is often a major challenge in the characterization of low-dimensional materials. Field-effect mobility (μ_{FET}), extracted from the transfer curve of a FET device, is frequently reported; however, unaccounted for contact resistance or device-substrate interactions produce error that often leads this value to be underestimated and inconsistent.[88] Our attempt to extract μ_{FET} from the linear region of device transfer measurements at several low V_{DS} values yielded discrepant results (Scheme S1). Magnetotransport Hall measurements of fabricated test structures, yielding the Hall mobility (μ_H) of the material, is regarded as a more effective approach of elucidating the carrier mobility of a semiconductor.[89] Unfortunately, reliable magnetotransport measurements on the nm-scale are complicated by the small spacing between electrical terminals and associated lithographic limitations. As an alternative to Hall measurements, we turned to time-resolved terahertz spectroscopy to determine the charge carrier mobility. TRTS has emerged as a

useful technique for the investigation of electronic transport properties in colloidal semiconductor nanocrystals,[41,62,63] and recent reports have indicated that the carrier mobility values generated from TRTS (μ_T) are comparable to μ_H.[10,64]

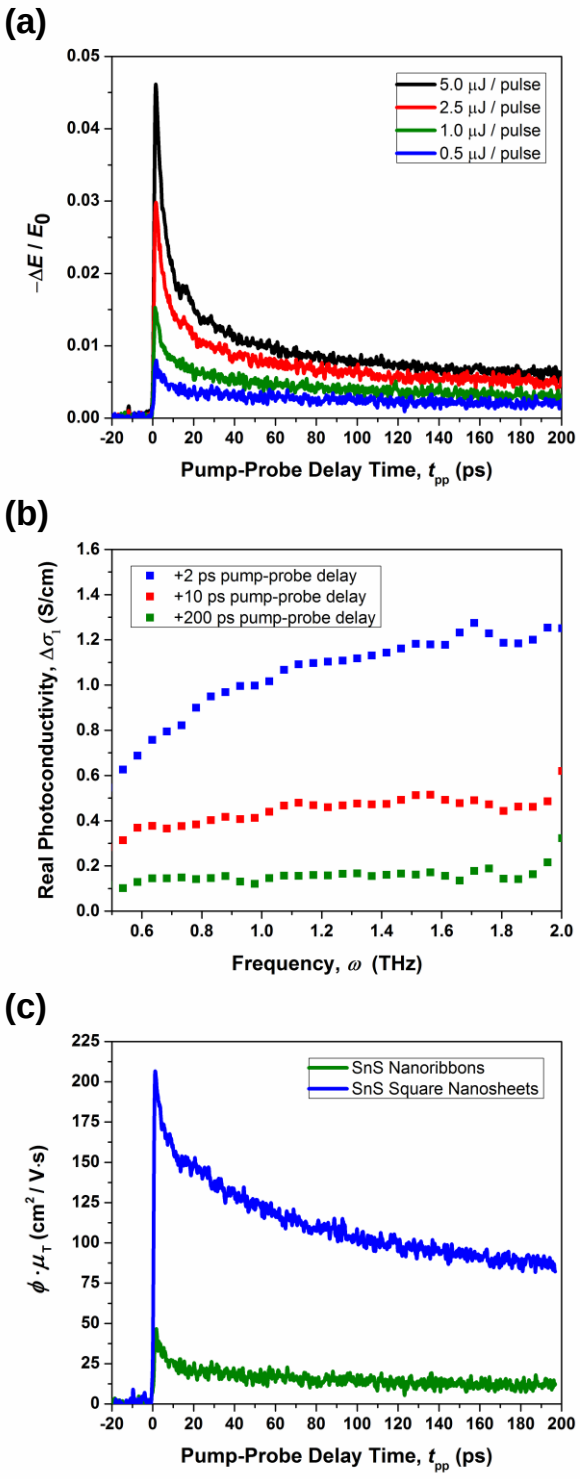

Figure 8. Terahertz mobility, μ_T, of solution-synthesized 2D SnS nanocrystals determined by TRTS at room temperature. (a) Fluence-dependence of ΔE / E_0 for SnS nanoribbons at pump-probe delay times, t_{pp}, 0 to 200 ps using 800 nm pump excitation. (b) Frequency-dependence of the real part of the generated change in photoconductivity in SnS nanoribbons with a pump fluence of 0.5 μJ / pulse, indicating that at low frequencies and longer pump delay times it nearly matches the measured electrical conductivity of ~ 0.1 S/cm. (c) The product of the carrier photogeneration yield and terahertz mobility at t_{pp} 0 – 200 ps when pumped with a fluence of 0.5 μJ / pulse, as determined using Equation 7, for both SnS nanoribbons and SnS square nanosheets.

TRTS is an ultrafast spectroscopic technique that utilizes a visible pump and far-infrared probe to generate and interrogate the dynamics of free charge carriers. The materials' photoconductivity can be approximated by measuring the change in transmission of a THz frequency probe wave packet following photoexcitation with visible light above the band gap energy. The probe waveform (covering frequencies 0.3 THz to 2.0 THz) was collected from samples of drop-cast centrifugally washed 2D SnS nanocrystals both following 800 nm excitation and again with the pump beam blocked, the latter scenario hereafter referred to as terahertz time-domain spectroscopy (THz-TDS). For TRTS, the delay between the pump and gate pulses, t_{pg}, was held constant at the point of maximum attenuation in the electric field transmission waveform relative to the unpumped THz-TDS waveform (Figure S35), while the pump-probe delay time, t_{pp}, was varied between 0 ps and 200 ps to monitor the magnitude of change in THz probe transmission due to photogenerated free carriers (Figure 8a).

The time-dependent photoconductivity was calculated from the optically induced decrease in THz transmission following photoexcitation using the thin film equation,[90] which is valid because our deposited nanocrystal films are substantially thinner (≈ 3-4 μm) than the wavelength of the probe radiation (hundreds of μm):

$$\Delta\sigma(t_{pp}) = -\left(\frac{\Delta E(t_{pp})}{E_0}\right)\left(\frac{n_{THz}+1}{Z_0 d}\right) \quad (2)$$

where $\Delta E(t_{pp})$ is the differential change in transmission, relative to the TDS measurement, at the peak of the THz probe waveform resulting from a photoexcited sample at pump-probe delay t_{pp}, E_0 is the sample transmission at the same point in the THz waveform without photoexcitation, n_{THz} is the index of refraction of the substrate at THz frequencies, Z_0 is the impedance of free space, and d is the thin film thickness (additional details, Figures S36, S37).

Measurement of ΔE / E_0 (Figure 8a), and therefore the transient photoconductivity, is a function of both the pump-probe delay time, t_{pp}, and the pump fluence. At very early pump-probe delay times, hot carriers with excess energy quickly relax to their respective band edges through phonon emission before reaching a long-lived state (ns timescale) where ΔE / E_0 decay occurs gradually through recombination mediated by typical Auger or Shockley-Read-Hall processes. This temporal stage several picoseconds after excitation is more representative of the inherent mobility of charge carriers within a given material, and so we and others focus our analysis on, in this case, pump-probe delay times of t_{pp} = 10 ps or greater.[10,62,63,91,92] By employing Equation 2 and performing a Fourier transform on the THz transmission differential waveforms for a deposited film of known thickness (Figure S38), we obtain the frequency-dependent real and imaginary conductivity. At low frequencies and longer pump-probe delay times, we found that $\Delta\sigma_1(\omega)$ was close to the DC conductivity determined from our four-point probe measurements when pumped with an excitation of 0.5 μJ / pulse (Figure 8b). Therefore, we selected this low fluence for our carrier transport measurements, as photogenerating too many electron-hole pairs can influence the mobility due to carrier crowding and increased Auger recombination. Importantly, at later t_{pp} the real photoconductivity $\Delta\sigma_1(\omega)$ was largely frequency-independent and the imaginary portion of the photoconductivity $\Delta\sigma_2(\omega)$ was positive across all measured frequencies (Figure S39). These

findings indicate Drude-like charge transport with isotropic scattering and minimal back-scattering at defects or interfaces.[41,92]

To determine the photogenerated carrier mobility in our samples, we utilize the following equation (see Scheme S2):

$$\mu_T(t_{\mathrm{pp}}) = -\left(\frac{\Delta E(t_{\mathrm{pp}})}{E_0}\right)\left(\frac{n_{\mathrm{THz}}+1}{Z_0 e\varphi FA}\right) \qquad (3)$$

where φ is the charge carrier photogeneration efficiency, F is the excitation fluence, A is the absorbance, and μ_T is the terahertz mobility, which is equal to the sum of the carrier mobilities, ($\mu_e + \mu_h$). The resulting time-dependent μ_T values for our 2D SnS nanocrystals is presented in Figure 8c. In our analysis, φ is assumed to be at or nearly unity, which is reasonable considering the strong absorptivity of SnS. However, we note that the values presented represent a lower bound to our mobility calculation. As with the ΔE / E_0 values, the mobility quickly decreases within the first several ps following excitation, likely from carrier-to-phonon cooling, and then gradually diminishes over time due to carrier recombination, which is not incorporated into Equation 7. We extract our room temperature μ_T value from the spectra at t_{pp} = 10 ps, where we can safely assume that all hot carrier energy transfers have ceased and very limited carrier recombination has taken place, yielding values of μ_T = 26.5 cm^2 / V·s for the SnS nanoribbons and 158.0 cm^2 / V·s in the square nanosheets. Although TRTS is an ensemble measurement, the high monodispersity of the samples allows us to assume that the mobility values extracted are confined within an individual crystalline domain if the diffusion length, L, is substantially shorter than the lateral size of our 2D nanocrystals.[10,41] Using the Einstein relation, $L = (\tau \mu_T k_B T/e)^{1/2}$, at τ = 10 ps we find L is only on the order of 26 nm in our SnS nanoribbons and 64 nm for our square nanosheets, confirming that backscattering at the edges should not be strongly limiting our mobility measurement.

A major limitation of the TRTS technique is that the extracted mobility corresponds to a combination of both electron and holes, while disentanglement of the individual free carrier mobilities remains challenging. Obtaining the majority carrier mobility of semiconductor is desirable because it is a more accurate representation of the material performance in electronic devices, and potentially allows for the calculation of the room temperature carrier concentration if the materials' conductivity is known. In an effort to ameliorate this issue, we devised an approximation to deconvolute the individual carrier mobilities from the combined values captured by TRTS (see Scheme S3). By assuming that carrier scattering at room temperature is primarily due to acoustic phonon scattering and that transport in these layered 2D materials is overwhelmingly in-plane,[4,87,92] we derived the following relationships for TRTS-measured in-plane carrier mobility of holes ($\mu_{h,xy}$) and electrons ($\mu_{e,xy}$):

$$\mu_{h,xy} = \frac{\mu_T}{1+\left(\frac{m^*_{h,xy}E_{d,h}}{m^*_{e,xy}E_{d,e}}\right)^2} \quad \text{and} \quad \mu_{e,xy} = \frac{\mu_T}{1+\left(\frac{m^*_{e,xy}E_{d,e}}{m^*_{h,xy}E_{d,h}}\right)^2} \tag{4}$$

where m^* is the carrier effective mass and E_d is the deformation potential for that carrier. Using values of m^* and E_d collected from reported density functional theory (DFT) calculations (Scheme S4), we find that the in-plane mobility of the majority carriers for our 2D SnS nanocrystals is $\mu_{h,xy}$ = 4.8 cm^2 / V·s in the nanoribbons and $\mu_{e,xy}$ = 158 cm^2 / V·s for our square nanosheets.

The anisotropic conductivity we observed in our Van der Pauw measurements, which has also been predicted and observed by others in single-crystalline SnS,[74,76,77] is primarily due to disparate mobilities in the zigzag and armchair directions, and thus likely manifest by differences in reduced mass and deformation potential experienced by a charge carrier in these directions. We estimate the zigzag and armchair contribution to the composite in-plane carrier mobility of 2D SnS using the following expressions (Schemes S5, S6),:

$$\mu_{\mathrm{x}} = \sqrt{\left(\frac{m_{\mathrm{x}}^{*} E_{\mathrm{d,x}}}{m_{\mathrm{y}}^{*} E_{\mathrm{d,y}}}\right)}\,\mu_{\mathrm{xy}} \qquad \text{and} \qquad \mu_{\mathrm{y}} = \sqrt{\left(\frac{m_{\mathrm{y}}^{*} E_{\mathrm{d,y}}}{m_{\mathrm{x}}^{*} E_{\mathrm{d,x}}}\right)}\,\mu_{\mathrm{xy}} \tag{5}$$

where x and y denote two orthogonal in-plane directions within a 2D or layered material, using reported values of effective mass and deformation potential for a given carrier type.[87] A summary of the results can be found in Table 1. In the p-type nanoribbons we estimate hole mobilities of 5.8 cm^2 / V·s along the zigzag direction and 3.9 cm^2 / V·s in the armchair direction, while for the n-type square nanosheets the electron mobilities are 170 cm^2 / V·s and 97 cm^2 / V·s along zigzag and armchair, respectively. This indicates a ~ 1.5 times higher mobility for holes in the zigzag direction, relative to armchair, in our SnS nanocrystals and likewise a ~ 1.75 times higher mobility of electron carriers along the zigzag direction, relative to armchair. These values are comparable to what has been previously reported for 2D SnS and other anisotropic 2D materials. [74,76,77] The ratio of μ_e to μ_h of ~ 4.5 that we report is somewhat higher than expected,[93] but this may be due to our mobility relation's dependence of the square of the effective mass, rather than the linear approximation between μ and m^* that is often reported.

Finally, the carrier concentrations of our 2D colloidal SnS nanocrystals were calculated using the four-point probe-measured conductivity and our direction-dependent estimated majority carrier mobility values. The results (Table 1) indicated that the SnS nanoribbons have several orders of magnitude higher carrier concentration of holes (1.04 x 10^{17} cm^{-3}) relative to the concentration of free electrons found in our square nanosheets (2.07 x 10^{15} cm^{-3}), which accounts for the former's higher conductivity despite substantially lower carrier mobility. According to Kröger-Vink defect chemistry theory,[94] the higher carrier concentration and lower mobility of the nanoribbons, relative to the square nanosheets, collectively suggest that they possess a larger population of vacancies. While surface passivation of the nanoribbons with Sn complexes or other

metal cations likely would improve the carrier mobility by eliminating surface trap states resulting from Sn vacancies, it is probable that doing so would result in a concomitant decreased density of free carriers. We hypothesize that a relatively small concentration of sulfur vacancies would engender the high μ_e, but also markedly lower n_e, exhibited by the square nanosheets. Indeed, previous calculations have indicated that small concentrations of sulfur defects in SnS lead to a markedly lower carrier concentration relative to typical tin-deficient bulk SnS.[95]

SnS Material	Conductivity (S / cm)	Mobility (cm^2 / V·s) [direction undefined]	Majority Carrier Concentration (cm^{-3})	Mobility (cm^2 / V·s) [approximated zigzag]	Mobility (cm^2 / V·s) [approximated armchair]
Nanoribbons, this work	0.097 (zigzag)	holes: 4.8 electrons: 22	1.04 x 10^{17}, holes [p-type]	holes: 5.8 electrons: 29	holes: 3.9 electrons: 16
Square nanosheets, this work	0.043 (in-plane)	electrons: 130 holes: 29	2.07 x 10^{15}, electrons [n-type]	electrons: 170 holes: 35	electrons: 97 holes: 23
Single crystals, consensus from literature	~ 0.01 - ~ 0.2	10 - 90	10^{13} - 10^{17}, holes	(1.15 - 2.5 times higher μ in zigzag direction relative to armchair)	
Thin films, consensus from literature	~ 0.001 - ~ 0.07	0.8 - 37	10^{14} - 10^{17}, holes 10^{15}, electrons	--	--

Table 1. Summary of the electronic transport properties obtained from our combined four-point probe and TRTS measurements on solution-synthesized colloidal nanocrystals of 2D SnS. For comparison, a summary of previously reported transport properties obtained from Hall measurements on both single-crystalline and thin films of SnS is provided. All SnS samples are undoped and results are at room temperature. See also supporting information, Table S1.

When compared to previous measurements of SnS electronic transport properties (Table S1 and summarized in Table 1), we find that our values correspond well with bulk SnS, which is expected as the thinness of our μm-scale 2D nanocrystals is not sufficient for quantum confinement. This outcome underscores the comparable crystal quality and electrical properties that are achievable when employing easily, scalable solution-based, colloidal syntheses relative to vapor-based

techniques. While the electrical properties of solution-synthesized semiconductors are typically measured across large assemblies of nanocrystals, resulting in extraneously high resistivities due to losses from inefficient charge transfer between domains, the consensus between our measurements and preceding reports substantiates the veracity of our proposed metrological strategy. Although our measured carrier mobilities are comparable to exfoliated ultrathin transition metal dichalcogenides and higher than most solution-synthesized organic semiconductor or nanocrystal assembly devices, we stress that TRTS has the potential to slightly underreport carrier mobilities, as a photocarrier generation rate less than unity and a nontrivial population of photoinduced carriers lost to recombination at early pump-probe delay times will diminish μ values.

These results conclusively demonstrate that colloidal nanocrystals can exhibit a substantial, yet inconspicuous, disparity in electronic transport properties. Despite being grown using similar precursors and reaction conditions, producing 2D materials of equivalent crystalline structure, our SnS nanoribbons and square nanosheets possessed dissimilar transport properties. This highlights the crucial role of judicious and precise synthetic parameter selection, and emphasizes how indispensable these measurements are towards the development of colloidal nanostructures appropriate for electronic and optoelectronic applications. As thorough investigations of inherent electronic transport in discrete nanocrystals are rare to date, this study may serve as a roadmap to the characterization of future solution-synthesized 2D electronic material systems.

CONCLUSIONS

In summary, colloidal solution-based routes were applied to achieve nearly monodisperse, single-crystalline, 2D SnS semiconductor nanocrystals in high yield using low-temperature, one-

pot chemistries. Two distinct morphologies of 2D SnS were accessed, and utilized to demonstrate an innovative metrological strategy to extract the intrinsic electronic transport properties of these colloidal 2D nanocrystals by employing a combination of four-terminal and TRTS measurements. The conductivity/resistivity and majority carrier were determined using four-point probe techniques on solid-state devices fabricated from individual SnS nanoribbons and square nanosheets. We proposed an interpretation of TRTS data which deconvolutes the intrinsic electron and hole mobility in each of our nanocrystal morphologies, as well as providing an estimation of the relative carrier transport along disparate crystallographic directions within an anisotropic crystal structure. These results were summarily combined to afford a quantification of their carrier concentration. We found that our SnS nanoribbons and square nanosheets had unexpected and substantially dissimilar electronic transport properties, likely due to differences in their synthetic procedure, which illustrates the importance of pursuing these less routine measurands when conducting nanocrystal characterization. Colloidal SnS is an attractive model system to illustrate the potential for bottom-up synthesized 2D materials to be manufactured cost-effectively and subsequently integrated into functional composites or utilized as building blocks for the construction of solution-processed nanoelectronic devices. The routine quantification of the full electronic transport properties of colloidal 2D materials will prove invaluable toward their eventual incorporation into commercial electronic or optoelectronic applications, and we believe that the metrological strategy laid out herein will prove applicable and of paramount importance to the characterization of other solution-synthesized semiconductor nanocrystal systems.

MATERIALS AND METHODS

Materials. Tin(IV) chloride (99.995 %), tin(IV) bromide (99 %), tin(II) acetate, tin(IV) acetate, sulfur powder (99.98 %), and oleylamine (70 %, technical grade) were purchased from Sigma-Aldrich. Tin(II) chloride (99 %), tin(II) bromide (99.2 %) hexamethyldisilazane (>99 %), tri-*n*-octylphosphine (90 %, technical grade), and tin(II) sulfide powder (99.5 %) were purchased from Alfa Aesar. Poly(methyl methacrylate) 495 A4 and 950 A4 were purchased from Microchem. Hydrofluoric acid (49 %) was purchased from J.T. Baker. Solvents, including toluene, ethanol, and acetone, were of analytical grade. All chemicals were used as received.

Synthesis. All reactions were performed under an argon atmosphere using standard Schlenk techniques. Micrometer-scale colloidal 2D SnS nanoribbons were synthesized using the following developed heat-up route. First, 0.032 g (1 mmol) of sulfur was dissolved in 10 mL of oleylamine (OLAM), forming an orange solution, and then added to a 25 mL three-neck flask containing a magnetic Teflon-coated stir bar and equipped with a condenser fitted to a Schlenk line. 0.0948 g (0.5 mmol) of $SnCl_2$ was then added directly into the reaction vessel. The temperature was controlled using a digital controller with glass-coated thermocouple (Gemini, J-KEM Scientific) and a 25 mL heating mantle (Glas-Col). After sealing the flask with a glass stopper, it was evacuated and the solution was heated to 120 °C (393 K) with vigorous stirring. The temperature was maintained for 20 min to remove residual water. After putting the reaction solution under an argon blanket, the temperature was raised to 180 °C (453 K) at ~ 5 ° / min, causing the solution to turn from orange to dark brown, and maintained at that temperature for 1 h before quenching the reaction by immersing the flask in cold water. SnS nanoribbons were separated from the reaction solution by adding 30 mL of ethanol antisolvent and centrifuging at 5000 rpm (524 rad / s) for 1 min. After decanting the yellow supernatant, the precipitate was redispersed in toluene and centrifuged at 3000 rpm (314 rad / s) for 1 min. The clear supernatant was discarded, and the

precipitate was redispersed in toluene before being centrifuged a final time at 2000 rpm 209 (rad / s) for 1 min. Following decanting of the light brown supernatant, the precipitate was redispersed in 4 mL of toluene. 500 μL of OLAM and 250 μL of tri-*n*-octylphosphine (TOP) were added to afford improved colloidal stability to the nanoribbons during storage in solution.

A similar route was applied to synthesize μm-scale colloidal 2D SnS square nanosheets. 0.0038 g (0.118 mmol) of sulfur was dissolved in 10 mL of OLAM then added to a 25 mL reaction flask that was equivalently outfitted. To this, 20.2 μL (0.175 mmol) of $SnCl_4$ was added all at once using a micropipette and the flask was sealed with a septum. While stirring vigorously at room temperature, the reaction was evacuated. After waiting several min for the resulting bubbling to subside, the solution was heated to 120 °C (393 K) and held there for 20 minutes under vacuum. Next, the reaction was switched to an argon blanket and 0.7 mL (3.34 mmol) of hexamethyldisilazane was injected through the septum with a syringe. The temperature was raised to 195 °C (468 K) at ~ 10 ° / min and then to 210 °C (483 K) at ~ 3 ° / min, resulting in a silvery-black solution, and the temperature was maintained for 5 min before quenching the reaction with cold water. To separate the nanosheets, 30 mL of ethanol antisolvent was added to the solution before centrifuging at 5000 rpm (524 rad / s) for 1 min and decanting the resulting light-yellow supernatant. The precipitate was redispersed in toluene and washed by centrifugation twice more under the same conditions. Finally, the SnS square nanosheets were dispersed in 2 mL of toluene before 500 μL of OLAM and 250 μL of TOP surface stabilizers were added to assist with dispersability during solution storage.

Device fabrication. First, an aliquot of the nanoribbon and square nanosheet stock solutions were each washed of excess OLAM and TOP stabilizer by centrifugation at 13000 rpm (1361 rad / s) for 1 min and then redispersed in neat toluene. A drop of dilute, centrifugally washed colloidal

2D SnS was then cast on a heavily-doped p-type Si substrate with ≈ 300 nm of thermally grown SiO_2 and prefabricated gold alignment marks. The p++Si/SiO_2 served as the global back gate and gate dielectric, respectively, of the device. To remove the remaining surface organics, the sample was annealed in a tube furnace (Lindburg/Blue M, Thermo Scientific) under flowing 5 % H_2 forming gas at 400 ºC for 1 h. Next, isolated nanoribbons and square nanosheets were selected for contact fabrication using optical microscopy, and their positions relative to the alignment marks noted. After spin coating a resist of poly(methyl methacrylate) (PMMA) 495 A4 followed by PMMA 950 A4, contacts were patterned onto individual crystals using an electron beam lithography system (Raith Elphy Quantum). After writing the patterns, the substrate was dipped in 1 % hydrofluoric acid for 30 s to remove native oxide and then Cr/Au (5 nm/75 nm) metal contacts were deposited using an e-beam evaporator (Denton Vacuum Infinity 22). Resist liftoff was achieved through immersion in acetone overnight. Channel dimensions were recorded using optical microscopy. Finally, the sample was again annealed under forming gas at 350 °C (623 K) for 15 min to achieve ohmic contact between the semiconductor and metal.

Characterization. Transmission electron microscope (TEM) images were collected using a Phillips EM-400 operating at an accelerating voltage of 120 kV. Samples were prepared by casting one drop of dilute dispersed sample in toluene onto a 300-mesh Formvar and carbon-coated copper grid (Ted Pella, Inc.). High-resolution TEM (HRTEM) images, selected area electron diffraction (SAED) patterns, high-angle annular dark field scanning TEM (HAADF-STEM) images, and energy-dispersive X-ray (EDX) spectra were obtained using a FEI Titan 80-300 TEM operating at an accelerating voltage of 300 kV and equipped with an EDAX r-TEM EDX spectrometer. TIA software (FEI) was used for EDX data processing, with the Sn L-shell and S K-shell transitions, which do not appreciably overlap, chosen for quantitative analysis. Lattice spacings were

determined from the fast Fourier transform (FFT) of HRTEM images using Gatan Digital Micrograph software. Particle counting analysis used a minimum of 200 individual particles and size was determined using the ImageJ program (http://rsbweb.nih.gov/ij/). Scanning electron microscope (SEM) images and SEM-EDX elemental maps of washed samples drop-cast on Si/SiO_2 were obtained using a Zeiss Ultra 60 field emission SEM operating at 2 kV – 10 kV with a secondary electron detector and Oxford X-Max EDX detector. Optical microscopy images were collected using a Nikon L200 compound optical microscope. Atomic force microscope (AFM) analysis was conducted using an Asylum Research Cypher AFM in tapping mode.

Powder X-ray diffraction (XRD) patterns of washed samples drop-cast on a zero-background plate were collected with a Rigaku SmartLab X-ray diffractometer in the Bragg-Brentano geometry using Cu Kα radiation. Simulated powder XRD and electron diffraction patterns were made using the CrystalMaker software suite. X-ray photoelectron spectroscopy (XPS) measurements were performed in a Kratos Axis Ultra X-ray photoelectron spectrometer with a monochromatic Al Kα excitation source operating at 15 kV and 10 mA. The pass energy used was 160 eV for survey scans and 20 eV for detailed scans. XPS samples were prepared by drop-casting concentrated sample onto a gold-coated Si wafer and CasaXPS software was used for data analysis. Fourier transform infrared (FTIR) spectra were obtained from 100 co-added transmission scans at Brewster's angle using a Thermo Scientific Nicolet 8700 FTIR spectrometer equipped with a deuterated triglycine sulfate potassium bromide (DTGS KBr) detector at 4 cm^{-1} resolution. Samples were prepared by drop-casting onto one side of double-sided, moderately-doped, polished Si(111) wafer. FTIR absorbance spectra were generated by referencing to measurements conducted on the bare Si substrate. Raman spectra were collected using a 514 nm excitation line from an Ar^{+} laser (Coherent Innova Sabre) and collecting in a 180° backscattering geometry

through a triple-grating Raman spectrometer coupled to a CCD detector (Horiba T64000). The typical integration time was 300 s and samples were prepared by drop-casting on gold-coated Si.

Electrical measurements of individual fabricated devices were conducted in the dark at room temperature using a probe station (Cascade Microtech 11000) connected to a semiconductor parameter analyzer (Agilent 4156C). Output and transfer characteristics were obtained between two contacts while varying the applied back gate potential. Four-point measurements were taken for the nanoribbons by measuring the voltage between the inner two probes of the linear four-terminal structure and for the square nanosheets using the van der Pauw method.[89] Time-resolved terahertz spectroscopy (TRTS) measurements were carried out on washed colloidal 2D SnS samples prepared by casting a single drop of dispersed material onto a fused quartz substrate (GM Associates) without annealing. The thickness of each deposited sample was measured with a Bruker Dektak XT contact profilometer. The TRTS apparatus is based on an amplified femtosecond Ti:sapphire laser system (Coherent Mira seed and Legend regenerative amplifier) with 1 kHz repetition rate that has been described previously in detail.[41] Briefly, the 800 nm amplified pulse train is split into 3 arms which allow for photoexcitation, THz probe generation (0.3 THz to 2.0 THz) in a 1 mm thick ZnTe crystal, and gated, electro-optic detection of the THz probe in a 0.5 mm thick ZnTe crystal. The resulting gate pulse polarization is analyzed by a $\lambda/4$ wave plate and Wollaston prism, and then collected by a pair of balanced silicon photodetectors using lock-in amplification (Stanford Research Systems, SR830). Measurements were made in transmission configuration within a chamber purged with dry air to avoid absorption of the terahertz probe by atmospheric water. Terahertz time-domain spectroscopy (THz-TDS) was also carried out using the same apparatus with the excitation beam blocked. All measurements are the average of 10 sweeps of the pump or probe delay. A Perkin Elmer Lambda 950 UV-vis-NIR

spectrometer equipped with an integrating sphere was used to determine the transmission, reflection, and absorption of the TRTS samples.

ASSOCIATED CONTENT

Supporting Information. Further characterization of SnS 2D colloidal nanocrystals and the devices fabricated thereof, including additional TEM and SEM images, HAADF-STEM images, optical microscopy images, EDX spectra, AFM images, SEM-EDX elemental maps, FTIR spectra, XPS spectra, Raman spectra, and TRTS waveform spectra. This material is available free of charge at http://pubs.acs.org.

Disclaimer. The authors declare no competing financial interest. Certain commercial equipment or materials are identified in this paper to adequately specify the experimental procedures. In no case does the identification imply recommendation or endorsement by NIST, nor does it imply that the materials or equipment identified are necessarily the best available for the purpose.

ACKNOWLEDGMENT

We would like to acknowledge the NIST Director's Fellow Postdoctoral Research Associateship program (A.J.B.), the NIST/National Research Council Postdoctoral Research Associateship program (B.G.A.), and NIST-STRS for funding. Fabrication and some characterization was conducted at the NIST Center for Nanoscale Science and Technology. We are especially grateful to Steven Hudson for the kind use of his TEM. We also thank Kerry Siebein, Alline Myers, Albert Davydov, Jeffery Fagan, Christina Hacker, June Lau, and Emily Bittle for their assistance with

characterization and helpful discussions. A.J.B. gratefully acknowledges emeritus NIST fellow Herbert Bennett.

REFERENCES

1. Jariwala, D.; Sangwan, V. K.; Lauhon, L. J.; Marks, T. J.; Hersam, M. C. Emerging Device Applications for Semiconducting Two-Dimensional Transition Metal Dichalcogenides. *ACS Nano* **2014**, *8*, 1102-1120.

2. Novoselov, K. S.; Mishchenko, A.; Carvalho, A.; Castro Neto, A. H. 2D Materials and van der Waals Heterostructures. *Science* **2016**, *353*.

3. Gao, M.; Li, L.; Song, Y. Inkjet Printing Wearable Electronic Devices. *J. Mater. Chem. C* **2017**, *5*, 2971-2993.

4. Li, S.-L.; Tsukagoshi, K.; Orgiu, E.; Samori, P. Charge Transport and Mobility Engineering in Two-Dimensional Transition Metal Chalcogenide Semiconductors. *Chem. Soc. Rev.* **2016**, *45*, 118-151.

5. Chhowalla, M.; Jena, D.; Zhang, H. Two-Dimensional Semiconductors for Transistors. *Nat. Rev. Mater.* **2016**, *1*, 16052.

6. Novoselov, K. S.; Jiang, D.; Schedin, F.; Booth, T. J.; Khotkevich, V. V.; Morozov, S. V.; Geim, A. K. Two-Dimensional Atomic Crystals. *Proc. Natl. Acad. Sci. U.S.A.* **2005**, *102*, 10451-10453.

7. Bhimanapati, G. R.; Lin, Z.; Meunier, V.; Jung, Y.; Cha, J.; Das, S.; Xiao, D.; Son, Y.; Strano, M. S.; Cooper, V. R.; Liang, L.; Louie, S. G.; Ringe, E.; Zhou, W.; Kim, S. S.; Naik, R. R.; Sumpter, B. G.; Terrones, H.; Xia, F.; Wang, Y.; *et al*. Recent Advances in Two-Dimensional Materials beyond Graphene. *ACS Nano* **2015**, *9*, 11509-11539.

8. Ryder, C. R.; Wood, J. D.; Wells, S. A.; Hersam, M. C. Chemically Tailoring Semiconducting Two-Dimensional Transition Metal Dichalcogenides and Black Phosphorus. *ACS Nano* **2016**, *10*, 3900-3917.

9. Schwierz, F.; Pezoldt, J.; Granzner, R. Two-Dimensional Materials and their Prospects in Transistor Electronics. *Nanoscale* **2015**, *7*, 8261-8283.

10. Kelly, A. G.; Hallam, T.; Backes, C.; Harvey, A.; Esmaeily, A. S.; Godwin, I.; Coelho, J.; Nicolosi, V.; Lauth, J.; Kulkarni, A.; Kinge, S.; Siebbeles, L. D. A.; Duesberg, G. S.; Coleman, J. N. All-Printed Thin-Film Transistors from Networks of Liquid-Exfoliated Nanosheets. *Science* **2017**, *356*, 69-73.

11. McManus, D.; Vranic, S.; Withers, F.; Sanchez-Romaguera, V.; Macucci, M.; Yang, H.; Sorrentino, R.; Parvez, K.; Son, S.-K.; Iannaccone, G.; Kostarelos, K.; Fiori, G.; Casiraghi, C. Water-Based and Biocompatible 2D Crystal Inks for All-Inkjet-Printed Heterostructures. *Nat. Nanotech.* **2017**, *12*, 343-350.

12. Zhu, J.; Hersam, M. C. Assembly and Electronic Applications of Colloidal Nanomaterials. *Adv. Mater.* **2017**, *29*, 1603895.

13. Kang, J.; Sangwan, V. K.; Wood, J. D.; Hersam, M. C. Solution-Based Processing of Monodisperse Two-Dimensional Nanomaterials. *Acc. Chem. Res.* **2017**, *50*, 943-951.

14. Bonaccorso, F.; Bartolotta, A.; Coleman, J. N.; Backes, C. 2D-Crystal-Based Functional Inks. *Adv. Mater.* **2016**, *28*, 6136-6166.

15. Lv, R.; Robinson, J. A.; Schaak, R. E.; Sun, D.; Sun, Y.; Mallouk, T. E.; Terrones, M. Transition Metal Dichalcogenides and Beyond: Synthesis, Properties, and Applications of Single- and Few-Layer Nanosheets. *Acc. Chem. Res.* **2015**, *48*, 56-64.

16. Nasilowski, M.; Mahler, B.; Lhuillier, E.; Ithurria, S.; Dubertret, B. Two-Dimensional Colloidal Nanocrystals. *Chem. Rev.* **2016**, *116*, 10934-10982.

17. Biacchi, A. J.; Vaughn, D. D.; Schaak, R. E. Synthesis and Crystallographic Analysis of Shape-Controlled SnS Nanocrystal Photocatalysts: Evidence for a Pseudotetragonal Structural Modification. *J. Am. Chem. Soc.* **2013**, *135*, 11634-11644.

18. Vaughn II, D. D.; In, S.-I.; Schaak, R. E. A Precursor-Limited Nanoparticle Coalescence Pathway for Tuning the Thickness of Laterally-Uniform Colloidal Nanosheets: The Case of SnSe. *ACS Nano* **2011**, *5*, 8852-8860.

19. Schliehe, C.; Juarez, B. H.; Pelletier, M.; Jander, S.; Greshnykh, D.; Nagel, M.; Meyer, A.; Foerster, S.; Kornowski, A.; Klinke, C.; Weller, H. Ultrathin PbS Sheets by Two-Dimensional Oriented Attachment. *Science* **2010**, *329*, 550-553.

20. Vaughn II, D. D.; Patel, R. J.; Hickner, M. A.; Schaak, R. E. Single-Crystal Colloidal Nanosheets of GeS and GeSe. *J. Am. Chem. Soc.* **2010**, *132*, 15170-15172.

21. Xue, D.-J.; Tan, J.; Hu, J.-S.; Hu, W.; Guo, Y.-G.; Wan, L.-J. Anisotropic Photoresponse Properties of Single Micrometer-Sized GeSe Nanosheet. *Adv. Mater.* **2012**, *24*, 4528-4533.

22. Buck, M. R.; Biacchi, A. J.; Popczun, E. J.; Schaak, R. E. Polymer-Assisted Synthesis of Colloidal Germanium Telluride Nano-Octahedra, Nanospheres, and Nanosheets. *Chem. Mater.* **2013**, *25*, 2163-2171.

23. Xiong, X.; Zhang, Q.; Zhou, X.; Jin, B.; Li, H.; Zhai, T. One-Step Synthesis of p-Type GaSe Nanoribbons and their Excellent Performance in Photodetectors and Phototransistors. *J. Mater. Chem. C* **2016**, *4*, 7817-7823.

24. Lauth, J.; Gorris, F. E. S.; Samadi Khoshkhoo, M.; Chassé, T.; Friedrich, W.; Lebedeva, V.; Meyer, A.; Klinke, C.; Kornowski, A.; Scheele, M.; Weller, H. Solution-Processed Two-Dimensional Ultrathin InSe Nanosheets. *Chem. Mater.* **2016**, *28*, 1728-1736.

25. Ithurria, S.; Tessier, M. D.; Mahler, B.; Lobo, R. P. S. M.; Dubertret, B.; Efros, A. L. Colloidal Nanoplatelets with Two-Dimensional Electronic Structure. *Nat. Mater.* **2011**, *10*, 936-941.

26. Xie, J.; Zhang, J.; Li, S.; Grote, F.; Zhang, X.; Zhang, H.; Wang, R.; Lei, Y.; Pan, B.; Xie, Y. Controllable Disorder Engineering in Oxygen-Incorporated MoS_2 Ultrathin Nanosheets for Efficient Hydrogen Evolution. *J. Am. Chem. Soc.* **2013**, *135*, 17881-17888.

27. Sun, D.; Feng, S.; Terrones, M.; Schaak, R. E. Formation and Interlayer Decoupling of Colloidal $MoSe_2$ Nanoflowers. *Chem. Mater.* **2015**, *27*, 3167-3175.

28. Sun, Y.; Wang, Y.; Sun, D.; Carvalho, B. R.; Read, C. G.; Lee, C.-h.; Lin, Z.; Fujisawa, K.; Robinson, J. A.; Crespi, V. H.; Terrones, M.; Schaak, R. E. Low-Temperature Solution Synthesis of Few-Layer 1T′-$MoTe_2$ Nanostructures Exhibiting Lattice Compression. *Angew. Chem. Int. Ed.* **2016**, *55*, 2830-2834.

29. Tan, Z.; Wu, Y.; Hong, H.; Yin, J.; Zhang, J.; Lin, L.; Wang, M.; Sun, X.; Sun, L.; Huang, Y.; Liu, K.; Liu, Z.; Peng, H. Two-Dimensional $(C_4H_9NH_3)_2PbBr_4$ Perovskite Crystals for High-Performance Photodetector. *J. Am. Chem. Soc.* **2016**, *138*, 16612-16615.

30. Skelton, J. M.; Burton, L. A.; Oba, F.; Walsh, A. Chemical and Lattice Stability of the Tin Sulfides. *J. Phys. Chem. C* **2017**, *121*, 6446-6454.

31. Xin, C.; Zheng, J.; Su, Y.; Li, S.; Zhang, B.; Feng, Y.; Pan, F. Few-Layer Tin Sulfide: A New Black-Phosphorus-Analogue 2D Material with a Sizeable Band Gap, Odd–Even Quantum Confinement Effect, and High Carrier Mobility. *J. Phys. Chem. C* **2016**, *120*, 22663-22669.

32. Antunez, P. D.; Buckley, J. J.; Brutchey, R. L. Tin and Germanium Monochalcogenide IV-VI Semiconductor Nanocrystals for Use in Solar Cells. *Nanoscale* **2011**, *3*, 2399-2411.

33. Burton, L. A.; Colombara, D.; Abellon, R. D.; Grozema, F. C.; Peter, L. M.; Savenije, T. J.; Dennler, G.; Walsh, A. Synthesis, Characterization, and Electronic Structure of Single-Crystal SnS, Sn_2S_3, and SnS_2. *Chem. Mater.* **2013**, *25*, 4908-4916.

34. Koteeswara Reddy, N.; Devika, M.; Gopal, E. S. R. Review on Tin(II) Sulfide (SnS) Material: Synthesis, Properties, and Applications. *Crit. Rev. Solid State Mater. Sci.* **2015**, *40*, 359-398.

35. Banai, R. E.; Horn, M. W.; Brownson, J. R. S. A Review of Tin(II) Monosulfide and its Potential as a Photovoltaic Absorber. *Sol. Energy Mater. Sol. Cells* **2016**, *150*, 112-129.

36. Albers, W.; Haas, C.; van der Maesen, F. The Preparation and the Electrical and Optical Properties of SnS Crystals. *J. Phys. Chem. Solids* **1960**, *15*, 306-310.

37. Sinsermsuksakul, P.; Heo, J.; Noh, W.; Hock, A. S.; Gordon, R. G. Atomic Layer Deposition of Tin Monosulfide Thin Films. *Adv. Energy Mater.* **2011**, *1*, 1116-1125.

38. de Kergommeaux, A.; Lopez-Haro, M.; Pouget, S.; Zuo, J.-M.; Lebrun, C.; Chandezon, F.; Aldakov, D.; Reiss, P. Synthesis, Internal Structure, and Formation Mechanism of Monodisperse Tin Sulfide Nanoplatelets. *J. Am. Chem. Soc.* **2015**, *137*, 9943-9952.

39. Deng, Z.; Han, D.; Liu, Y. Colloidal Synthesis of Metastable Zincblende IV-VI SnS Nanocrystals with Tunable Sizes. *Nanoscale* **2011**, *3*, 4346-4351.

40. Patra, B. K.; Sarkar, S.; Guria, A. K.; Pradhan, N. Monodisperse SnS Nanocrystals: In Just 5 Seconds. *J. Phys. Chem. Lett.* **2013**, *4*, 3929-3934.

41. Alberding, B. G.; Biacchi, A. J.; Hight Walker, A. R.; Heilweil, E. J. Charge Carrier Dynamics and Mobility Determined by Time-Resolved Terahertz Spectroscopy on Films of Nano-to-Micrometer-Sized Colloidal Tin(II) Monosulfide. *J. Phys. Chem. C* **2016**, *120*, 15395-15406.

42. Yang, H.; Kim, C.-E.; Giri, A.; Soon, A.; Jeong, U. Synthesis of Surfactant-Free SnS Nanoplates in an Aqueous Solution. *RSC Adv.* **2015**, *5*, 94796-94801.

43. Koktysh, D. S.; McBride, J. R.; Rosenthal, S. J. Synthesis of SnS Nanocrystals by the Solvothermal Decomposition of a Single Source Precursor. *Nanoscale Res. Lett.* **2007**, *2*, 144.

44. Brent, J. R.; Lewis, D. J.; Lorenz, T.; Lewis, E. A.; Savjani, N.; Haigh, S. J.; Seifert, G.; Derby, B.; O'Brien, P. Tin(II) Sulfide (SnS) Nanosheets by Liquid-Phase Exfoliation of Herzenbergite: IV–VI Main Group Two-Dimensional Atomic Crystals. *J. Am. Chem. Soc.* **2015**, *137*, 12689-12696.

45. Liu, X.; Li, Y.; Zhou, B.; Wang, X.; Cartwright, A. N.; Swihart, M. T. Shape-Controlled Synthesis of SnE (E = S, Se) Semiconductor Nanocrystals for Optoelectronics. *Chem. Mater.* **2014**, *26*, 3515-3521.

46. Greyson, E. C.; Barton, J. E.; Odom, T. W. Tetrahedral Zinc Blende Tin Sulfide Nano- and Microcrystals. *Small* **2006**, *2*, 368-371.

47. Gao, W.; Wu, C.; Cao, M.; Huang, J.; Wang, L.; Shen, Y. Thickness Tunable SnS Nanosheets for Photoelectrochemical Water Splitting. *J. Alloys Compd.* **2016**, *688*, 668-674.

48. Zhu, H.; Yang, D.; Ji, Y.; Zhang, H.; Shen, X. Two-Dimensional SnS Nanosheets Fabricated by a Novel Hydrothermal Method. *J. Mater. Sci.* **2005**, *40*, 591-595.

49. Herron, S. M.; Tanskanen, J. T.; Roelofs, K. E.; Bent, S. F. Highly Textured Tin(II) Sulfide Thin Films Formed from Sheetlike Nanocrystal Inks. *Chem. Mater.* **2014**, *26*, 7106-7113.

50. Chao, J.; Wang, Z.; Xu, X.; Xiang, Q.; Song, W.; Chen, G.; Hu, J.; Chen, D. Tin Sulfide Nanoribbons as High Performance Photoelectrochemical Cells, Flexible Photodetectors and Visible-Light-Driven Photocatalysts. *RSC Adv.* **2013**, *3*, 2746-2753.

51. Zhang, Y.; Lu, J.; Shen, S.; Xu, H.; Wang, Q. Ultralarge Single Crystal SnS Rectangular Nanosheets. *Chem. Commun.* **2011**, *47*, 5226-5228.

52. Deng, Z.; Cao, D.; He, J.; Lin, S.; Lindsay, S. M.; Liu, Y. Solution Synthesis of Ultrathin Single-Crystalline SnS Nanoribbons for Photodetectors *via* Phase Transition and Surface Processing. *ACS Nano* **2012**, *6*, 6197-6207.

53. Kagan, C. R.; Murray, C. B. Charge Transport in Strongly Coupled Quantum Dot Solids. *Nat. Nanotech.* **2015**, *10*, 1013-1026.

54. Kholmicheva, N.; Moroz, P.; Eckard, H.; Jensen, G.; Zamkov, M. Energy Transfer in Quantum Dot Solids. *ACS Energy Lett.* **2017**, *2*, 154-160.

55. Oh, S. J.; Berry, N. E.; Choi, J.-H.; Gaulding, E. A.; Lin, H.; Paik, T.; Diroll, B. T.; Muramoto, S.; Murray, C. B.; Kagan, C. R. Designing High-Performance PbS and PbSe Nanocrystal Electronic Devices through Stepwise, Post-Synthesis, Colloidal Atomic Layer Deposition. *Nano Lett.* **2014**, *14*, 1559-1566.

56. Kagan, C. R.; Lifshitz, E.; Sargent, E. H.; Talapin, D. V. Building Devices from Colloidal Quantum Dots. *Science* **2016**, *353*, 885.

57. Whitham, K.; Yang, J.; Savitzky, B. H.; Kourkoutis, L. F.; Wise, F.; Hanrath, T. Charge Transport and Localization in Atomically Coherent Quantum Dot Solids. *Nat. Mater.* **2016**, *15*, 557-563.

58. Dogan, S.; Bielewicz, T.; Cai, Y.; Klinke, C. Field–Effect Transistors Made of Individual Colloidal PbS Nanosheets. *Appl. Phys. Lett.* **2012**, *101*, 073102.

59. Oh, S. J.; Kim, D. K.; Kagan, C. R. Remote Doping and Schottky Barrier Formation in Strongly Quantum Confined Single PbSe Nanowire Field-Effect Transistors. *ACS Nano* **2012**, *6*, 4328-4334.

60. Ramasamy, P.; Kwak, D.; Lim, D.-H.; Ra, H.-S.; Lee, J.-S. Solution Synthesis of GeS and GeSe Nanosheets for High-Sensitivity Photodetectors. *J. Mater. Chem. C* **2016**, *4*, 479-485.

61. Tan, C.-S.; Chen, H.-S.; Chiu, C.-Y.; Wu, S.-C.; Chen, L.-J.; Huang, M. H. Facet-Dependent Electrical Conductivity Properties of PbS Nanocrystals. *Chem. Mater.* **2016**, *28*, 1574-1580.

62. Guglietta, G. W.; Diroll, B. T.; Gaulding, E. A.; Fordham, J. L.; Li, S.; Murray, C. B.; Baxter, J. B. Lifetime, Mobility, and Diffusion of Photoexcited Carriers in Ligand-Exchanged Lead Selenide Nanocrystal Films Measured by Time-Resolved Terahertz Spectroscopy. *ACS Nano* **2015**, *9*, 1820-1828.

63. Lauth, J.; Kulkarni, A.; Spoor, F. C. M.; Renaud, N.; Grozema, F. C.; Houtepen, A. J.; Schins, J. M.; Kinge, S.; Siebbeles, L. D. A. Photogeneration and Mobility of Charge Carriers in Atomically Thin Colloidal InSe Nanosheets Probed by Ultrafast Terahertz Spectroscopy. *J. Phys. Chem. Lett.* **2016**, *7*, 4191-4196.

64. Alberding, B. G.; Robert Thurber, W.; Heilweil, E. J. Direct Comparison of Time-Resolved Terahertz Spectroscopy and Hall Van der Pauw Methods for Measurement of Carrier Conductivity and Mobility in Bulk Semiconductors. *J. Opt. Soc. Am. B* **2017**, *34*, 1392-1406.

65. van Embden, J.; Chesman, A. S. R.; Jasieniak, J. J. The Heat-Up Synthesis of Colloidal Nanocrystals. *Chem. Mater.* **2015**, *27*, 2246-2285.

66. Biacchi, A. J.; Schaak, R. E. The Solvent Matters: Kinetic *versus* Thermodynamic Shape Control in the Polyol Synthesis of Rhodium Nanoparticles. *ACS Nano* **2011**, *5*, 8089-8099.

67. Lu, J.; Nan, C.; Li, L.; Peng, Q.; Li, Y. Flexible SnS Nanobelts: Facile Synthesis, Formation Mechanism and Application in Li-ion Batteries. *Nano Res.* **2013**, *6*, 55-64.

68. Biacchi, A. J.; Schaak, R. E. Ligand-Induced Fate of Embryonic Species in the Shape-Controlled Synthesis of Rhodium Nanoparticles. *ACS Nano* **2015**, *9*, 1707-1720.

69. Yin, X.; Shi, J.; Niu, X.; Huang, H.; Wang, X. Wedding Cake Growth Mechanism in One-Dimensional and Two-Dimensional Nanostructure Evolution. *Nano Lett.* **2015**, *15*, 7766-7772.

70. Devika, M.; Reddy, N. K.; Patolsky, F.; Gunasekhar, K. R. Ohmic Contacts to SnS films: Selection and Estimation of Thermal Stability. *J. Appl. Phys.* **2008**, *104*, 124503.

71. Smyth, C. M.; Addou, R.; McDonnell, S.; Hinkle, C. L.; Wallace, R. M. Contact Metal–MoS2 Interfacial Reactions and Potential Implications on MoS_2-Based Device Performance. *J. Phys. Chem. C* **2016**, *120*, 14719-14729.

72. Chandrasekhar, H. R.; Humphreys, R. G.; Zwick, U.; Cardona, M. Infrared and Raman spectra of the IV-VI compounds SnS and SnSe. *Phys. Rev. B* **1977**, *15*, 2177-2183.

73. Le, S. T.; Jannaty, P.; Zaslavsky, A.; Dayeh, S. A.; Picraux, S. T. Growth, Electrical Rectification, and Gate Control in Axial *in situ* Doped p-n Junction Germanium Nanowires. *Appl. Phys. Lett.* **2010**, *96*, 262102.

74. Zhang, Z.; Yang, J.; Zhang, K.; Chen, S.; Mei, F.; Shen, G. Anisotropic Photoresponse of Layered 2D SnS-based Near Infrared Photodetectors. *J. Mater. Chem. C* **2017**, *5*, 11288-11293.

75. Vidal, J.; Lany, S.; d'Avezac, M.; Zunger, A.; Zakutayev, A.; Francis, J.; Tate, J. Band-structure, Optical Properties, and Defect Physics of the Photovoltaic Semiconductor SnS. *Appl. Phys. Lett.* **2012**, *100*, 032104.

76. Tian, Z.; Guo, C.; Zhao, M.; Li, R.; Xue, J. Two-Dimensional SnS: A Phosphorene Analogue with Strong In-Plane Electronic Anisotropy. *ACS Nano* **2017**, *11*, 2219-2226.

77. Sucharitakul, S.; Rajesh Kumar, U.; Sankar, R.; Chou, F.-C.; Chen, Y.-T.; Wang, C.; He, C.; He, R.; Gao, X. P. A. Screening Limited Switching Performance of Multilayer 2D Semiconductor FETs: the Case for SnS. *Nanoscale* **2016**, *8*, 19050-19057.

78. Ahn, J.-H.; Lee, M.-J.; Heo, H.; Sung, J. H.; Kim, K.; Hwang, H.; Jo, M.-H. Deterministic Two-Dimensional Polymorphism Growth of Hexagonal n-Type SnS_2 and Orthorhombic p-Type SnS Crystals. *Nano Lett.* **2015**, *15*, 3703-3708.

79. Yanagi, H.; Iguchi, Y.; Sugiyama, T.; Kamiya, T.; Hosono, H. n-Type Conduction in SnS by Anion Substitution with Cl. *Appl. Phys. Express* **2016**, *9*, 051201.

80. Xu, Y.; Yuan, J.; Zhang, K.; Hou, Y.; Sun, Q.; Yao, Y.; Li, S.; Bao, Q.; Zhang, H.; Zhang, Y. Field-Induced n-Doping of Black Phosphorus for CMOS Compatible 2D Logic Electronics with High Electron Mobility. *Adv. Funct. Mater.* **2017**, *27*, 1702211.

81. Mahjouri-Samani, M.; Liang, L.; Oyedele, A.; Kim, Y.-S.; Tian, M.; Cross, N.; Wang, K.; Lin, M.-W.; Boulesbaa, A.; Rouleau, C. M.; Puretzky, A. A.; Xiao, K.; Yoon, M.; Eres, G.; Duscher, G.; Sumpter, B. G.; Geohegan, D. B. Tailoring Vacancies Far Beyond Intrinsic Levels Changes the Carrier Type and Optical Response in Monolayer $MoSe_{2-x}$ Crystals. *Nano Lett.* **2016**, *16*, 5213-5220.

82. Oh, S. J.; Berry, N. E.; Choi, J.-H.; Gaulding, E. A.; Paik, T.; Hong, S.-H.; Murray, C. B.; Kagan, C. R. Stoichiometric Control of Lead Chalcogenide Nanocrystal Solids to Enhance Their Electronic and Optoelectronic Device Performance. *ACS Nano* **2013**, *7*, 2413-2421.

83. Tanuševski, A.; Poelman, D. Optical and Photoconductive Properties of SnS Thin Films Prepared by Electron Beam Evaporation. *Sol. Energy Mater. Sol. Cells* **2003**, *80*, 297-303.

84. Koteeswara Reddy, N.; Ramakrishna Reddy, K. T. Electrical Properties of Spray Pyrolytic Tin Sulfide Films. *Solid·State Electron.* **2005**, *49*, 902-906.

85. Lei, S.; Wang, X.; Li, B.; Kang, J.; He, Y.; George, A.; Ge, L.; Gong, Y.; Dong, P.; Jin, Z.; Brunetto, G.; Chen, W.; Lin, Z.-T.; Baines, R.; Galvão, D. S.; Lou, J.; Barrera, E.; Banerjee, K.; Vajtai, R.; Ajayan, P. Surface Functionalization of Two-Dimensional Metal Chalcogenides by Lewis Acid–Base Chemistry. *Nat. Nano* **2016**, *11*, 465-471.

86. Hajzus, J. R.; Biacchi, A. J.; Le, S. T.; Richter, C. A.; Hight Walker, A. R.; Porter, L. M. Contacts to Solution-Synthesized SnS Nanoribbons: Dependence of Barrier Height on Metal Work Function. *Nanoscale* **2018**, *10*, 319-327.

87. Guo, R.; Wang, X.; Kuang, Y.; Huang, B. First-Principles Study of Anisotropic Thermoelectric Transport Properties of IV-VI Semiconductor Compounds SnSe and SnS. *Phys. Rev. B* **2015**, *92*, 115202.

88. Chang, H.-Y.; Zhu, W.; Akinwande, D. On the Mobility and Contact Resistance Evaluation for Transistors Based on MoS_2 or Two-Dimensional Semiconducting Atomic Crystals. *Appl. Phys. Lett.* **2014**, *104*, 113504.

89. van der Pauw, L. J. A Method for Measuring Specific Resistivity and Hall Effect of Discs of Arbitrary Shapes. *Phillips Res. Repts.* **1958**, *13*, 1-9.

90. Hegmann, F. A.; Ostroverkhova, O.; Cooke, D. G., *Photophysics of Molecular Materials*. Wiley-VCH: Weinheim, 2006.

91. Jaramillo, R.; Sher, M.-J.; Ofori-Okai, B. K.; Steinmann, V.; Yang, C.; Hartman, K.; Nelson, K. A.; Lindenberg, A. M.; Gordon, R. G.; Buonassisi, T. Transient Terahertz Photoconductivity Measurements of Minority-carrier Lifetime in Tin Sulfide Thin Films: Advanced Metrology for an Early Stage Photovoltaic Material. *J. Appl. Phys.* **2016**, *119*, 035101.

92. Strait, J. H.; Nene, P.; Rana, F. High Intrinsic Mobility and Ultrafast Carrier Dynamics in Multilayer Metal-Dichalcogenide MoS2. *Phys. Rev. B* **2014**, *90*, 245402.

93. Steinmann, V.; Brandt, R. E.; Chakraborty, R.; Jaramillo, R.; Young, M.; Ofori-Okai, B. K.; Yang, C.; Polizzotti, A.; Nelson, K. A.; Gordon, R. G.; Buonassisi, T. The Impact of Sodium Contamination in Tin Sulfide Thin-Film Solar Cells. *APL Mater.* **2016**, *4*, 026103.

94. Kröger, F. A.; Vink, H. J., Relations between the Concentrations of Imperfections in Crystalline Solids. In *Solid State Phys.*, Seitz, F.; Turnbull, D., Eds. Academic Press: 1956; Vol. 3, pp 307-435.

95. Polizzotti, A.; Faghaninia, A.; Poindexter, J. R.; Nienhaus, L.; Steinmann, V.; Hoye, R. L. Z.; Felten, A.; Deyine, A.; Mangan, N. M.; Correa-Baena, J. P.; Shin, S. S.; Jaffer, S.; Bawendi, M. G.; Lo, C.; Buonassisi, T. Improving the Carrier Lifetime of Tin Sulfide *via* Prediction and Mitigation of Harmful Point Defects. *J. Phys. Chem. Lett.* **2017**, *8*, 3661-3667.

Table of Contents Graphic

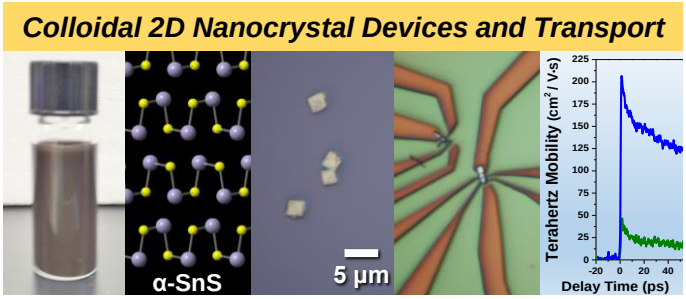
Colloidal 2D Nanocrystal Devices and Transport
α-SnS
5 μm
Terahertz Mobility (cm² / V·s)
Delay Time (ps)

SUPPORTING INFORMATION

Contact and Non-Contact Measurement of Electronic Transport in Individual 2D SnS Colloidal Semiconductor Nanocrystals

Adam J. Biacchi*,‡, Son T. Le‡, Brian G. Alberding§, Joseph A. Hagmann‡, Sujitra J. Pookpanratana‡, Edwin J. Heilweil‡, Curt A. Richter‡, and Angela R. Hight Walker*,‡

‡ *Nanoelectronics Group, Engineering Physics Division, National Institute of Standards and Technology (NIST), Gaithersburg, Maryland 20899, United States.*

§ *Remote Sensing Group, Sensor Science Division, National Institute of Standards and Technology (NIST), Gaithersburg, Maryland 20899, United States.*

*E-mail: adam.biacchi@nist.gov, angela.hightwalker@nist.gov

(a) View of armchair bonding

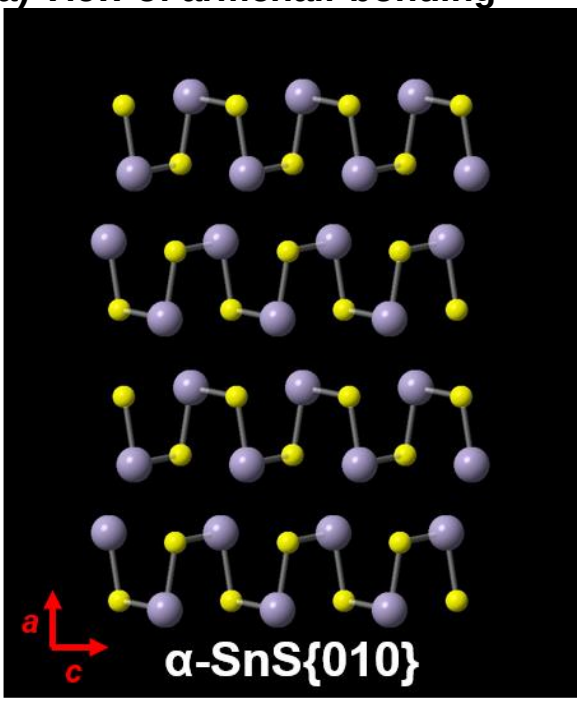

(b) View of zigzag bonding

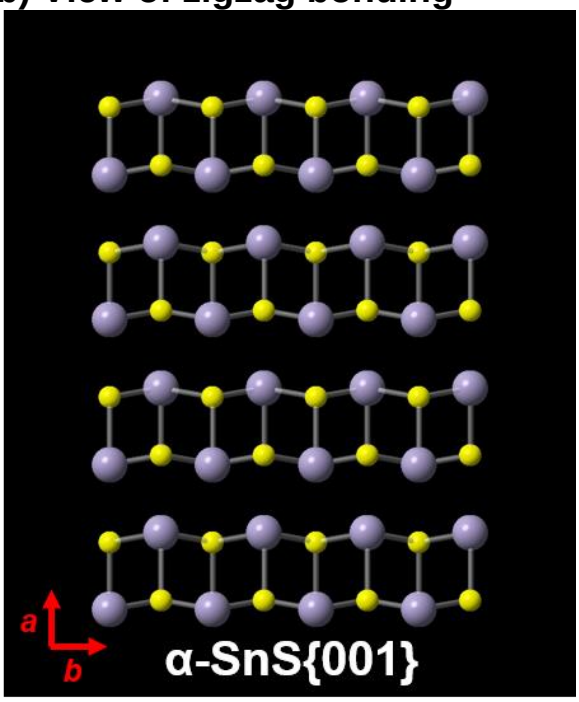

Figure S1. Crystal structure of orthorhombic α-SnS, also known as herzenbergite, (*Pnma*, *a* = 1.118 nm, *b* = 0.398 nm, *c* = 0.433 nm)[1] viewed from (a) the [010] zone axis and (b) the [001] zone axis displaying its layered nature and anisotropic interlayer bonding. Armchair bonding is found in the [001] direction and zigzag bonding is found in the [010] direction. (grey atoms = Sn^{2+}, yellow atoms = S^{2-})

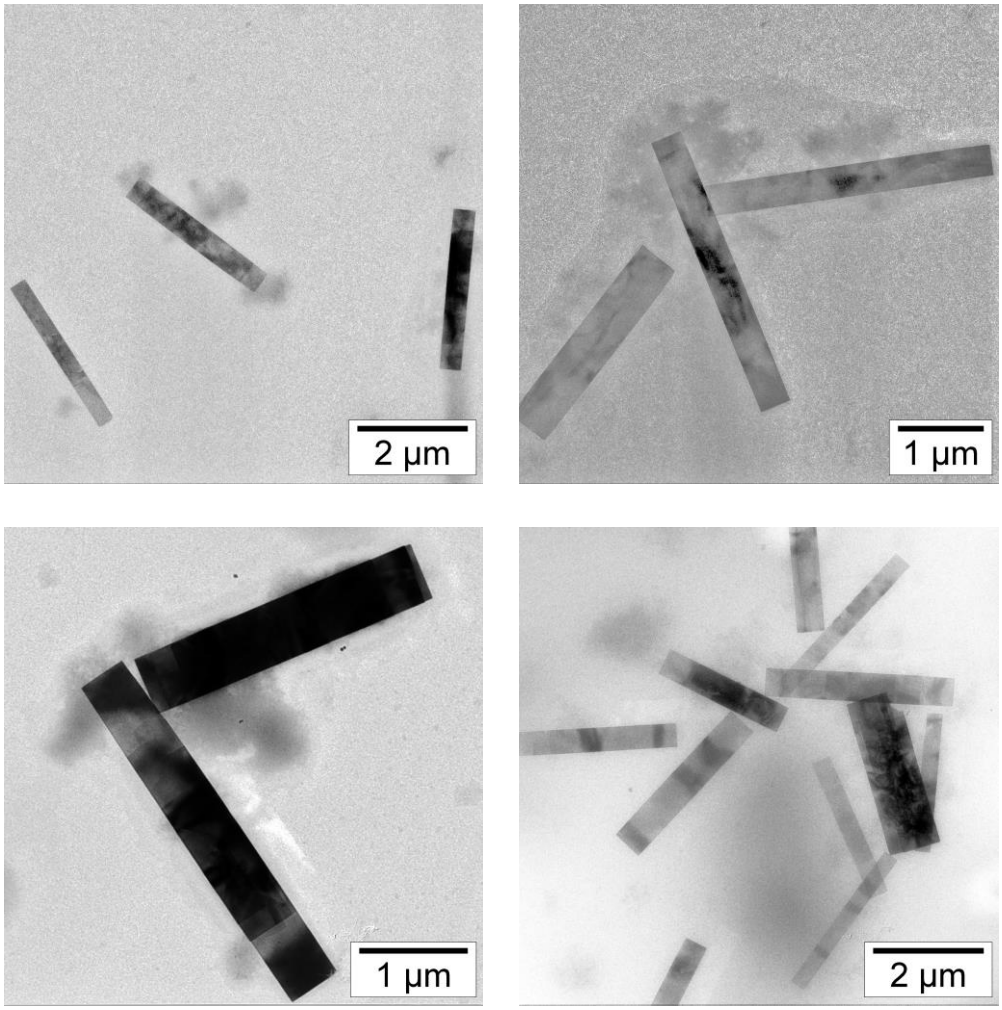

Figure S2. Additional TEM images of SnS nanoribbons.

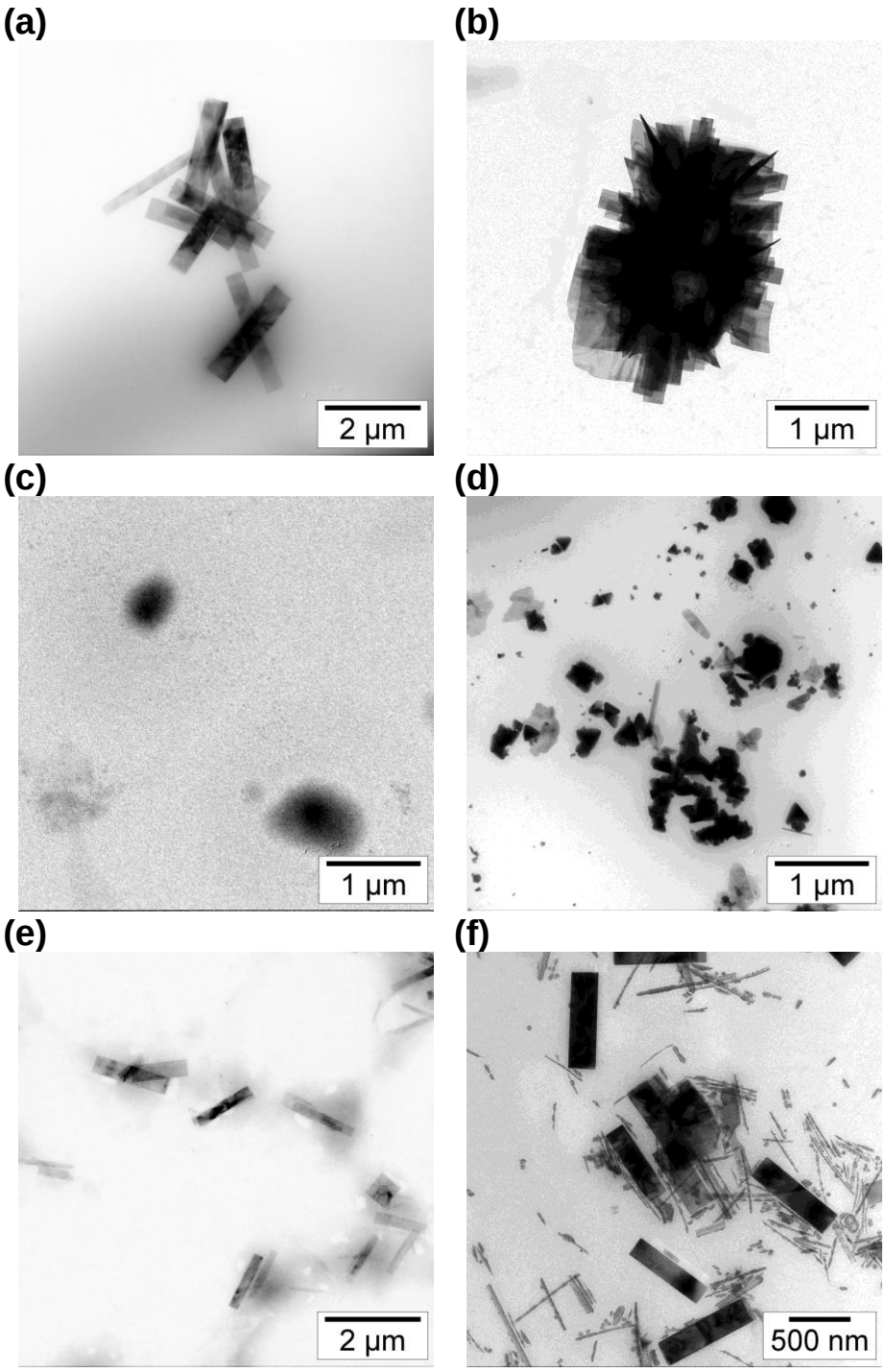

Figure S3. Variation of SnS nanoribbon synthetic conditions. (a) Shorter ribbons form at lower concentration of reagents (0.1 mmol $SnCl_2$ and 0.2 mmol sulfur) but (b) SnS flowers form if the concentration is too low (0.05 mmol $SnCl_2$ and 0.1 mmol sulfur). (c) Only precursor clusters result at 165 °C (438 K) instead of 180 °C (453 K) while (d) a mixture of products form if reagents are hot injected at 200 °C (473 K). (e) Using $SnBr_2$ yields shorter and less monodisperse ribbons, while (f) $Sn(acetate)_2$ produces a mixture of short ribbons and nanowires.

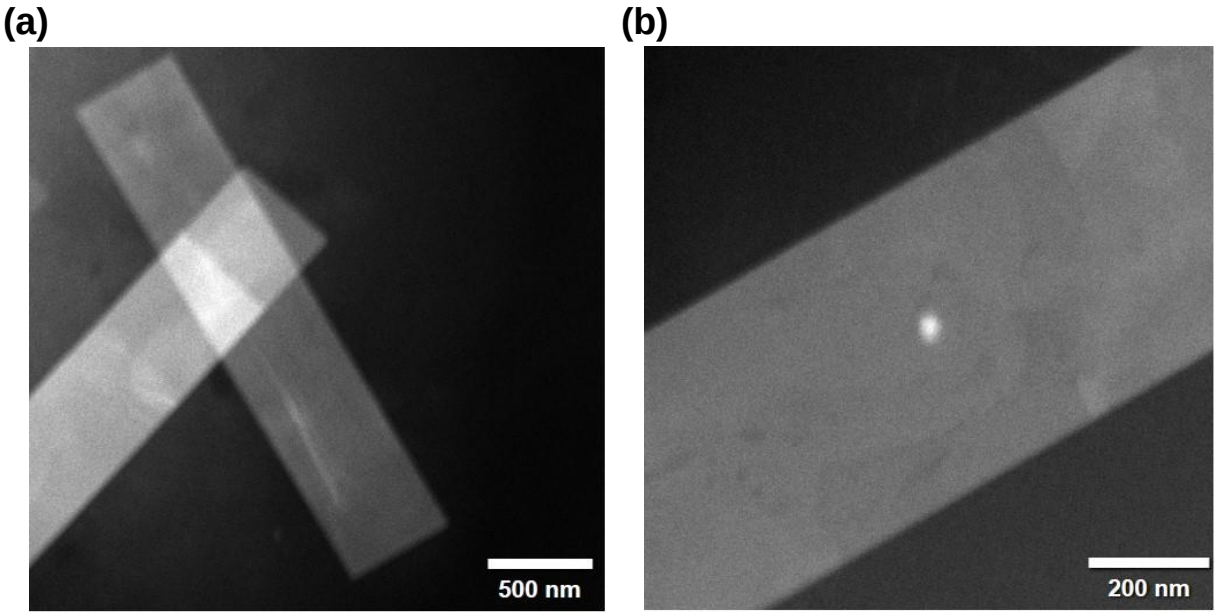

Figure S4. HAADF-STEM images of SnS nanoribbons. The white circle in the center of (b) is due to beam damage.

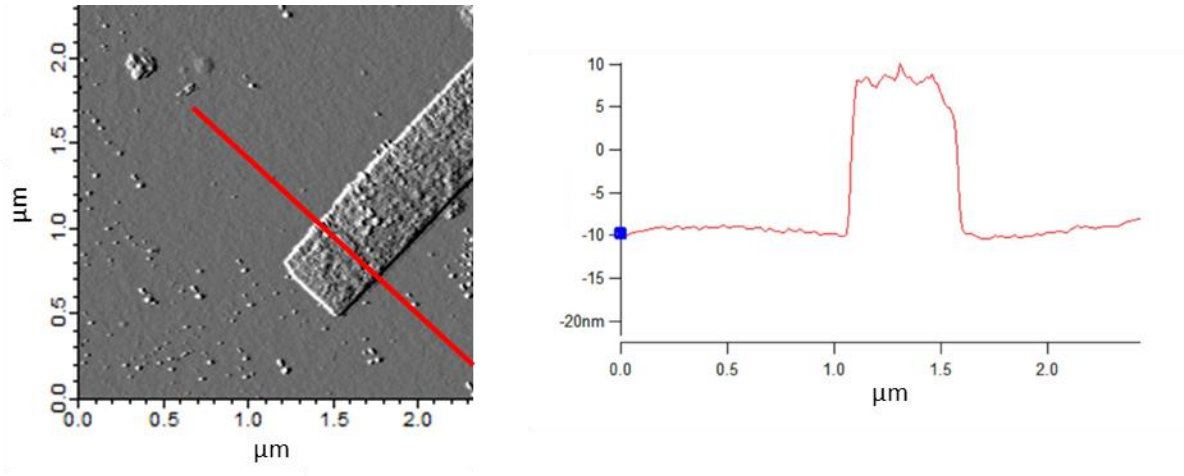

Figure S5. AFM characterization of SnS nanoribbons, indicating their thickness of approximately 17 - 20 nm.

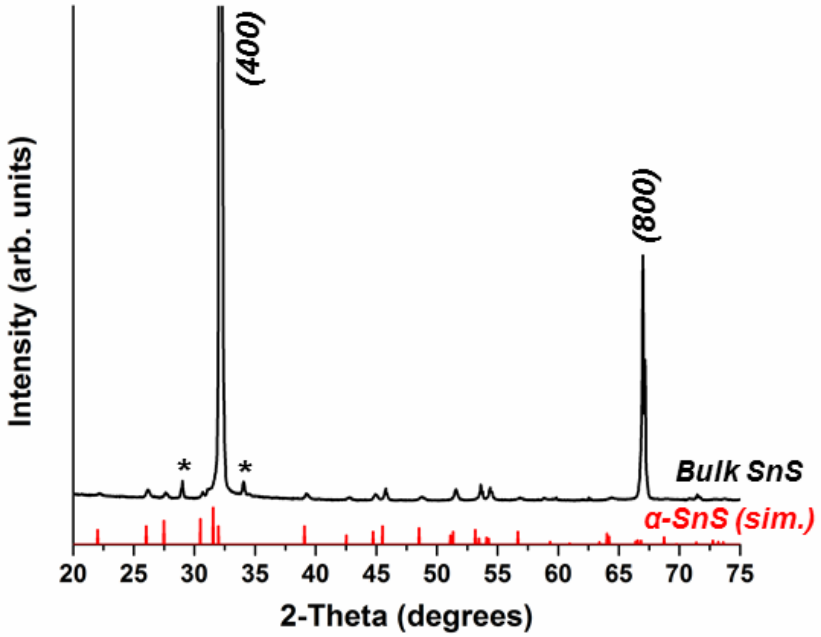

Figure S6. XRD pattern of commercial, bulk herzenbergite SnS (Sigma-Aldrich) compared to the simulated pattern of GeS-type α-SnS (JCPDS card number 73-1859) from Figures 1 and 2 (* = surface oxides).

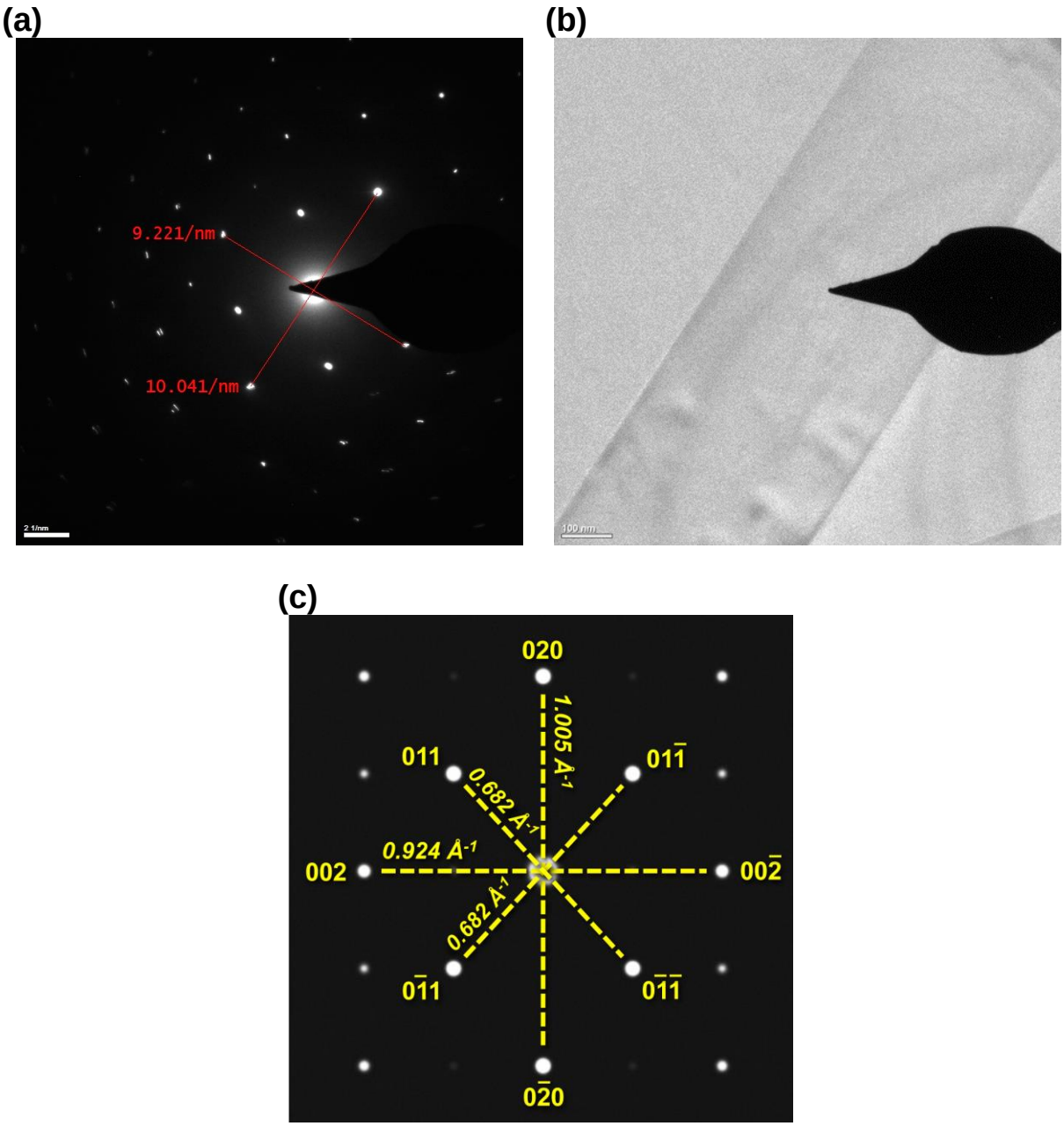

Figure S7. (a) SAED pattern collected from a single SnS nanoribbon and (b) a bright-field TEM image showing the orientation of the nanoribbon producing the diffraction pattern shown in (a). When compared to (c) the simulated electron diffraction pattern for orthorhombic α-SnS(100),[2] the reciprocal space distances between diffraction spots in (a) indicate that the length of the nanoribbon extends in the crystallographic <010> (zigzag) directions, while the width extends in the <001> (armchair) directions.

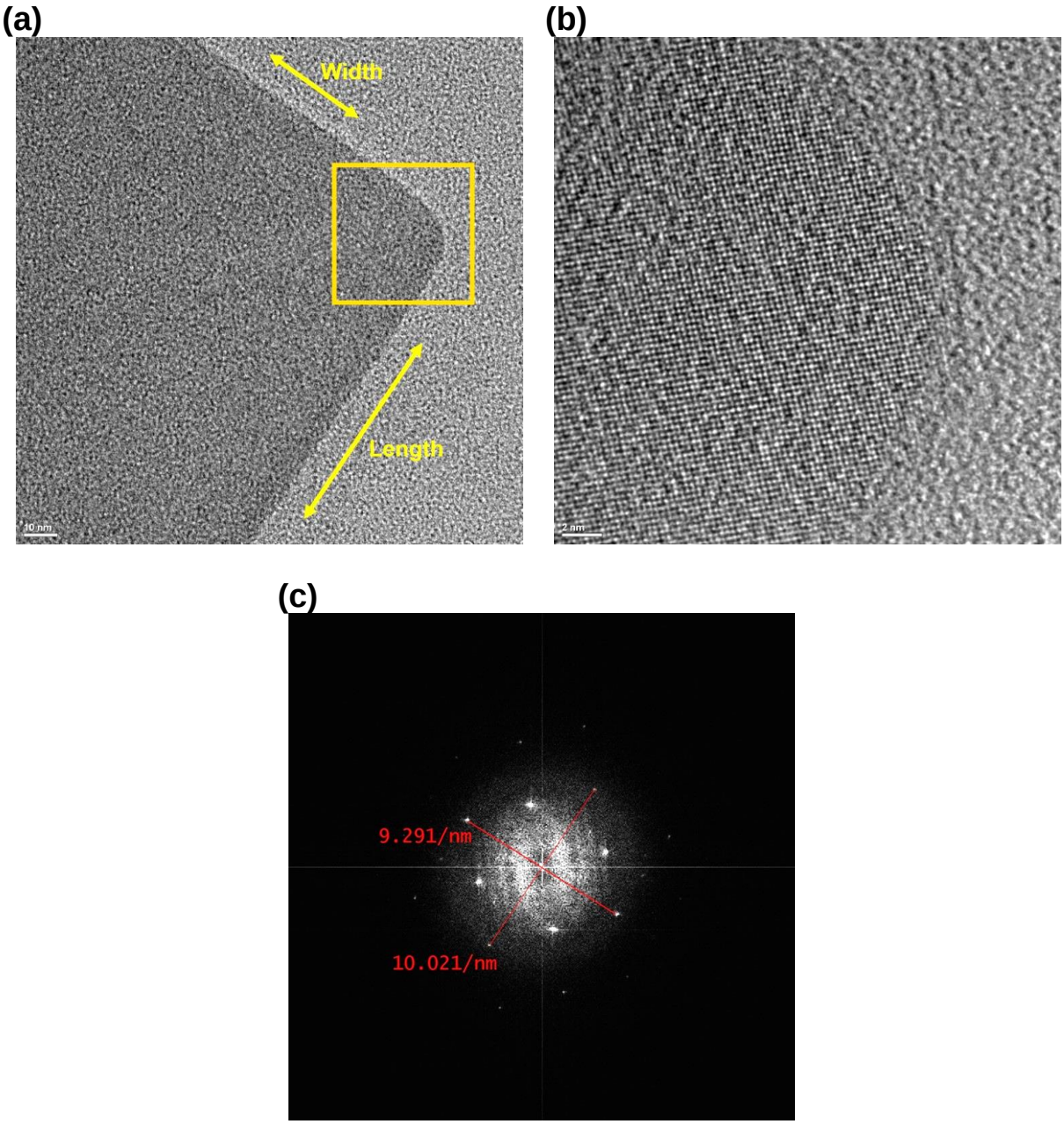

Figure S8. (a) TEM image of a µm-scale SnS nanoribbon and (b) HRTEM image of the highlighted region in (a). (c) The corresponding HRTEM FFT of (b) confirms that the length of the ribbon corresponds to the crystallographic SnS<010> directions (zigzag) and the width to SnS<001> (armchair) when compared to the simulated electron diffraction pattern displayed in Figure S7c.

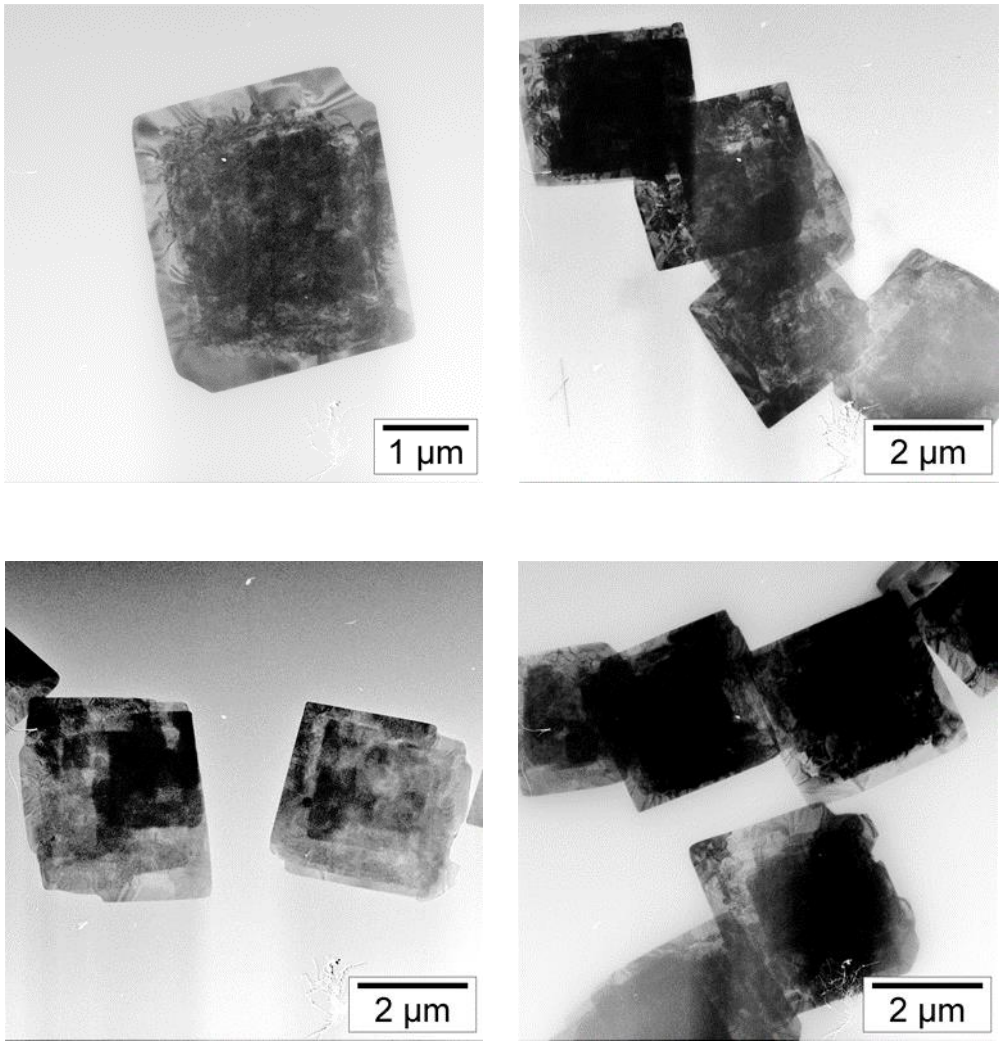

Figure S9. Additional TEM images of SnS square nanosheets.

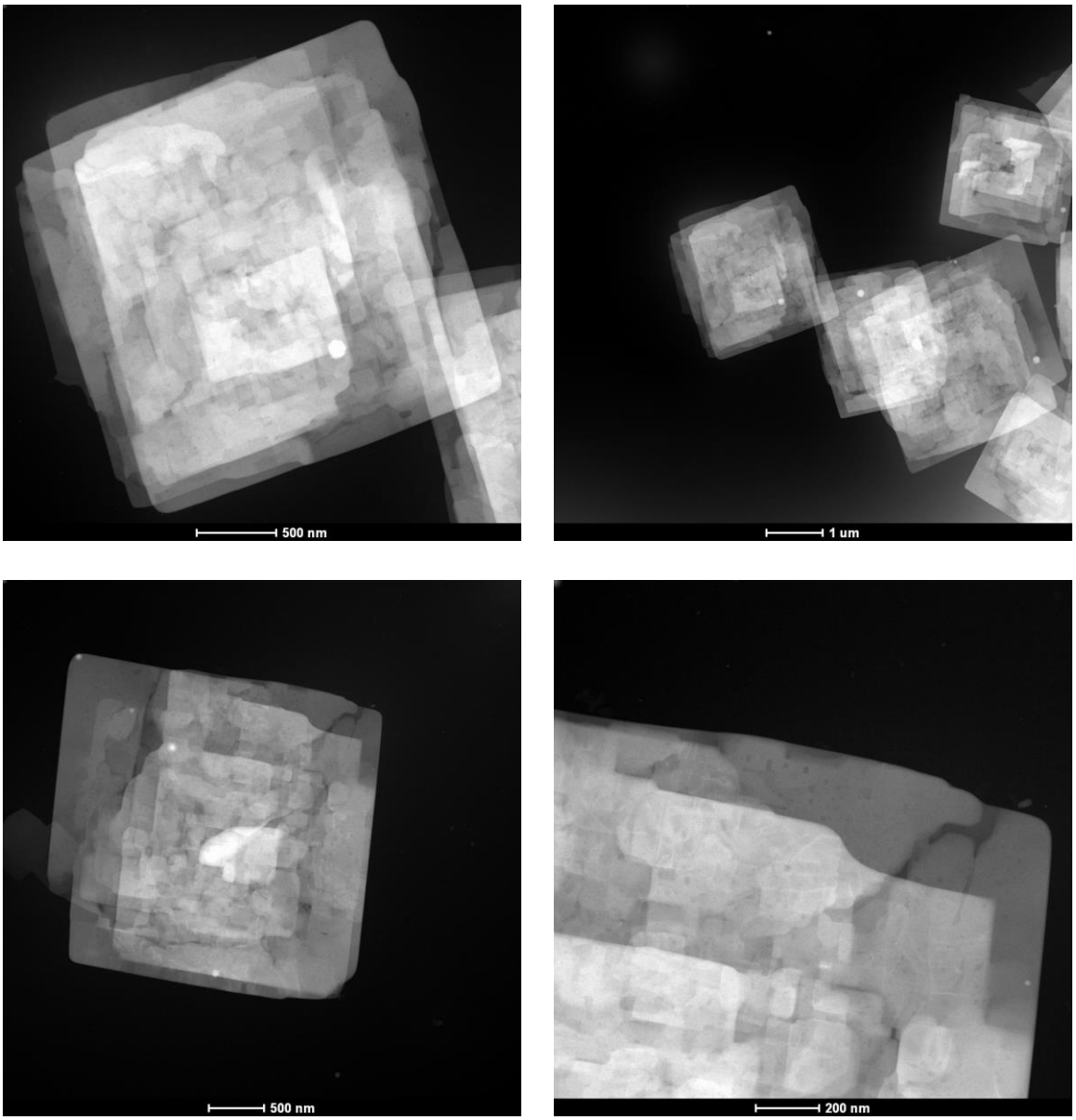

Figure S10. HAADF-STEM images of SnS square nanosheets.

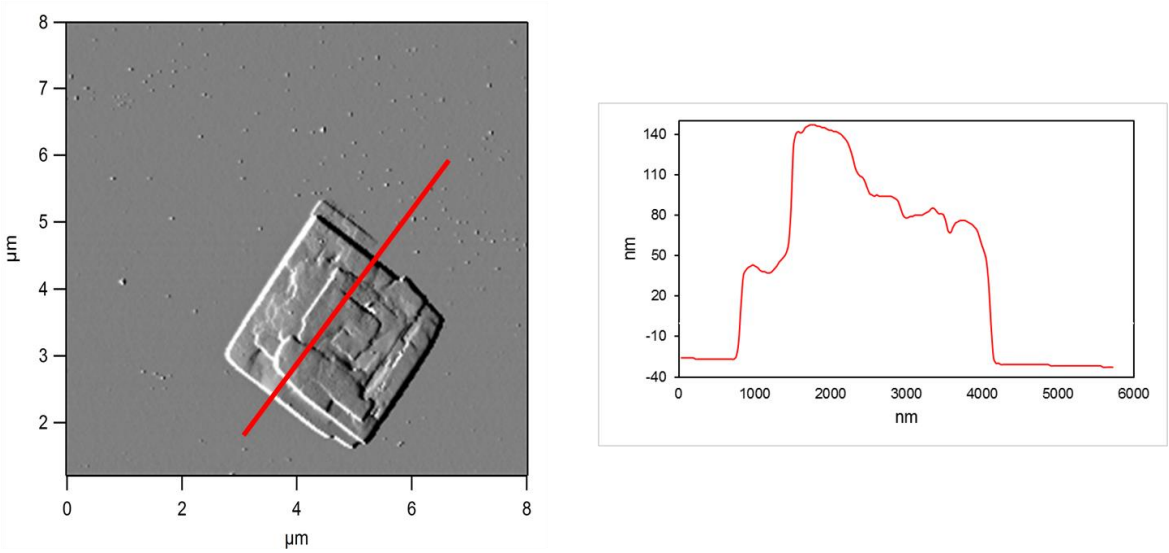

Figure S11. AFM characterization of an SnS square nanosheet, indicating its thickness varies from ≈75 nm to ≈160 nm across the various steps and plateaus of the nanostructure.

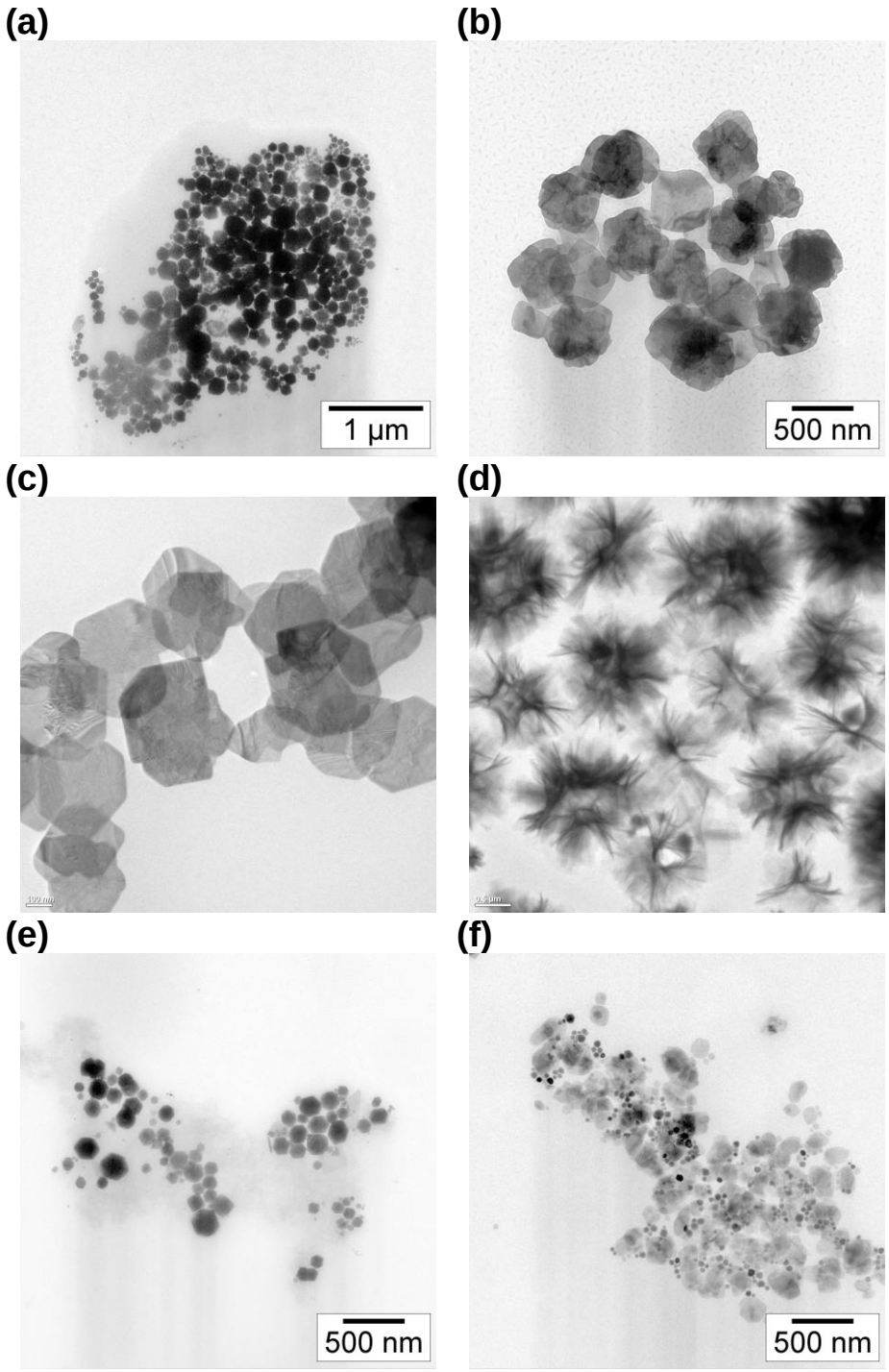

Figure S12. Variation of SnS square nanosheet synthetic conditions. (a) Only polyhedra are obtained without HMDS present, indicating it is essential to the formation of the nanosheets. However, (b) an excess of HMDS (1.25 mL) results in smaller irregular nanosheets, likely due to increased precursor reactivity and corresponding formation kinetics. (c) Small nanosheets form when the Sn:S ratio is increased to 2.5:1, while (d) an excess of sulfur (1:2.5 Sn:S) results in SnS nanoflowers. Replacing $SnCl_4$ with 0.175 mmol (e) $SnBr_4$ yields primarily mixed polyhedra and with (f) $Sn(acetate)_4$ produces a mixture of small rounded sheets and polyhedra.

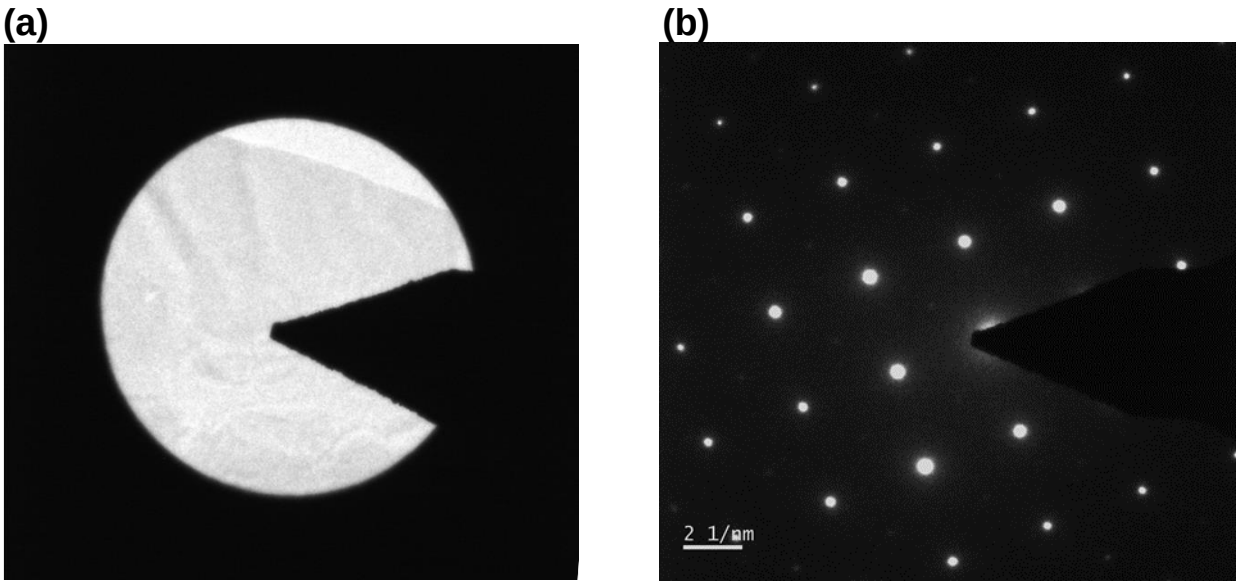

Figure S13. (a) Bright-field TEM image indicating the orientation of the SnS square nanosheet relative to (b) the SnS(100) SAED pattern collected from it, revealing that the edges of the nanosheet correspond to the <010> and <001> directions, while the corners correspond to <011> directions.

(a)

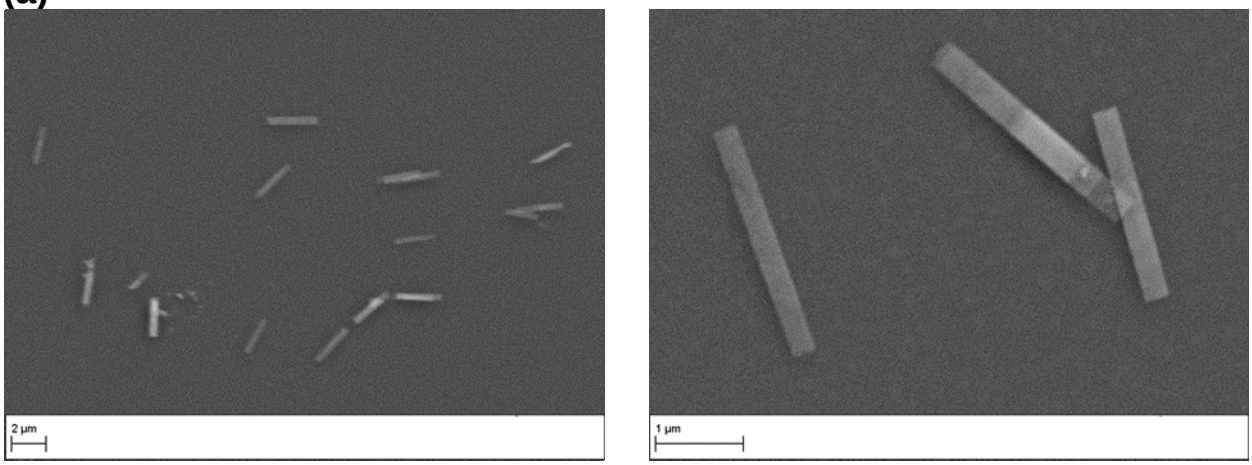

(b)

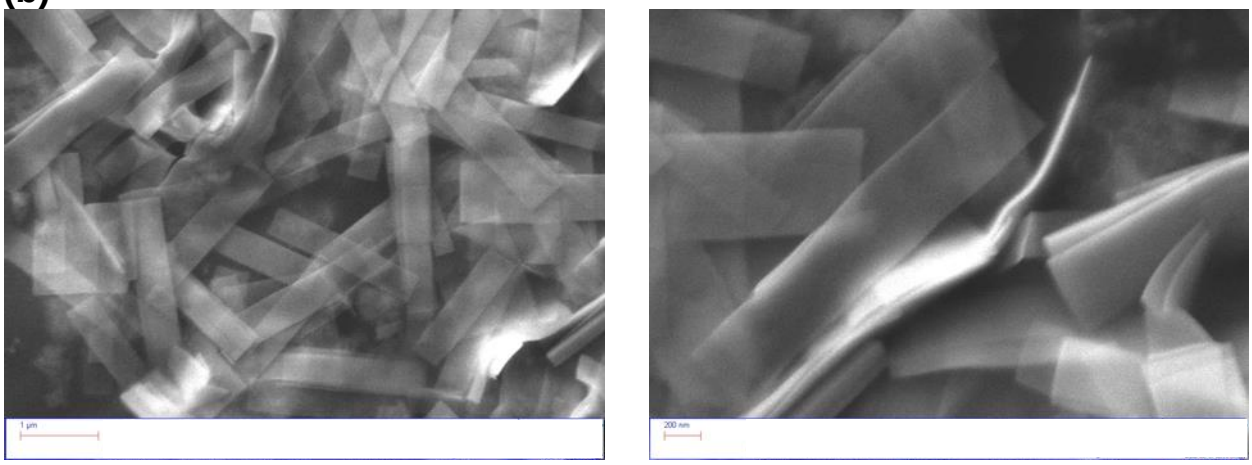

Figure S14. Additional SEM images of (a) dilute and (b) concentrated drop-cast 2D SnS nanoribbons.

(a)

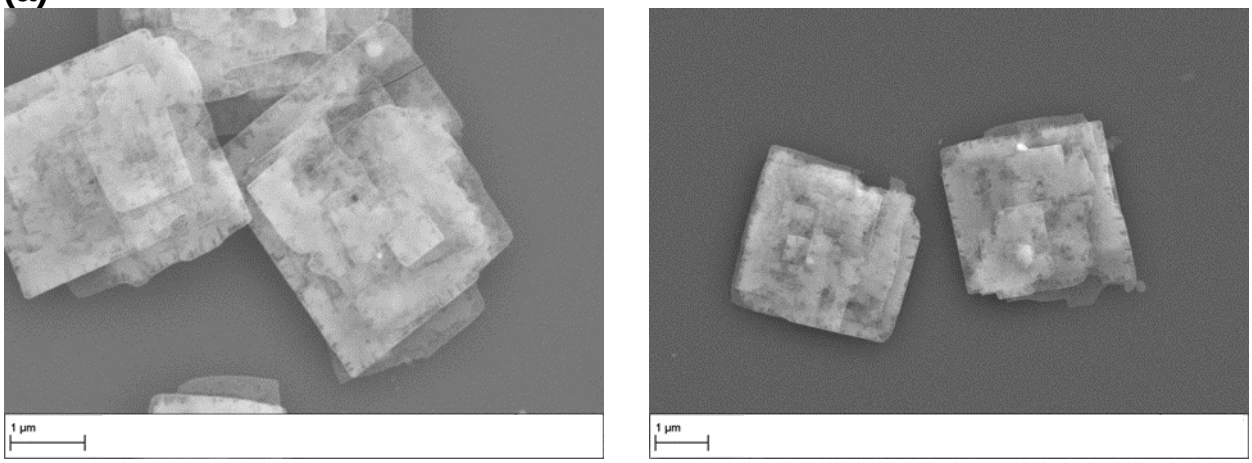

(b)

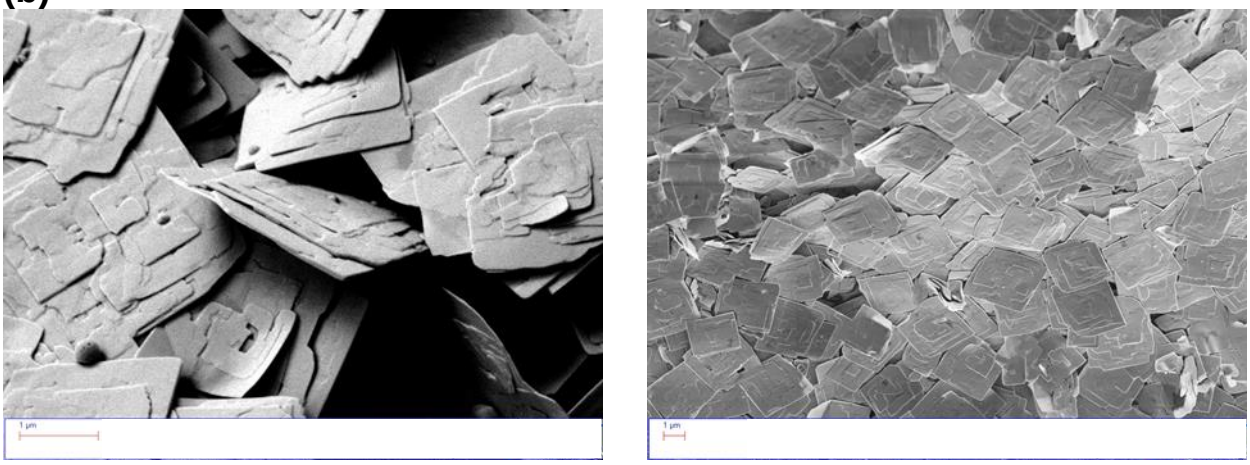

Figure S15. Additional SEM images of (a) dilute and (b) concentrated drop-cast 2D SnS square nanosheets.

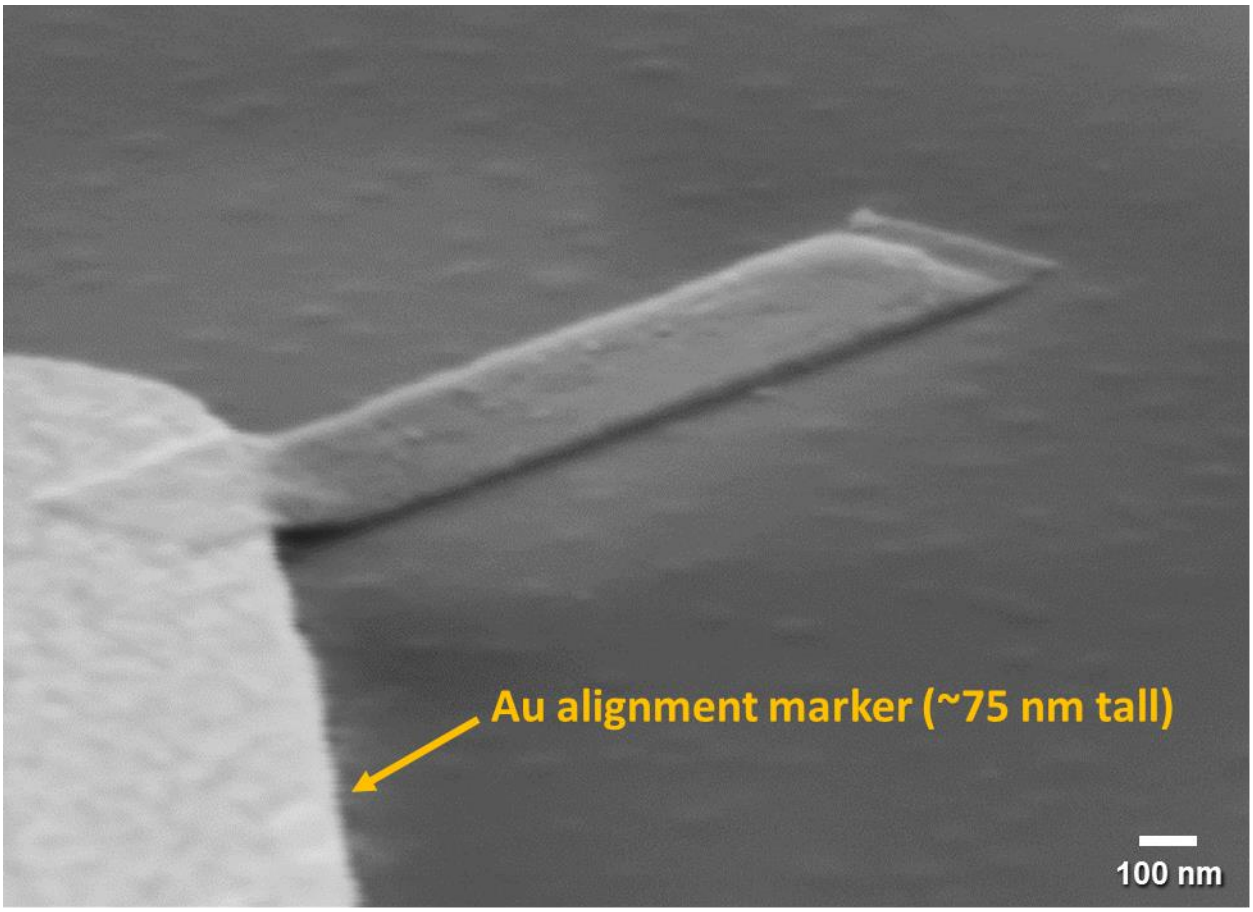

Figure S16. SEM image, taken at a tilt, of an SnS nanoribbon, displaying the elasticity of the nanostructure as it lays astride a ≈75 nm tall fiducial marker on the substrate.

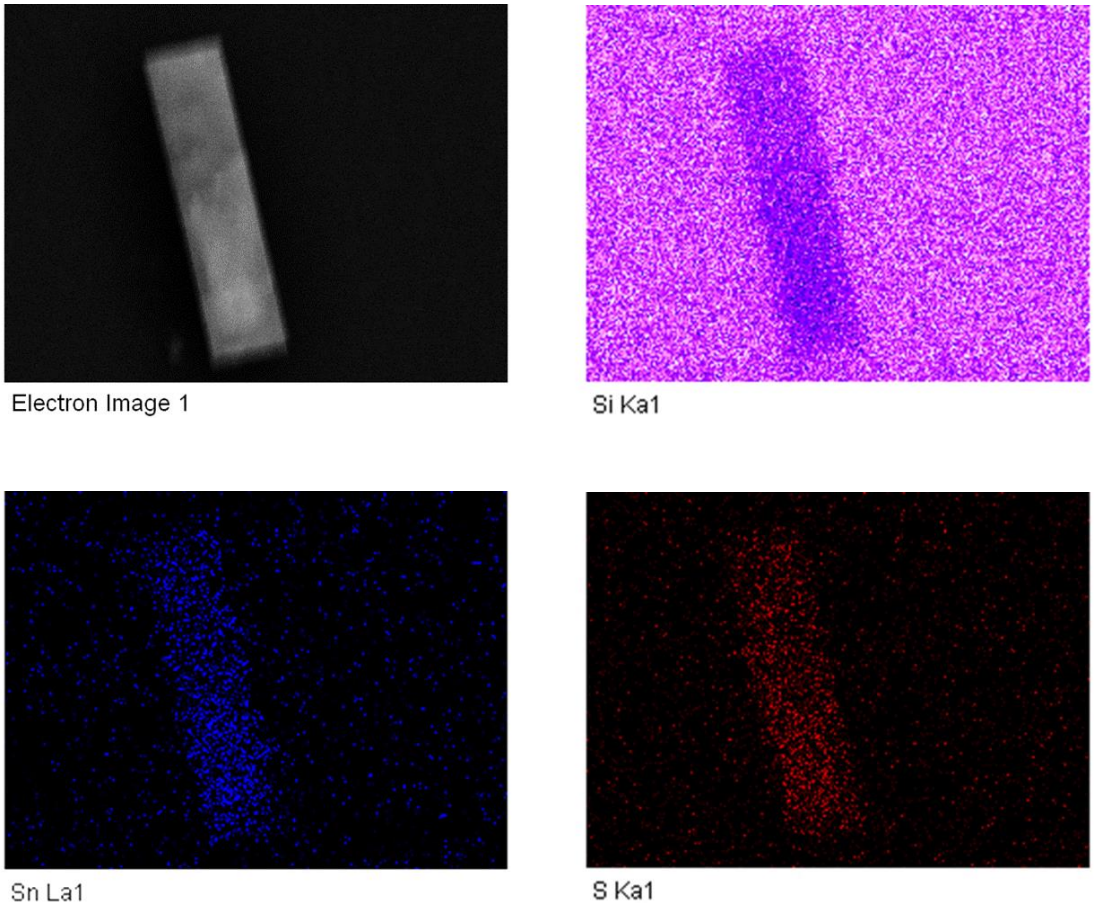

Figure S17. SEM-EDX elemental maps of an individual SnS nanoribbon deposited on an Si substrate, demonstrating a uniform distribution of Sn and S throughout the 2D nanostructure.

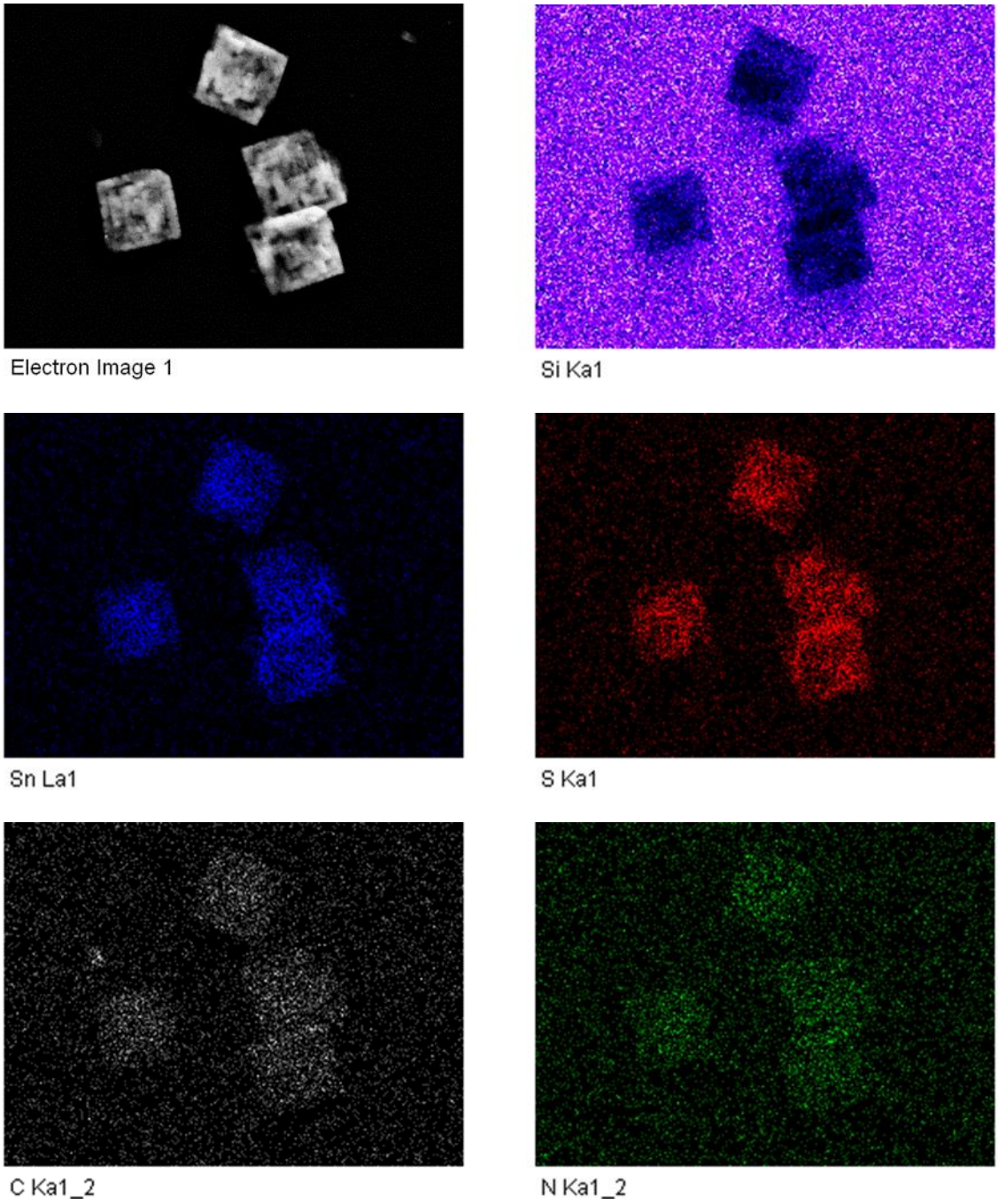

Figure S18. SEM-EDX elemental maps of several SnS square nanosheets deposited on Si, demonstrating a uniform distribution of Sn and S throughout the 2D materials. The presence of C and N detected on the nanocrystals indicates that, despite centrifugal washing, OLAM or other surfactants that provided colloidal stability are still adsorbed to the surface following deposition on the substrate.

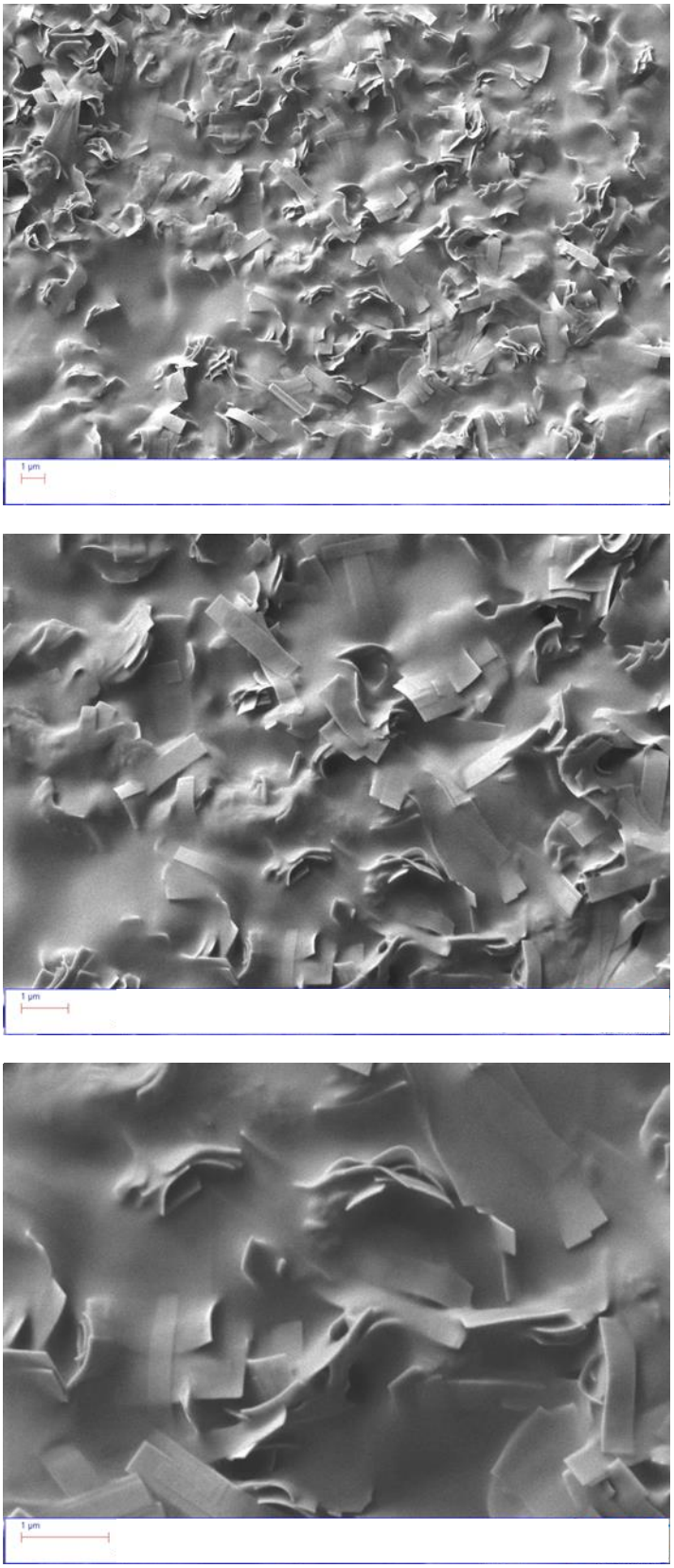

Figure S19. SEM images of a drop-cast SnS nanoribbons without centrifugal washing.

Additional Colloidal SnS FET Device Fabrication Details

We cast a single drop of dilute, centrifugally washed, dispersed nanocrystals in toluene onto a substrate of heavily doped p+Si covered with a 300 nm layer of grown SiO_2 dielectric and an array of photolithographically defined Au fiducial marks. Manipulating the drop concentration allowed for control of the semiconductor density on the substrate. Concentrated drops afford a compact film of SnS, whereas a dilute drop resulted in nanoribbons and square nanosheets distributed across a wide area, appropriate for characterizing or fabricating devices from individual 2D SnS nanocrystals. After drying in air, optical microscopy showed the 2D SnS nanocrystals deposited on the substrate in a random fashion within the circular drop's vicinity. The density of semiconductor nanocrystals on the periphery of the deposition area was unacceptably high for fabrication of single crystal devices due to the "coffee ring effect" (Figures S20a,b,d). However, throughout the interior we found regions of 2D SnS colloidal nanocrystals that had dried from solution with a free proximity of 10 μm or more surrounding them.

After recording the desired device positions relative to the alignment pattern, the substrate was annealed in a tube furnace under an atmosphere of 5 % forming gas at 400 °C (673 K) to remove oleylamine and other organic species from the surface of the 2D SnS. Despite the removal of most surfactant during our initial centrifugal wash, we found that residual molecules adsorbed to the 2D SnS prevented smooth application of our lithographic resist. Fourier-transform infrared (FTIR) spectroscopy confirmed that annealing effectively removed these ligands. As seen in Figure S21, the strong signal of the C-H stretching modes around 2800 cm^{-1} – 3000 cm^{-1}, characteristic of aliphatic hydrocarbons, was no longer present after this thermal treatment. Absorption due to a mixture of alkane, amine, and phosphine moieties located from ~1300 cm^{-1} to 1650 cm^{-1} were also likewise removed by this process. The crystallographic structure of the SnS nanocrystals was preserved during this process, as confirmed by Raman spectroscopy (see Figure S25).

After spin coating a poly(methyl methacrylate) (PMMA) resist, electron beam lithography was used to pattern device contacts on selected individual 2D SnS nanocrystals. Next, the developed area was cleaned and etched of native oxide using a brief hydrofluoric acid wash before proceeding with physical vapor deposition of metal electrodes using an electron-beam evaporator. A Cr adhesion layer (10 nm) was deposited first, followed by an Au noble metal capping layer (70 nm). Liftoff of the resist was achieved in acetone, and images of the resulting device arrays were collected using SEM and optical microscopy (Figures S22-S23).

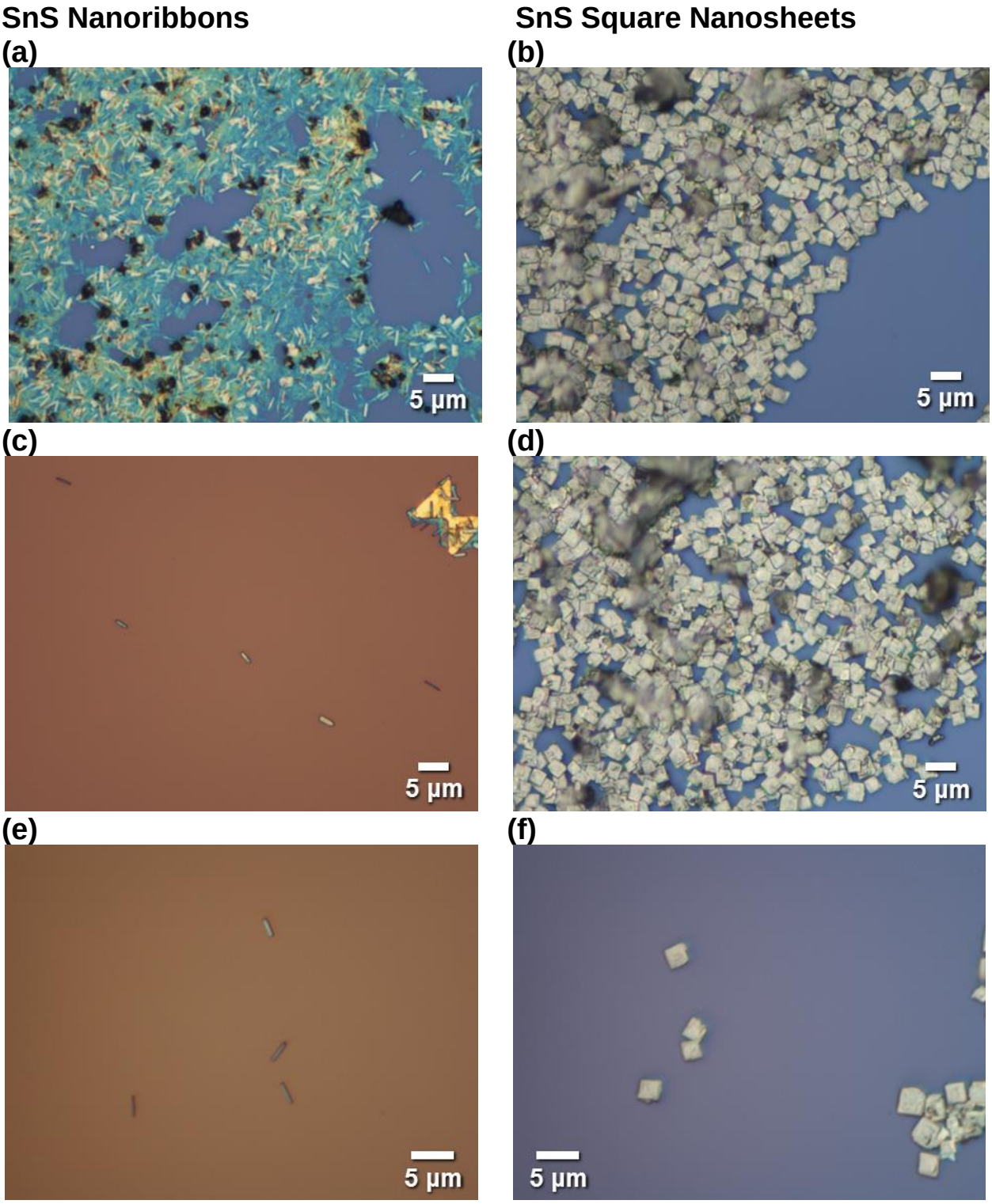

Figure S20. Additional optical microscopy images taken from both concentrated regions (a,b,d) and dilute regions (c,e,f) of drop-cast µm-scale 2D SnS nanoribbons (left column) and square nanosheets (right column).

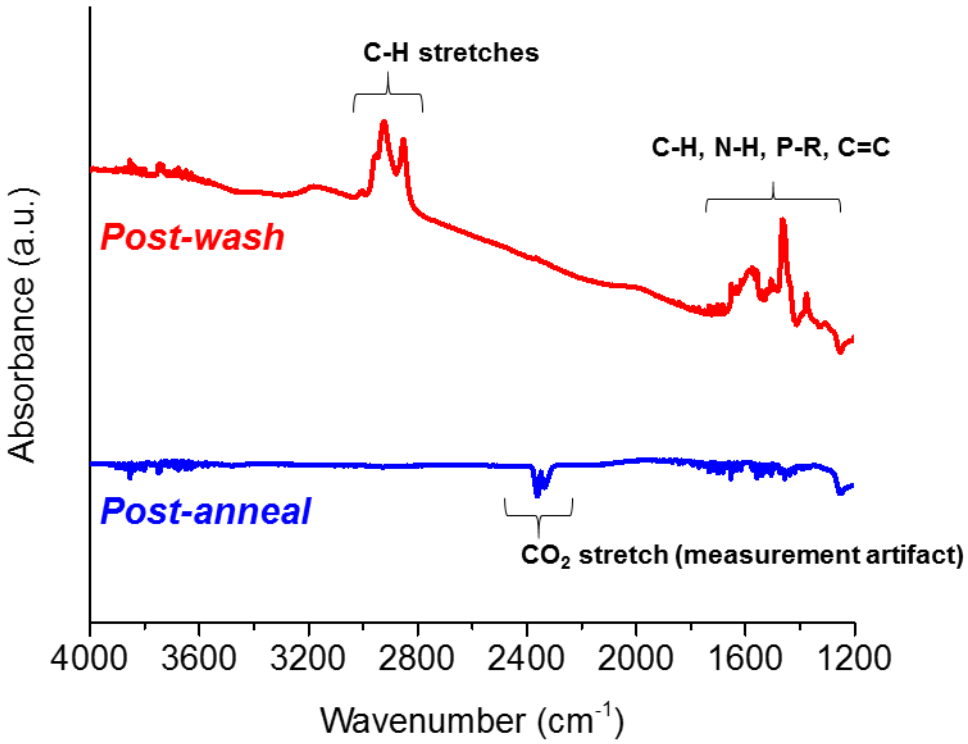

Figure S21. FTIR spectra of SnS nanoribbons prior to annealing (red) and after annealing at 400 °C in forming gas (blue), indicating that organic species present on the surface of the deposited nanocrystals have been removed.

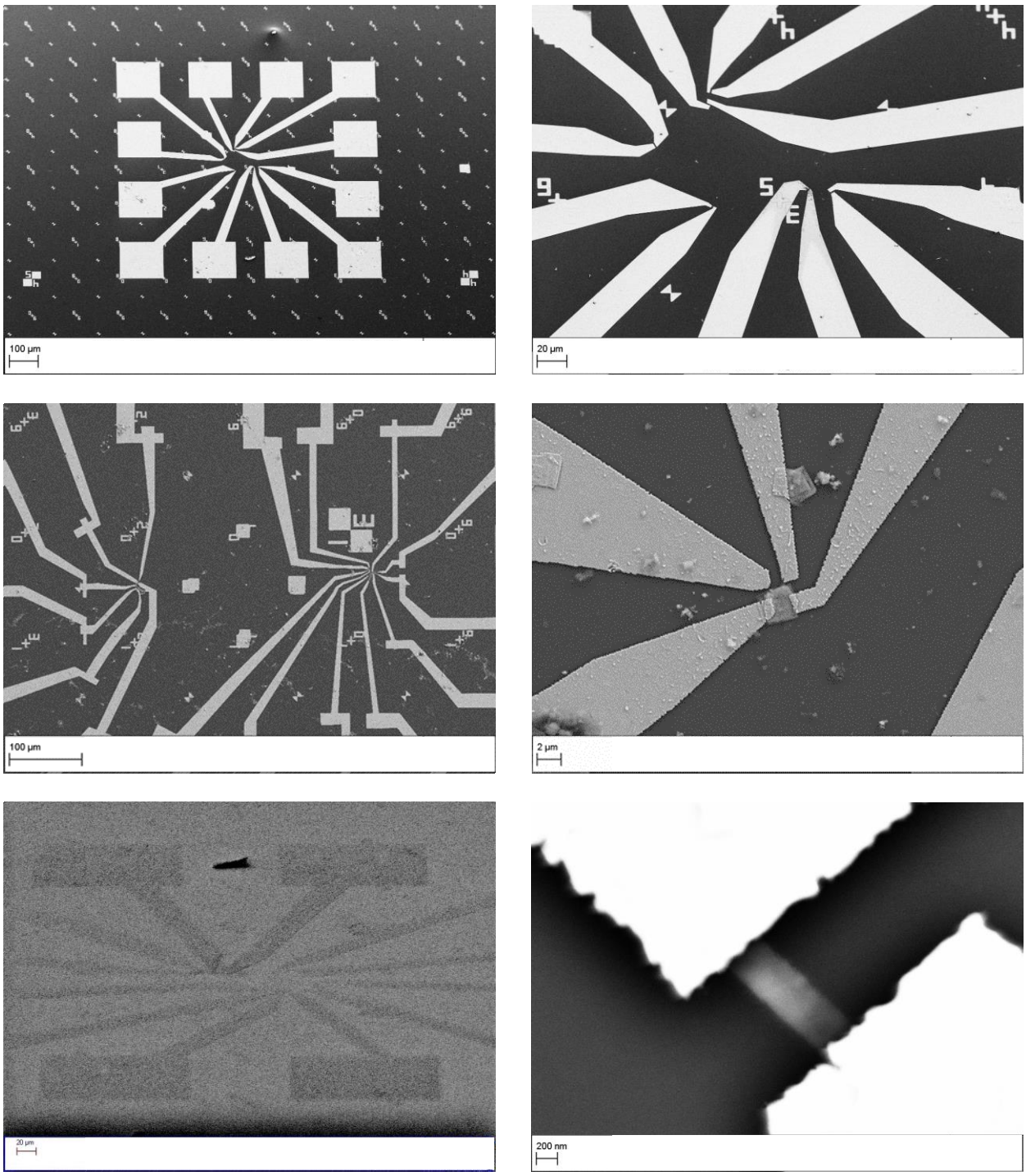

Figure S22. Additional SEM images of fabricated individual SnS nanocrystal device arrays.

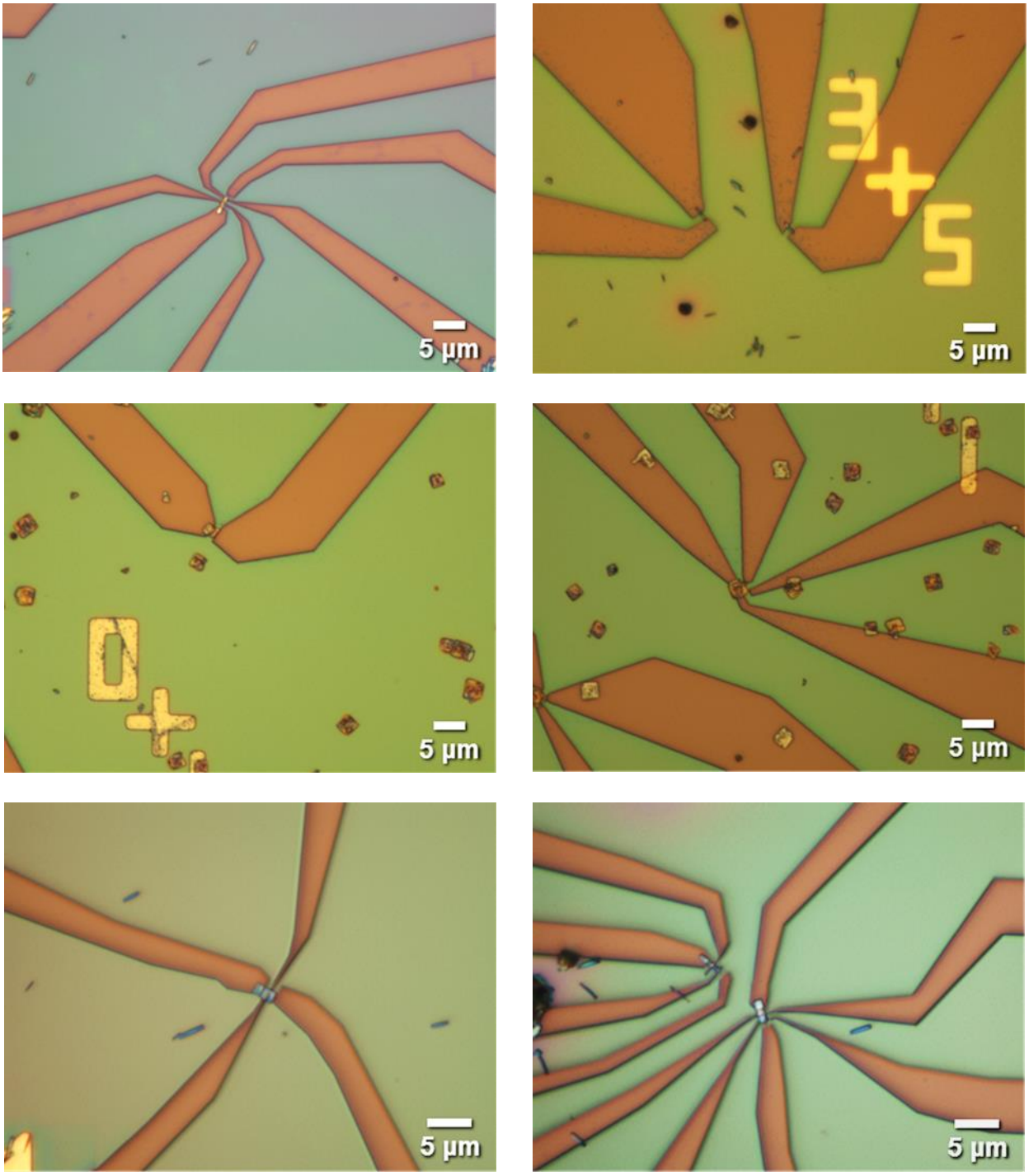

Figure S23. Additional optical images of fabricated individual SnS nanocrystal device arrays.

(a)

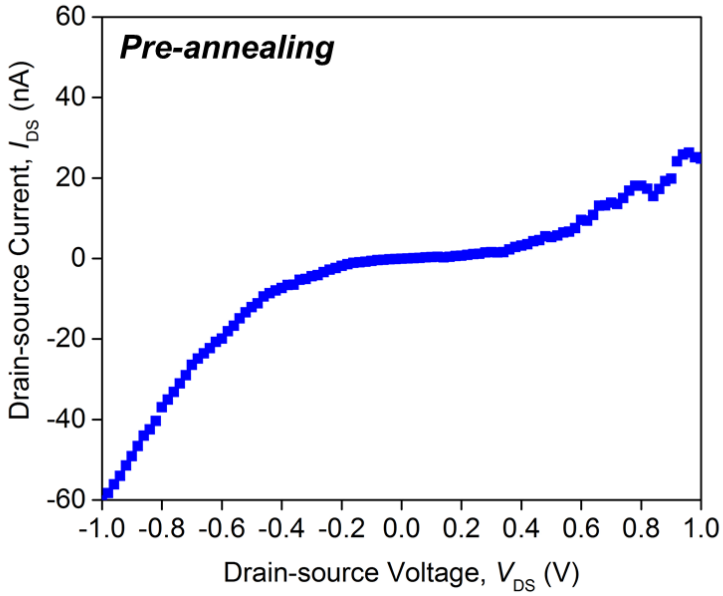

(b)

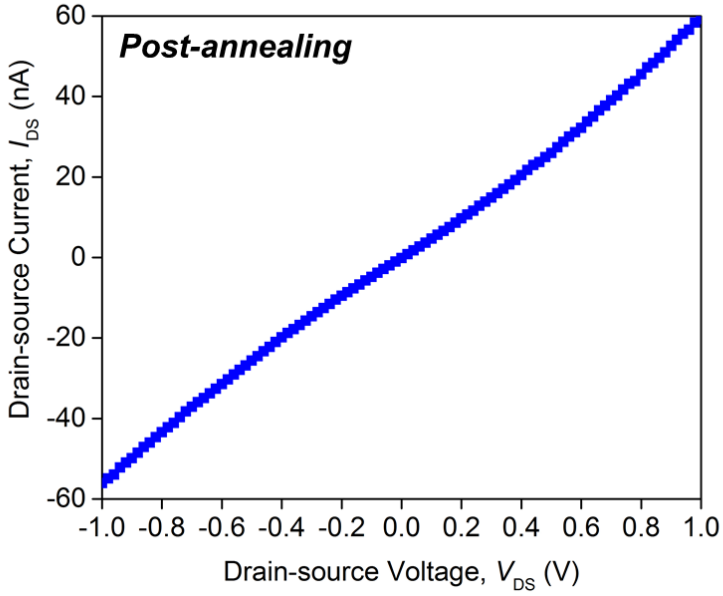

Figure S24. Representative output characteristic at V_{GS} = 0 V (a) before and (b) after annealing of an individual 2D SnS nanocrystal device, indicating a change from Schottky (rectifying) behavior to ohmic behavior.

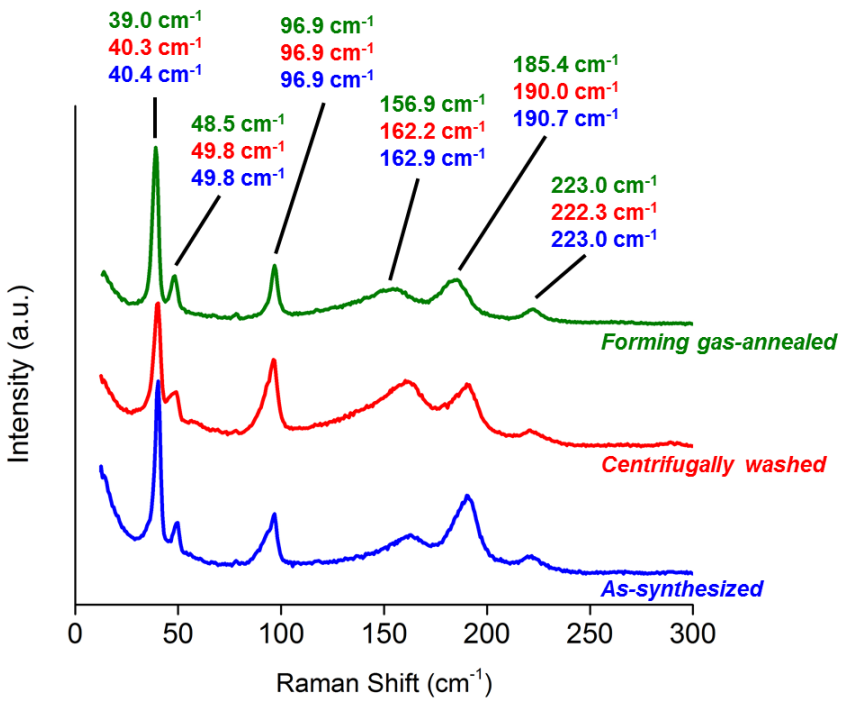

Figure S25. Raman spectra of μm-scale SnS nanoribbons collected as-synthesized, following centrifugal washing, and after the completion of FET devices. Excitation λ = 514 nm. These data indicate that the fidelity of the SnS crystal structure has been maintained throughout the fabrication process

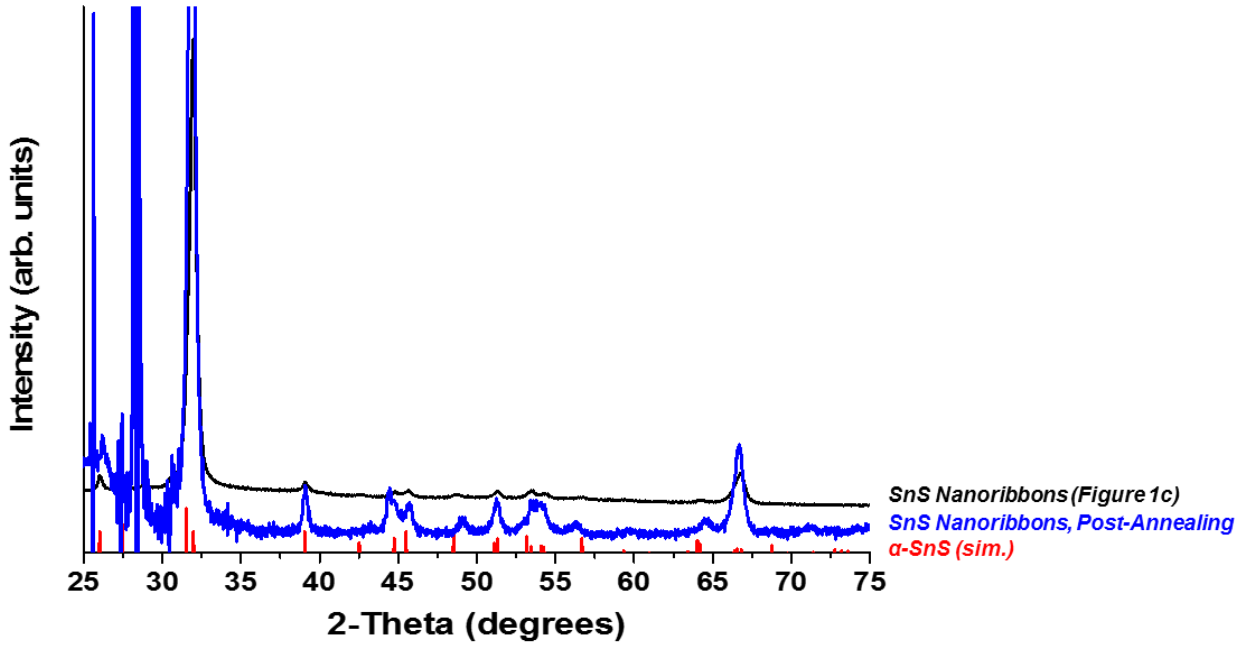

Figure S26. Powder XRD pattern of an ensemble of SnS nanoribbons following annealing at 400 °C in 5% forming gas, indicating that the crystal structure is maintained. The large signals at 25 – 29 °2θ are from the crystalline Si substrate.

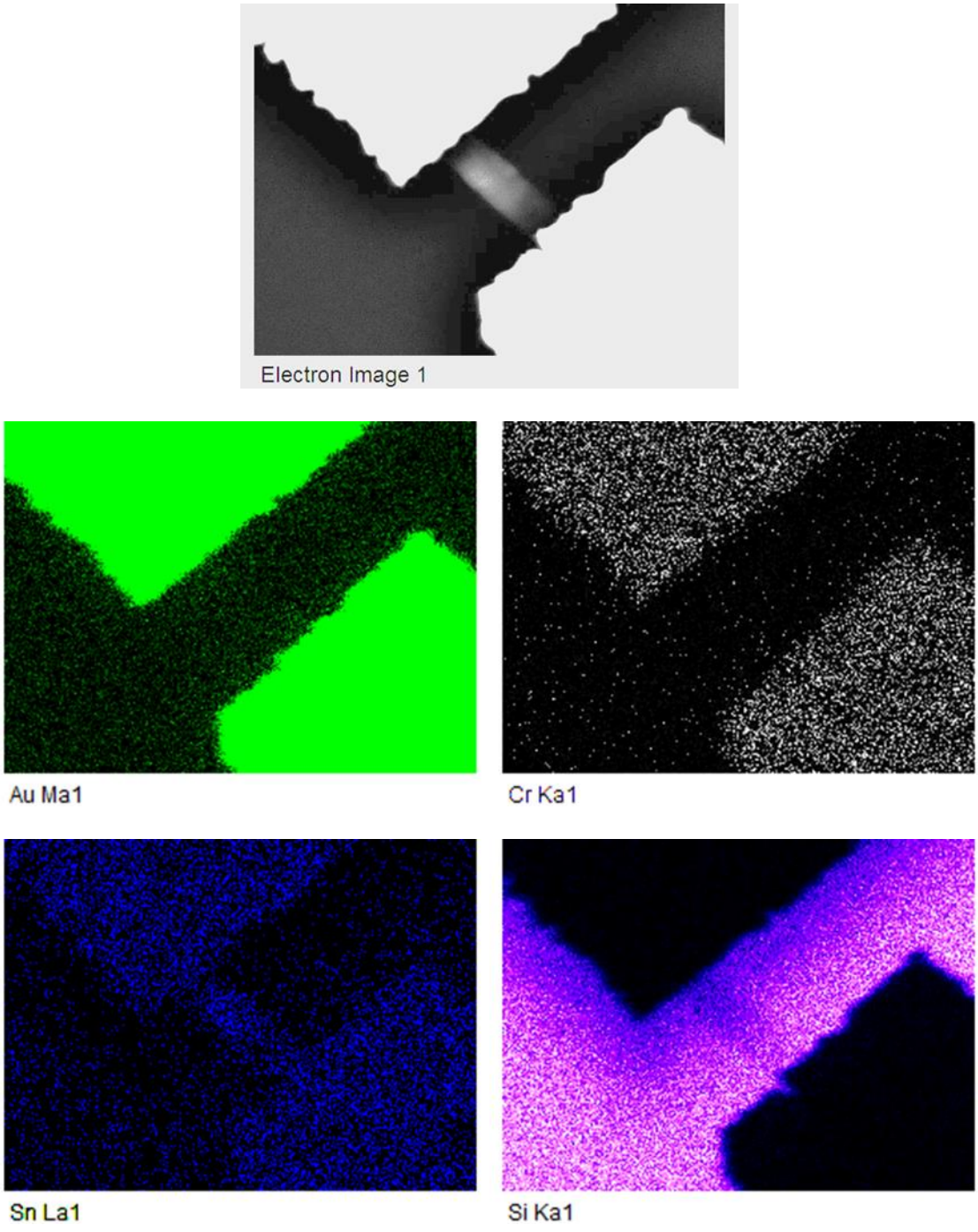

Figure S27. SEM-EDX elemental maps of a fabricated SnS nanoribbon device following annealing, confirming that the device remains intact and indicating that metal from the contacts has not diffused into the semiconductor channel.

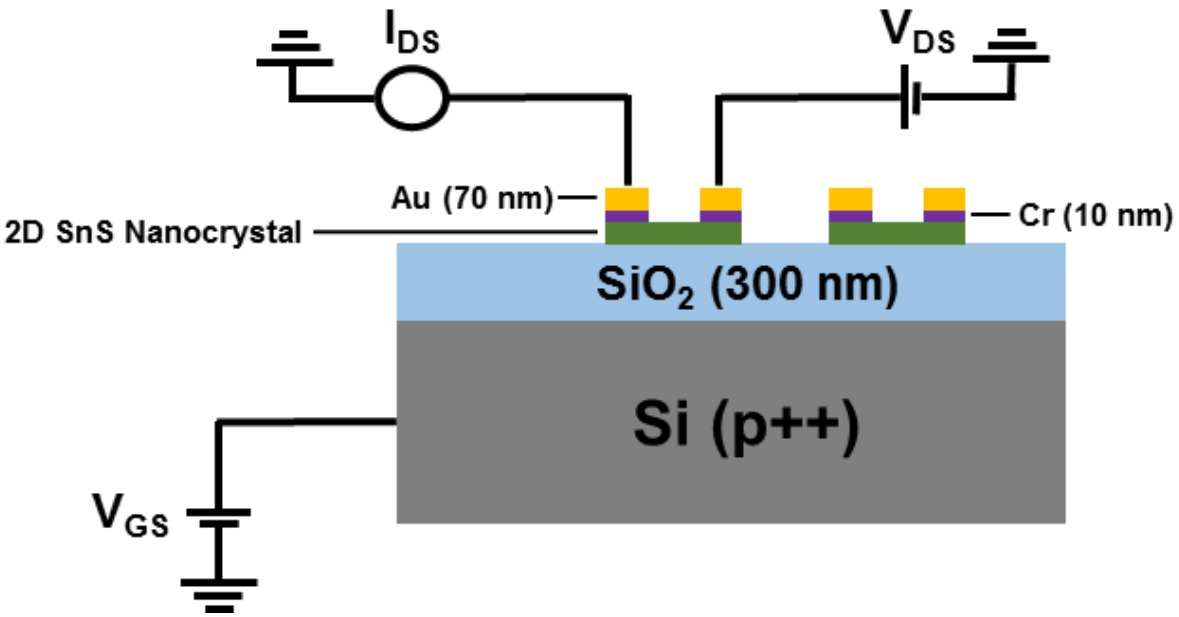

Figure S28. Schematic of individual colloidal 2D SnS nanocrystal-based devices, indicating that they are top-contact, back-gated.

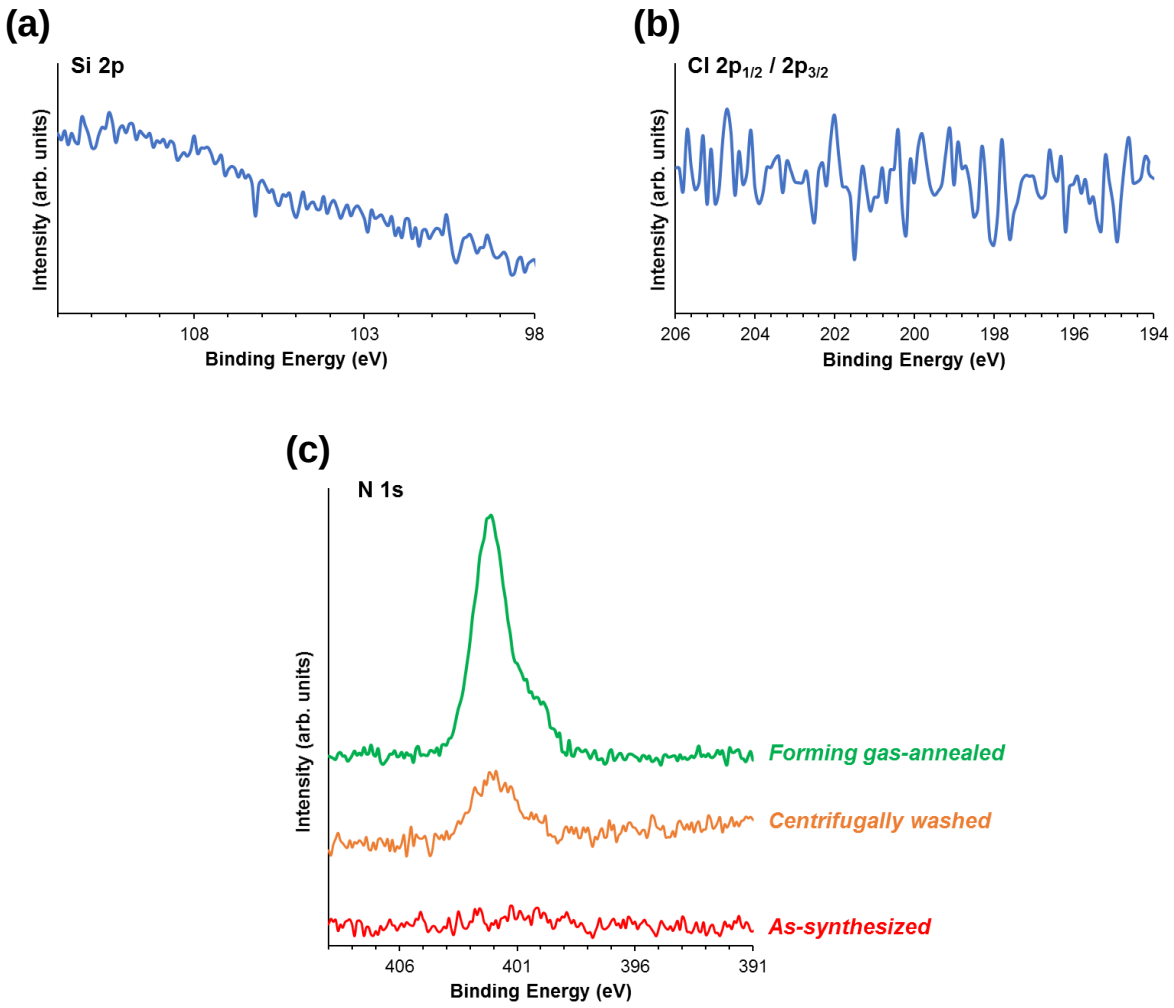

Figure S29. XPS spectra of SnS square nanosheets, centrifugally washed unless otherwise noted. (a) Si 2p region and (b) Cl 2p region, indicating a lack of extrinsic doping by these elements. (c) N 1s region without washing (green), after centrifugal washing (orange), and following annealing in forming gas (red), indicating the removal of OLAM surfactant from the surface.

(a)

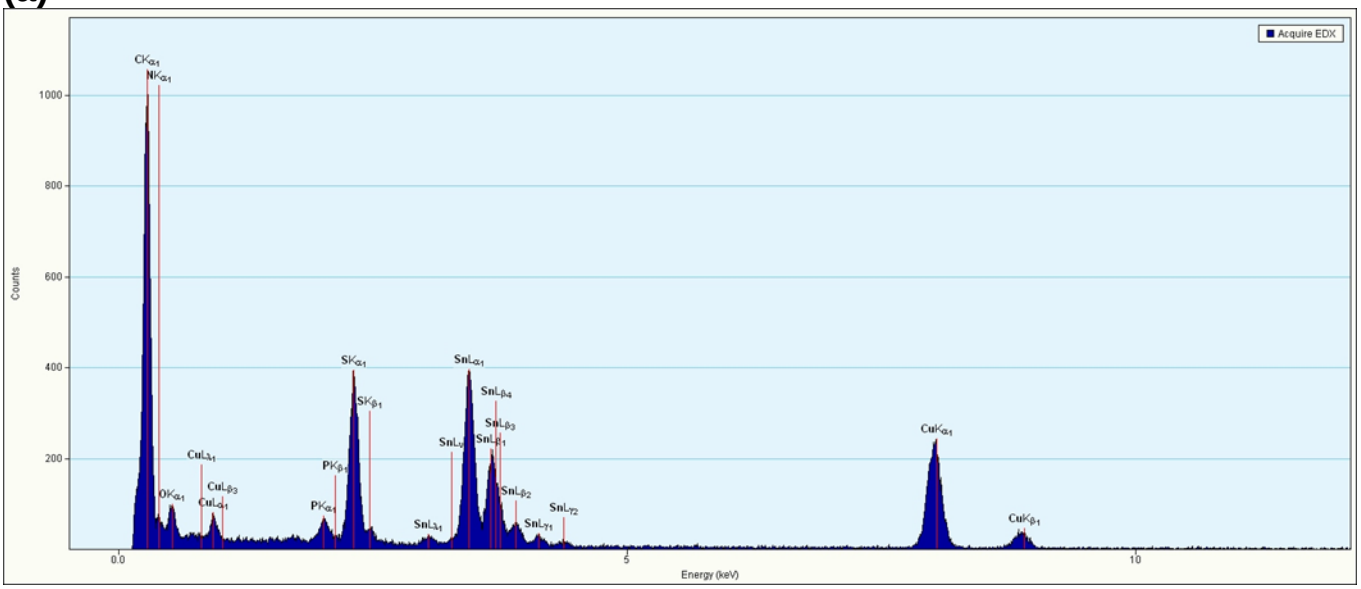

(b)

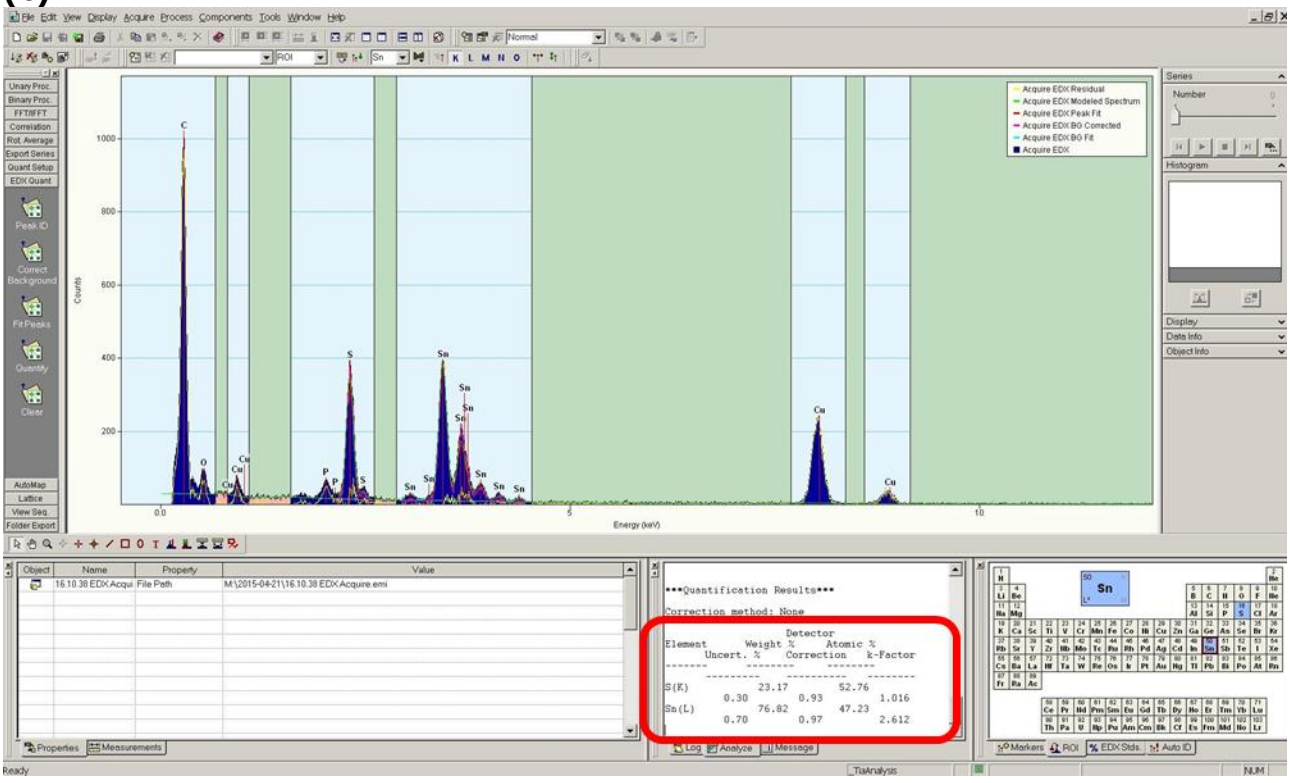

Figure S30. (a)Large-area EDX spectrum and (b) quantitative analysis of SnS nanoribbons, indicating that, stoichiometrically, they are slightly S-heavy (52.76 % S, 47.23 % Sn). Detected C, N, and P are from OLAM and TOP surfactants. Detected Cu is due to the substrate.

(a)

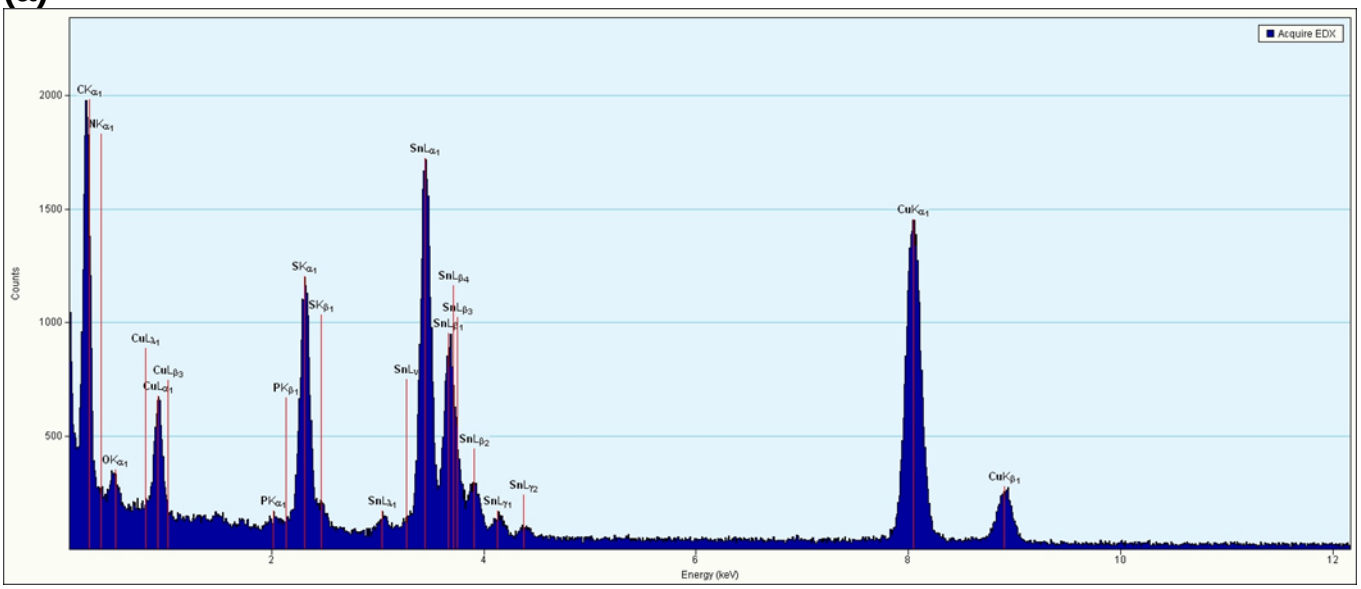

(b)

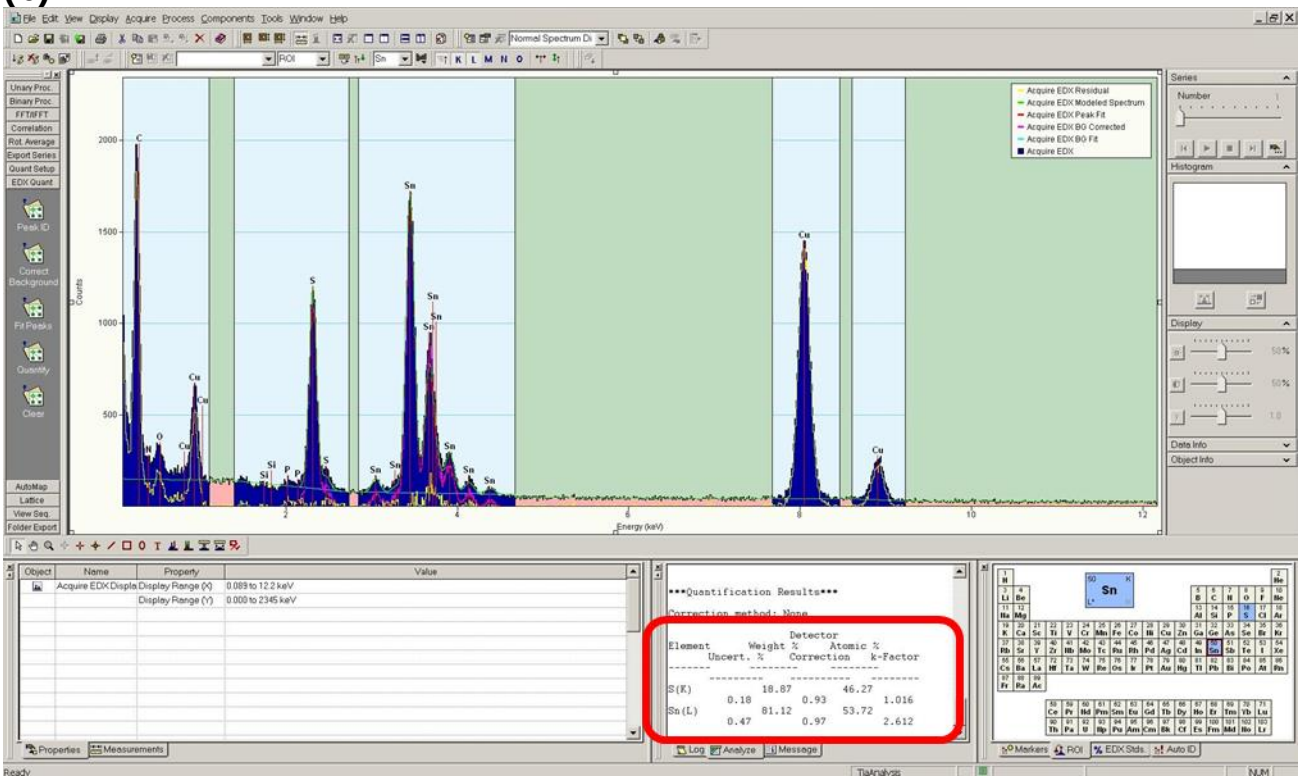

Figure S31. (a) Large-area EDX spectrum and (b) quantitative analysis of SnS square nanosheets, indicating that, stoichiometrically, they are Sn-heavy (46.27 % S, 53.72 % Sn), likely due to the excess Sn^{4+} employed during their synthesis. Detected Cu is due to the substrate.

Additional XPS Analysis Details

To explore the possibility that the relatively low currents displayed by our SnS square nanosheets were due to a thick surface oxide that forms in air, we analyzed the surface composition with XPS. As expected, strong Sn 3d and S 2p peaks were detected (Figure S32). The Sn $3d_{5/2}$ XPS spectrum indicates that an oxide layer is present, as shown by the binding energy feature at 487.1 eV that we ascribed to SnO_x.[3-4] However, the sizeable lower binding energy Sn $3d_{5/2}$ signal located at 485.7 eV corresponds to SnS detected beneath the SnO_x. This implies that the oxide layer must be substantially thinner than the penetration depth of the XPS analysis (8 nm – 10 nm), suggesting the oxide layer at the surface is insufficiently thick to negatively impact performance. Indeed, a thin native oxide passivation layer is potentially advantageous to these semiconductor devices, as they eliminate trap states near the band edges of SnS.[5]

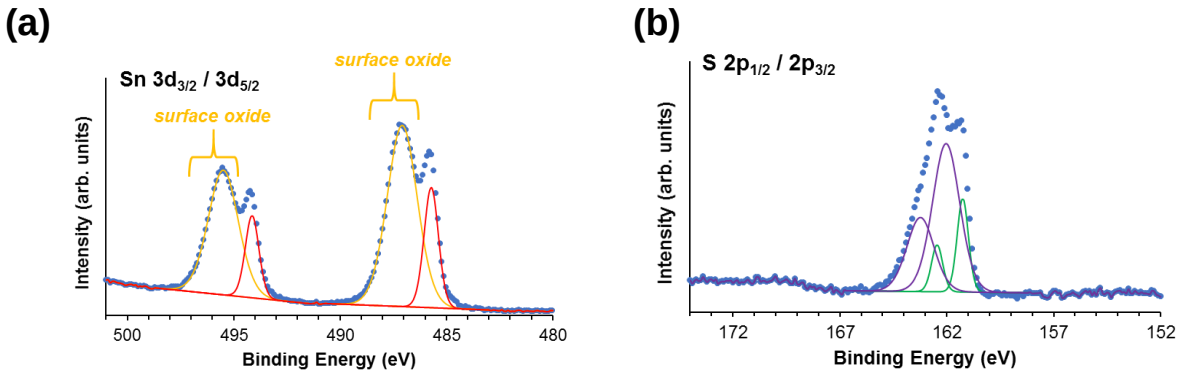

Figure S32. XPS spectra of SnS square nanosheets, centrifugally washed unless otherwise noted. (a) Sn 3d region, indicating the presence of a surface oxide, and (b) S 2p region.

Additional SnS Nanoribbon 4-Point Conductivity Analysis Details

In the case of the nanoribbons, a constant current was forced between the two outermost contacts, which we label 1 and 4, and the differential voltage between the two interior probes, 2 and 3, was measured. For two nanoribbon four-terminal devices, the $I_{DS,1-2}$ - V_{2-3} curves were linear and an average channel resistance of 5.04 x 10^6 Ω was extracted by employing Ohm's law. After establishing the dimensions of the semiconductor channel between contacts 2 and 3 using SEM and optical microscopy, we used the electrical resistivity equation $\rho = \frac{R_{4pt}A}{L}$ where ρ is the resistivity, R_{4pt} is the channel resistance as determined from our four-point measurement, A is the channel area, and L is the channel length, to elucidate the intrinsic material resistivity.

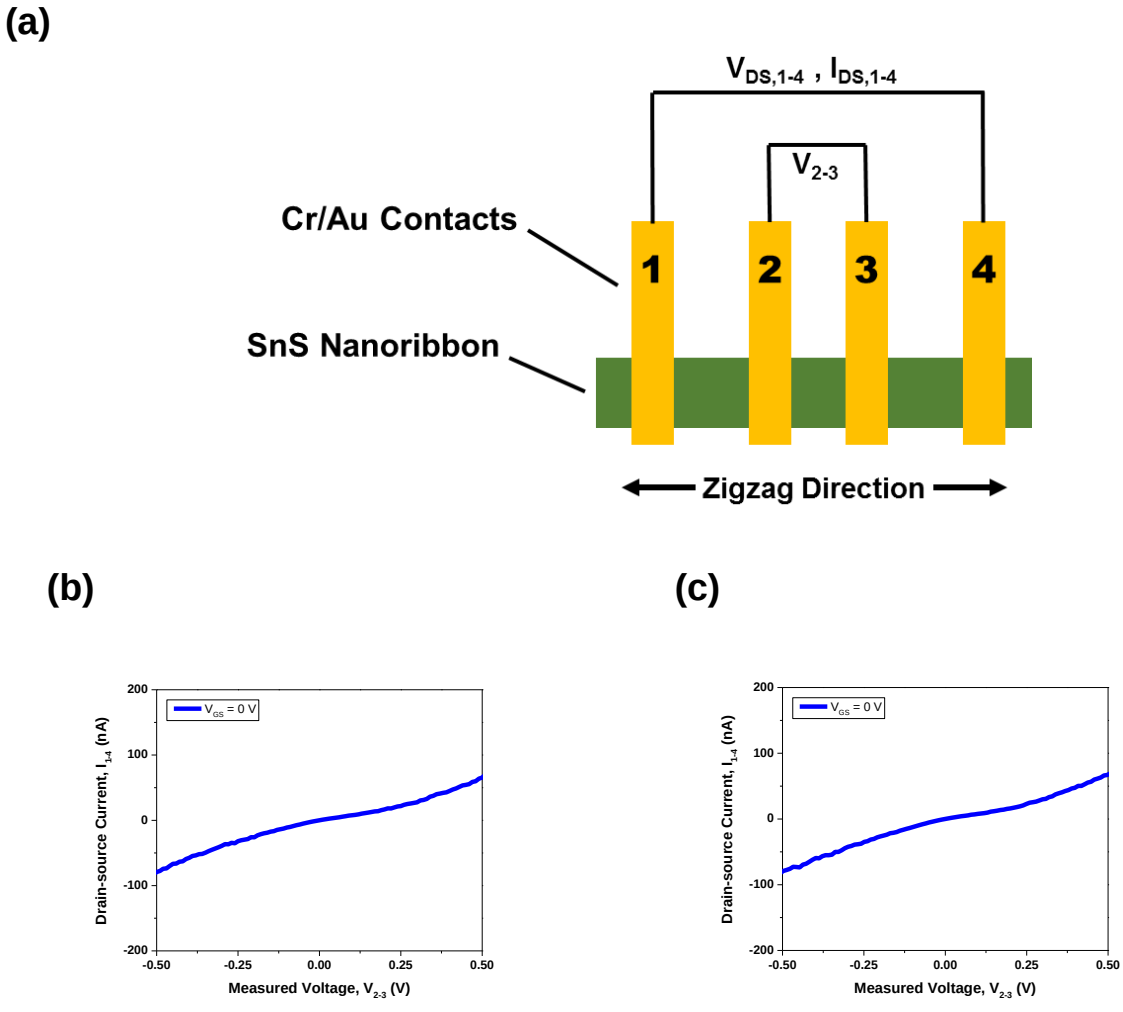

Figure S33. Linear four-point probe conductivity (a) schematic and (b,c) data collected from two SnS nanoribbons.

Additional SnS Square Nanosheet 4-Point Conductivity Analysis Details

Four-point probe analysis of the square nanosheets utilized a van der Pauw configuration, which affords measurements along two directions set off 90° from each other, in this case corresponding to the edges of the square nanocrystals. We found the measured resistances to be highly anisotropic, with an average value of 5.35 x 10^5 Ω in one direction and 8.55 x 10^5 Ω for the orthogonal in-plane direction. The sheet resistance, R_s, was determined by solving the van der Pauw equation,[6] $e^{\frac{-\pi R_X}{R_S}} + e^{\frac{-\pi R_Y}{R_S}} = 1$, where R_x and R_y are the two measured resistances along the edges of our device. Finally, the resistivity of the square nanosheets is calculated by accounting for the thickness of the nanosheet.

(a)

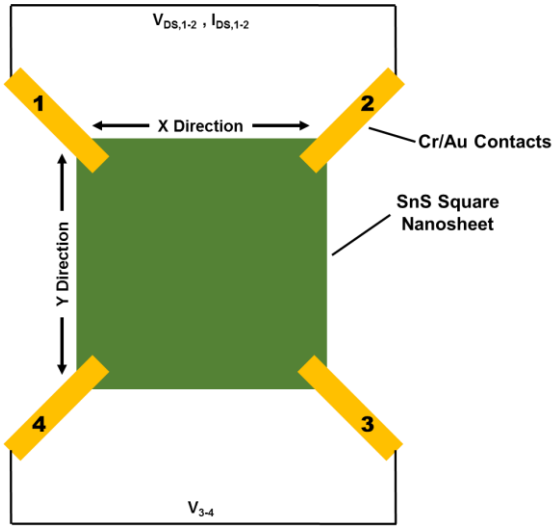

(b) **(c)**

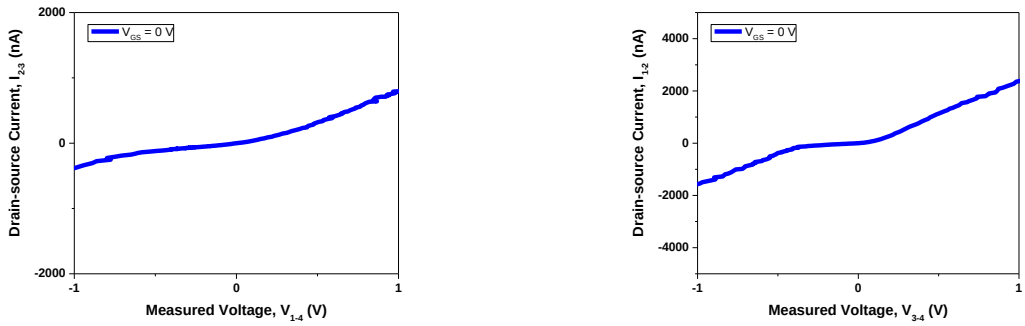

Figure S34. Van der Pauw four-point probe conductivity (a) schematic and (b,c) data collected along two orthogonal directions within the same 2D SnS square nanosheet. The schematic shown in (a) corresponds to the measurements displayed in (c).

Scheme S1. Determination of SnS device field-effect mobility (μ_{FET}).

The field-effect mobility (μ_{FET}) can be calculated from the linear region of a device's transfer characteristic using the equation $\mu_{\mathrm{FET}} = m_{I_{\mathrm{DS}}-V_{\mathrm{GS}}}\left(\frac{L}{W}\right)\left(\frac{1}{V_{\mathrm{DS}}}\right)\left(\frac{1}{C_{\mathrm{ox}}}\right)$, where L and W are the length and width of the channel, V_{DS} is the drain-source voltage, C_{ox} is the gate oxide capacitance per unit area, and $m_{I_{\mathrm{DS}}-V_{\mathrm{GS}}}$ is the slope of the device's linear transfer behavior at low V_{DS}. However, our attempt to extract μ_{FET} at several low V_{DS} values yields discrepant results. For instance, in the case of a two-contact (Cr/Au) SnS nanoribbon FET device fabricated on Si with a 300 nm SiO_2 dielectric (C_{ox} = 1.15 x 10^{-8} F / cm^2) with L = 1270 nm and W = 480 nm:

V_{DS} (V)	$m_{I_{\mathrm{DS}}-V_{\mathrm{GS}}}$ (A / V)	μ_{FET} (cm^2 / V·s)
0.3	4.93 x 10^{-10}	0.38
0.4	1.01 x 10^{-9}	0.58
0.5	1.92 x 10^{-9}	0.88
0.6	2.35 x 10^{-9}	0.90

The inconsistency of μ_{FET} can potentially arise from local non-linearities in the transfer curves, but more likely results from the device resistance associated with the Cr/Au contacts or an interface interaction between SnS and the SiO_2 surface. Unlike Hall mobility[6] and terahertz mobility,[7] these μ_{FET} values correspond to the mobility of the device, rather than the intrinsic mobility of the channel material which, importantly, likely leads to an underestimation of μ relative to the inherent mobility of the semiconductor itself.

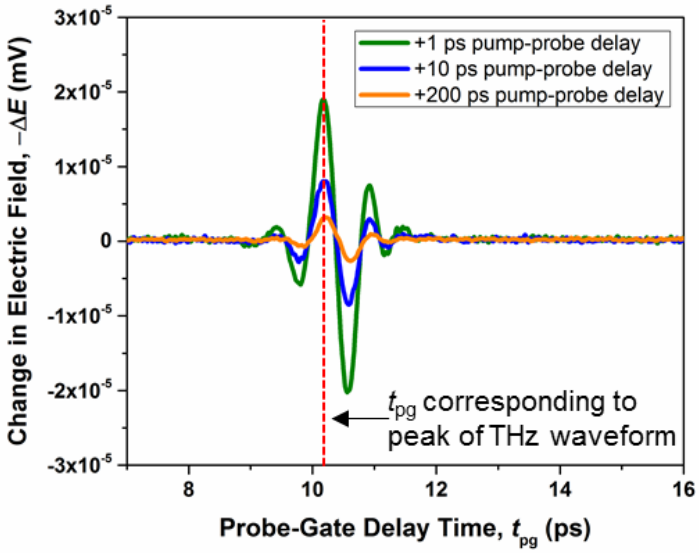

Figure S35. Pumping the deposited 2D SnS with 800 nm excitation induces changes in the terahertz transmission waveform due to increased absorption (larger ΔE) by photogenerated free carriers. The magnitude of these changes decreases with increasing pump-probe delay time, t_{pp}. The probe-gate delay time, t_{pg} was set to correspond with the peak of the THz waveform when collecting the t_{pp}-dependent differential transmission $-\Delta E(t_{pp})$.

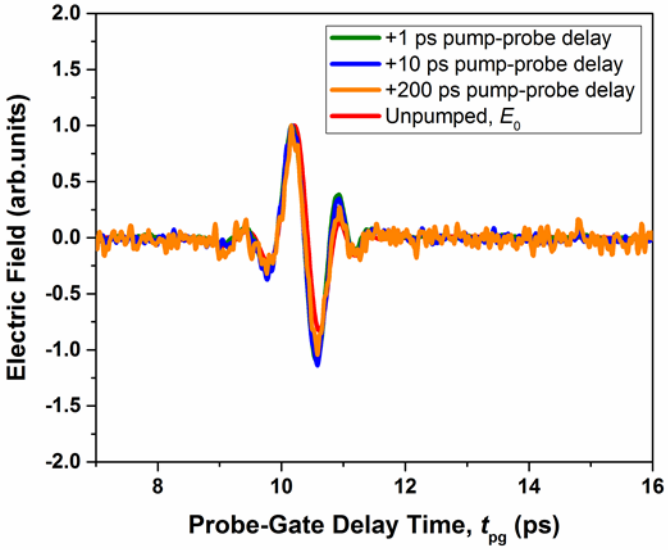

Figure S36. TRTS differential transmission waveforms at several t_{pp} normalized to the signal intensity of the unpumped sample. No observed phase shift is visible, indicating the index of refraction remains constant. (Equation 2 assumes a constant index of refraction of the sample, which was verified by comparing the THz waveforms collected with and without pump beam excitation. In both cases, no discernable phase delay is observed.)

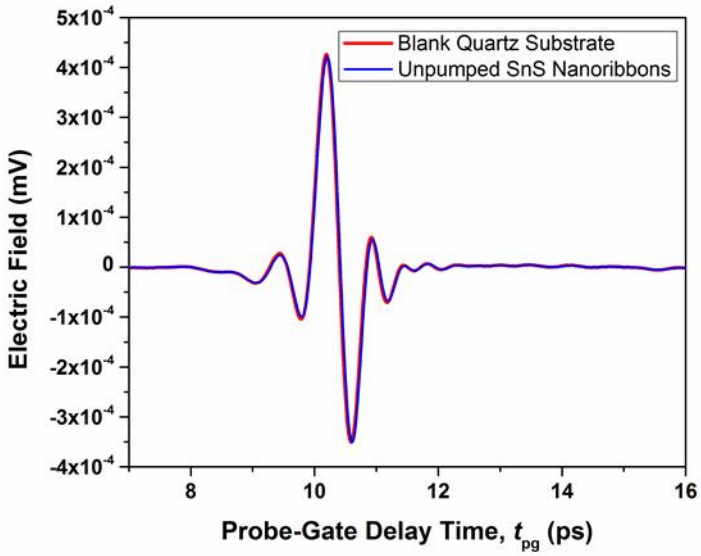

Figure S37. Terahertz time-domain transmission waveforms of SnS nanoribbons deposited on a fused quartz substrate (blue) and the blank substrate (red), demonstrating that the waveform is essentially unchanged without photoexcitation. This indicates that the contribution to TRTS-measured photoconductivity ($\Delta\sigma$) from the inherent, non-photoexcited, SnS free carriers is negligible or smaller than our detection limit. The pump-generated photoconductivity, $\Delta\sigma(t_{pp})$, can be assumed $\approx \sigma(t_{pp})$ if the detected conductivity contribution of the non-photoexcited sample is very low.

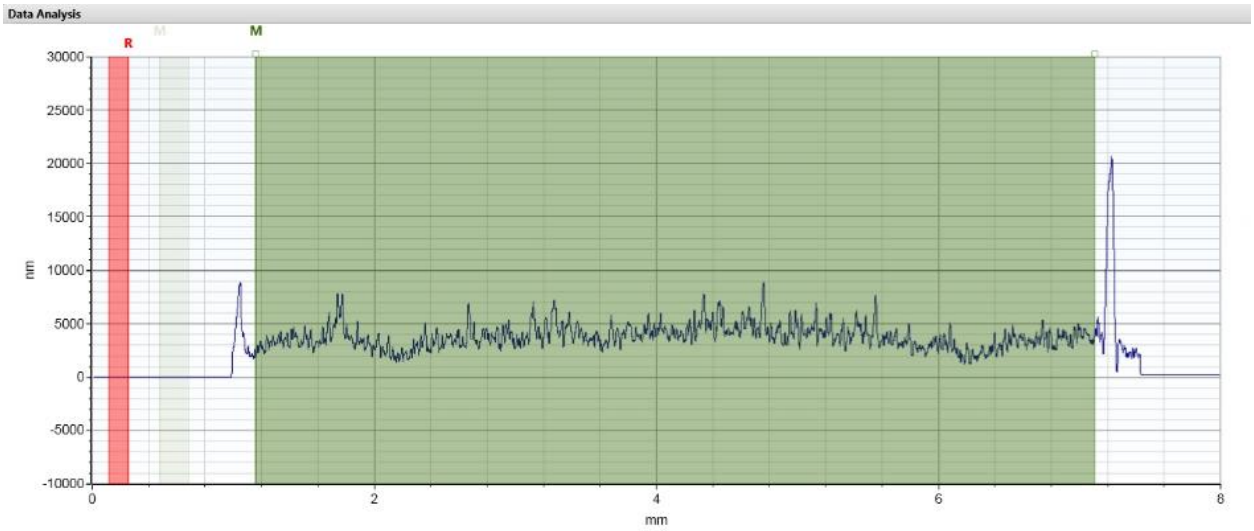

Figure S38. Contact profilometer characterization of a film of SnS nanoribbons drop-cast on a fused quartz substrate, indicating that the average thickness is 3.78 µm.

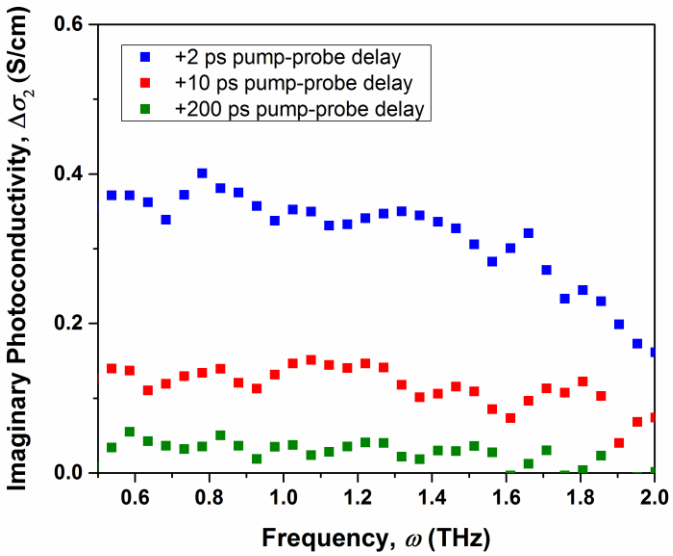

Figure S39. Frequency-dependence of the imaginary part of the THz photoconductivity collected from SnS nanoribbons at three different pump-probe delay times. The positive values of $\Delta\sigma_2$ (in addition to $\Delta\sigma_1$, see Fig. 8b) suggest Drude-like free carrier dynamics and scattering.

Scheme S2. Derivation of the terahertz mobility (μ_T) equation.

To determine the carrier mobility of our samples, start with equation 2, the thin film equation[7]:

$$\Delta\sigma(t_{\mathrm{pp}}) = -\left(\frac{\Delta E(t_{\mathrm{pp}})}{E_0}\right)\left(\frac{n_{\mathrm{THz}}+1}{Z_0 d}\right) \qquad (2)$$

Next, we consider the combined carrier DC conductivity equation for electrons and holes, $\sigma = e(n_{\mathrm{e}}\mu_{\mathrm{e}} + n_{\mathrm{h}}\mu_{\mathrm{h}})$, where *e* is the charge of an electron, *n* is the carrier concentration, and μ is the carrier mobility. If we assume that all free charge carriers are photogenerated by optical excitation in an equal ratio of electron-hole pairs, then $n_e = n_h = N$ and the DC photoconductivity is:

$$\sigma(t_{\mathrm{pp}}) = eN[\mu_{\mathrm{T}}(t_{\mathrm{pp}})] \qquad (S1)$$

where the terahertz mobility, μ_T, is equal to the sum of the carrier mobilities, ($\mu_e + \mu_h$). The charge carrier concentration resulting from photoexcitation was estimated according to:

$$N = \frac{\varphi FA}{d} \qquad (S2)$$

where φ is the charge carrier photogeneration efficiency, *F* is the excitation fluence in photons / cm^2, and the absorbance *A* is equal to (1-*R*-*T*), where *R* and *T* is the fraction of pump photon reflection and transmission, respectively. Combining Equation 2, Equation S1, and Equation S2 for a system where $\Delta\sigma(t_{pp})$ can be assumed $\approx \sigma(t_{pp})$ (see Figure S37), we find the time-dependent terahertz mobility (Equation 3 in the main text):

$$\mu_T(t_{\mathrm{pp}}) = -\left(\frac{\Delta E(t_{\mathrm{pp}})}{E_0}\right)\left(\frac{n_{\mathrm{THz}}+1}{Z_0 e\varphi FA}\right) \qquad (3)$$

Scheme S3. Derivation of the approx. relationship between μ_e and μ_h with μ_T in TRTS.

We propose the following scheme to approximate the deconvolution of a 2D materials' individual carrier mobilities, $\mu_{e,xy}$ and $\mu_{h,xy}$, from the TRTS-measured μ_T.

According to the Drude model, the drift mobility of a carrier, μ, can be expressed in terms of the scattering time, τ, and the effective mass, m^*:

$$\mu = \frac{e\tau}{m^*} \tag{S3}$$

At room temperature, carrier scattering is primarily due to lattice (aka phonon) scattering, as opposed to impurity scattering. Derived from Fermi's Golden Rule, the acoustic phonon-limited momentum scattering time for 2D and layered materials is:[8-10]

$$\tau = \frac{\hbar^3 \rho v_s^2}{m_{xy}^* E_d^2 k_B T} \tag{S4}$$

where ρ is mass density, v_s is longitudinal sound velocity, T is temperature, E_d is the composite deformation potential, and m^*_{xy} is the composite of the 2D in-plane directions. This approximation assumes photoinduced current primarily in the in-plane directions, and the model is valid only when transport is substantially less favorable in the out-of-plane direction. Combining S3 and S4 gives the in-plane carrier mobility as:

$$\mu_{xy} = \frac{e\frac{\hbar^3 \rho v_s^2}{m_{xy}^* E_d^2 k_B T}}{m_{xy}^*} = \frac{e\hbar^3 \rho v_s^2}{(m_{xy}^*)^2 E_d^2 k_B T} = A\left(\frac{1}{m_{xy}^* E_d}\right)^2 \tag{S5}$$

where A is a set of carrier-independent constants for a given 2D material at a steady state temperature. Therefore, the relationship between $\mu_{e,xy}$ and $\mu_{h,xy}$ can be expressed:

$$\frac{\mu_{e,xy}}{\mu_{h,xy}} = \frac{A\left(\frac{1}{m_{e,xy}^* E_{d,e}}\right)^2}{A\left(\frac{1}{m_{h,xy}^* E_{d,h}}\right)^2}$$

or:

$$\mu_{e,xy} = \mu_{h,xy}\left(\frac{m_{h,xy}^* E_{d,h}}{m_{e,xy}^* E_{d,e}}\right)^2 \quad \text{and} \quad \mu_{h,xy} = \mu_{e,xy}\left(\frac{m_{e,xy}^* E_{d,e}}{m_{h,xy}^* E_{d,h}}\right)^2 \tag{S6}$$

which we take as an approximation of the collective in-plane carrier mobility in terms of the in-plane mobility of the complimentary carrier for a 2D or layered material. This can then be combined with the TRTS mobility relation $\mu_e + \mu_h = \mu_T$ to yield:

$$\mu_{h,xy} = \frac{\mu_T}{1+\left(\frac{m_{h,xy}^* E_{d,h}}{m_{e,xy}^* E_{d,e}}\right)^2} \quad \text{and} \quad \mu_{e,xy} = \frac{\mu_T}{1+\left(\frac{m_{e,xy}^* E_{d,e}}{m_{h,xy}^* E_{d,h}}\right)^2} \tag{4}$$

which is an estimation of the mobility of individual carriers in terms of μ_T, E_d, and m^*_{xy}. Note that the resultant carrier mobility has contribution from multiple in-plane directions unless μ_T was collected with a polarized TRTS measurement on a single crystal. In that case, values of E_d and m^* correspond to the investigated crystallographic orientation.

Scheme S4. Calculation of TRTS-measured independent carrier mobilities for SnS nanoribbons and square nanosheets.

m^* and E_d for α-SnS were tabulated from a variety of reports to provide a consensus calculation from first principles.[10-14] After calculating the geometric mean from the direction-dependent values, we used the following parameters in our analysis:
$m^*_{h,xy} = 0.26m_0$ $m^*_{e,xy} = 0.17m_0$ $E_{d,h} = 18.4$ eV $E_{d,e} = 13.2$ eV

The values of μ_T obtained from TRTS at $t_{pp} = 10$ ps were $\mu_T = 26.5$ cm^2/V·s for the SnS nanoribbons and $\mu_T = 158.0$ cm^2/V·s for the square nanosheets (assuming $\varphi = 1$).

Employing Equation 4, this gives the following in-plane carrier mobilities:

SnS nanoribbons:	$\mu_{h,xy} = 4.8$ cm^2 / V·s	$\mu_{e,xy} = 22$ cm^2 / V·s
SnS square nanosheets:	$\mu_{h,xy} = 29$ cm^2 / V·s	$\mu_{e,xy} = 130$ cm^2 / V·s

Scheme S5. A method for approximating the direction-dependent carrier mobilities μ_x and μ_y from the in-plane carrier mobility μ_{xy}.

The transport direction-dependent variation of Equation S5, the carrier mobility equation for either electrons or holes in 2D or layered materials, is:

$$\mu_x = \frac{e\hbar^3\rho v_s^2}{m_x^* m_{xy}^* E_{d,x} E_{d,xy} k_B T} = A\frac{1}{m_x^* m_{xy}^* E_{d,x} E_{d,xy}} \quad \text{(S7)}$$

where A is a set of carrier-independent constants for a given 2D material at a steady state temperature. Therefore, the relationship between $\mu_{e,x}$ and $\mu_{e,y}$ can be expressed:

$$\frac{\mu_{e,x}}{\mu_{e,y}} = \frac{A\frac{1}{m_{e,x}^* m_{e,xy}^* E_{d,e,x} E_{d,e,xy}}}{A\frac{1}{m_{e,y}^* m_{e,xy}^* E_{d,e,y} E_{d,e,xy}}}$$

Or:

$$\mu_{e,x} = \mu_{e,y}\left(\frac{m_{e,y}^* E_{d,e,y}}{m_{e,x}^* E_{d,e,x}}\right) \text{ and } \mu_{e,y} = \mu_{e,x}\left(\frac{m_{e,x}^* E_{d,e,x}}{m_{e,y}^* E_{d,e,y}}\right) \quad \text{(S8)}$$

and likewise for hole mobility. Assuming that the direction-specific carrier mobilities can be estimated from the composite in-plane mobility using a geometric mean, where $\mu_{xy} = \sqrt{\mu_x \mu_y}$, then we propose:

$$\mu_x = \sqrt{\left(\frac{m_x^* E_{d,x}}{m_y^* E_{d,y}}\right)}\mu_{xy} \quad \text{and} \quad \mu_y = \sqrt{\left(\frac{m_y^* E_{d,y}}{m_x^* E_{d,x}}\right)}\mu_{xy} \quad \text{(5)}$$

where values of μ, m^*, and E_d are all carrier-dependent.

Scheme S5. Calculation of TRTS-measured direction-dependent carrier mobilities μ_x and μ_y from the in-plane mobility μ_{xy}.

Direction-dependent values of m^* and E_d for α-SnS were taken from Guo, *et al.*[10]:

$m^*_{h,zigzag} = 0.21m_0$ $m^*_{e,zigzag} = 0.15m_0$ $E_{d,h,zigzag} = 21.9$ eV $E_{d,e,zigzag} = 11.0$ eV

$m^*_{h,armchair} = 0.36m_0$ $m^*_{e,armchair} = 0.20m_0$ $E_{d,h,armchair} = 19.1$ eV $E_{d,e,armchair} = 14.6$ eV

Using Equation 5 and the values of $\mu_{h,xy}$ and $\mu_{e,xy}$ previously extracted from TRTS data, we approximate direction-dependent carrier mobilities in our 2D SnS nanocrystals:

SnS nanoribbons:	$\mu_{h,zigzag} = 5.8$ cm^2 / V·s	$\mu_{e,zigzag} = 29$ cm^2 / V·s
	$\mu_{h,armchair} = 3.9$ cm^2 / V·s	$\mu_{e,armchair} = 16$ cm^2 / V·s
SnS square nanosheets:	$\mu_{h,zigzag} = 35$ cm^2 / V·s	$\mu_{e,zigzag} = 170$ cm^2 / V·s
	$\mu_{h,armchair} = 23$ cm^2 / V·s	$\mu_{e,armchair} = 97$ cm^2 / V·s

Table S1. Reported electronic transport properties for undoped SnS at room temperature collected from various references. (NR = not reported)

Reference Number	Synthesis	Structure	Conductivity (S / cm)	Majority carrier	Hall mobility (cm^2 / V·s)	Carrier concentration (cm^{-3})
15	PVD	Single crystal	0.0083	h^+	34	1.52×10^{15}
16	Bridgman-Stockbarger	Single crystal	2.08	h^+	65	2×10^{17}
17	Bridgman-Stockbarger	Single crystal	NR	h^+	90	4×10^{17}
18	Bridgman-Stockbarger	Single crystal	0.019	h^+	48	2.68×10^{15}
19	Bridgman-Stockbarger	Single crystal	0.193	h^+	NR	5.07×10^{13}
20	Exfoliation	Single crystal	NR	h^+	10 - 25	4.0×10^{11}
21	Solution synthesis	Dropcast films of crystals	0.93	h^+	5.7	1×10^{18}
22	Spray pyrolysis	Polycrystalline thin film	0.033	e^-	130	1.6×10^{15}
23	Vacuum evaporation	Polycrystalline thin film	0.05-0.077	h^+	400 - 500	6.3×10^{14} - 1.2×10^{15}
24	ALD	Polycrystalline thin film	0.0014 - 0.017	h^+	0.82 - 15.3	6.9×10^{15} - 1.5×10^{16}
25	Pulsed laser deposition	Polycrystalline thin film	0.024	h^+	25 - 37	4×10^{15}
26	CVD	Polycrystalline thin film	0.001 - 0.01	h^+	3 - 10	10^{15} - 10^{16}
27	Thermal evaporation	Polycrystalline thin film	0.02 - 0.16	h^+	20.1 - 31.6	6.3×10^{15} - 3.1×10^{16}
28	CVT	Polycrystalline thin film	0.069	h^+	3.73	1.16×10^{17}
29	Vacuum evaporation	Polycrystalline thin film	0.008 - 0.012	h^+	0.8 - 31.6	1.7×10^{15} - 9.0×10^{16}

Supporting Information References.

(1.) Villars, P. *Pearson's Handbook Desk Edition: Crystallography Data for Intermetallic Phases*; ASM International: Materials Park, OH, 1998.

(2.) Biacchi, A. J.; Vaughn, D. D.; Schaak, R. E. Synthesis and Crystallographic Analysis of Shape-Controlled SnS Nanocrystal Photocatalysts: Evidence for a Pseudotetragonal Structural Modification. *J. Am. Chem. Soc.* **2013,** *135*, 11634-11644.

(3.) Whittles, T. J.; Burton, L. A.; Skelton, J. M.; Walsh, A.; Veal, T. D.; Dhanak, V. R. Band Alignments, Valence Bands, and Core Levels in the Tin Sulfides SnS, SnS2, and Sn2S3: Experiment and Theory. *Chem. Mater.* **2016**, *28*, 3718-3726.

(4.) NIST X-ray Photoelectron Spectroscopy Database. https://srdata.nist.gov/xps/Default.aspx (accessed October 26, 2017).

(5.) Tritsaris, G. A.; Malone, B. D.; Kaxiras, E. Structural stability and electronic properties of low-index surfaces of SnS. *J. Appl. Phys.* **2014**, *115*, 173702.

(6.) van der Pauw, L. J. A Method of Measuring Specific Resistivity and Hall Effect of Discs of Arbitrary Shape. *Philips Res. Rep.* **1958**, *13*, 1-9.

(7.) Hegmann, F. A.; Ostroverkhova, O.; Cooke, D. G., *Photophysics of Molecular Materials*. Wiley-VCH: Weinheim, 2006.

(8.) Li, S.-L.; Tsukagoshi, K.; Orgiu, E.; Samori, P. Charge Transport and Mobility Engineering in Two-Dimensional Transition Metal Chalcogenide Semiconductors. *Chem. Soc. Rev.* **2016**, *45*, 118-151.

(9.) Strait, J. H.; Nene, P.; Rana, F. High Intrinsic Mobility and Ultrafast Carrier Dynamics in Multilayer Metal-Dichalcogenide MoS_2. *Phys. Rev. B* **2014**, *90*, 245402.

(10.) Guo, R.; Wang, X.; Kuang, Y.; Huang, B. First-Principles Study of Anisotropic Thermoelectric Transport Properties of IV-VI Semiconductor Compounds SnSe and SnS. *Phys. Rev. B* **2015**, *92*, 115202.

(11.) Vidal, J.; Lany, S.; d'Avezac, M.; Zunger, A.; Zakutayev, A.; Francis, J.; Tate, J. Band-structure, Optical Properties, and Defect Physics of the Photovoltaic Semiconductor SnS. *Appl. Phys. Lett.* **2012**, *100*, 032104.

(12.) Xin, C.; Zheng, J.; Su, Y.; Li, S.; Zhang, B.; Feng, Y.; Pan, F. Few-Layer Tin Sulfide: A New Black-Phosphorus-Analogue 2D Material with a Sizeable Band Gap, Odd–Even Quantum Confinement Effect, and High Carrier Mobility. *J. Phys. Chem. C* **2016**, *120*, 22663-22669.

(13.) Tritsaris, G. A.; Malone, B. D.; Kaxiras, E. Optoelectronic Properties of Single-Layer, Double-Layer, and Bulk Tin Sulfide: A Theoretical Study. *J. Appl. Phys.* **2013**, *113*, 233507.

(14.) Shafique, A.; Shin, Y.-H. Thermoelectric and Phonon Transport Properties of Two-Dimensional IV–VI Compounds. *Sci. Rep.* **2017**, *7*, 506.

(15.) Hegde, S. S.; Kunjomana, A. G.; Chandrasekharan, K. A.; Ramesh, K.; Prashantha, M. Optical and Electrical Properties of SnS Semiconductor Crystals Grown by Physical Vapor Deposition Technique. *Physica B* **2011**, *406*, 1143-1148.

(16.) Albers, W.; Haas, C.; van der Maesen, F. The Preparation and the Electrical and Optical Properties of SnS Crystals. *J. Phys. Chem. Solids* **1960**, *15*, 306-310.

(17.) Albers, W.; Haas, C.; Vink, H. J.; Wasscher, J. D. Investigations on SnS. *J. Appl. Phys.* **1961**, *32*, 2220-2225.

(18.) Patel, T. H.; Vaidya, R.; Patel, S. G. Growth and Transport Properties of Tin Monosulphoselenide Single Crystals. *J. Cryst. Growth* **2003**, *253*, 52-58.

(19.) Nassary. M. M. Temperature Dependence of the Electrical Conductivity, Hall Effect and Thermoelectric Power of SnS Single Crystals. *J. Alloys Compd.* **2005**, *398*, 21-25.

(20.) Sucharitakul, S.; Kumar, U. R.; Sankar, R.; Chou, F.-C.; Chen, Y.-T.; Wang, C.; He, C.; He, R.; Gao, X. P. A. Screening Limited Switching Performance of Multilayer 2D Semiconductor FETs: the Case for SnS. *Nanoscale* **2016**, *8*, 19050-19057.

(21.) Herron, S. M.; Tanskanen, J. T.; Roelofs, K. E.; Bent, S. F. Highly Textured Tin(II) Sulfide Thin Films Formed from Sheetlike Nanocrystal Inks. *Chem. Mater.* **2014**, *26*, 7106-7113.

(22.) Koteeswara Reddy, N.; Ramakrishna Reddy, K. T. Electrical Properties of Spray Pyrolytic Tin Sulfide Films. *Solid-State Electron.* **2005**, *49*, 902-906.

(23.) Noguchi, H.; Setiyadi, A.; Tanamura, H.; Nagatomo, T.; Omoto, O. Molecular Beam Epitaxy Growth of High Quality p-Doped SnS van der Waals Epitaxy on a Graphene Buffer Layer. *Sol. Energy Mater. Sol. Cells* **1994**, *35*, 325-331.

(24.) Sinsermsuksakul, P.; Heo, J.; Noh, W.; Hock, A. S.; Gordon, R. G. Atomic Layer Deposition of Tin Monosulfide Thin Films. *Adv. Energy Mater.* **2011**, *1*, 1116-1125.

(25.) Ran, F.-Y.; Xiao, Z.; Hiramatsu, H.; Hosono, H.; Kamiya, T. Growth of High-Quality SnS Epitaxial Films by H_2S Flow Pulsed Laser Deposition. *Appl. Phys. Lett.* **2014**, *104*, 072106.

(26.) Park, H. H.; Heasley, R.; Sun, L.; Steinmann, V.; Jaramillo, R.; Hartman, K.; Chakraborty, R.; Sinsermsuksakul, P.; Chua, D.; Buonassisi, T.; Gordon, R. G. Co-Optimization of SnS Absorber and Zn(O,S) Buffer Materials for Improved Solar Cells. *Prog. Photovoltaics* **2015,** *23,* 901-908.

(27.) Chakraborty, R.; Steinmann, V.; Mangan, N. M.; Brandt, R. E.; Poindexter, J. R.; Jaramillo, R.; Mailoa, J. P.; Hartman, K.; Polizzotti, A.; Yang, C.; Gordon, R. G.; Buonassisi, T. Non-Monotonic Effect of Growth Temperature on Carrier Collection in SnS Solar Cells. *Appl. Phys. Lett.* **2015**, *106*, 203901.

(28.) Hamzah, Y.; Guastavino, F.; Llinares, C.; Djessas, K.; Masse, G. SnS Thin Films Grown by Close-Spaced Vapor Transport. *J. Mater. Sci. Lett.* **2000**, *19*, 2135-2137.

(29.) Ghosh, B.; Bhattacharjee, R.; Banerjee, P.; Das, S. Structural and Optoelectronic Properties of Vacuum Evaporated SnS Thin Films Annealed in Argon Ambient. *Appl. Surf. Sci*. **2011**, *257*, 3670-3676.